Title

Multiscale Magneto-mechanical Coupling Framework of Magnetorheological Elastomer Composites

Permalink

https://escholarship.org/uc/item/4f50r778

Author

FENG, SHENGWEI

Publication Date

2024

Peer reviewed|Thesis/dissertation

UNIVERSITY OF CALIFORNIA,
IRVINE

Multiscale Magneto-mechanical Coupling Framework of Magnetorheological Elastomer Composites

DISSERTATION

submitted in partial satisfaction of the requirements
for the degree of

DOCTOR OF PHILOSOPHY

in Civil Engineering

by

Shengwei Feng

Dissertation Committee
Professor Lizhi Sun, Chair
Professor Anne Lemnitzer
Professor Mohammad Javad Abdolhosseini Qomi

2024

Table of Contents

Page

List of Figures v

List of Tables x

Acknowledgments xi

Vita xii

Abstract of the Dissertation xiii

Chapter 1 Scope of Thesis 1

Chapter 2 Literature Review 4
  2.2 Fabrication and Experimental Studies of MREs 5
  2.3 Modeling of MREs 10
  2.4 Motivation and Objectives 19

Chapter 3 Modeling and Simulation Methodologies for Magnetorheological Elastomers (MREs) 22
  3.1 Introduction 22
  3.2 Modeling of Particle Distribution 22
    3.2.1 Random Distribution 23
    3.2.2 Periodic Distribution 28
    3.2.3 Chain Distribution 29
  3.3 Magnetic Interaction of Particles 30
    3.3.1 Dipole Method 31
    3.3.2 Maxwell Method 32
    3.3.3 Comparison of the Dipole and Maxwell Methods for Magnetic Interactions 33
  3.4 Mechanical and Magnetic Coupling Methods 39
    3.4.1 Partial Coupling Method 40
    3.4.2 Full Coupling Method 41
  3.5 Boundary Conditions and RVE Selection 43
  3.6 Homogenization Methods 48
  3.7 Conclusions 51

Chapter 4: Quasi-static Analysis of Magnetorheological Elastomers (MREs) 53
  4.1 Introduction 53
  4.2 Sanity Check 53
  4.3 Comparative Analysis of Various Modeling Techniques 55
    4.3.1 Comparison of Force and Energy Methods 56
    4.3.2 Comparison of 2D and 3D Models 58
    4.3.3 Comparison of Random and Periodic Distribution 60
  4.4 Analysis of MREs with Chain Structures 64

Chapter 5 Viscoelasticity Analysis of Magnetorheological Elastomers (MREs) 70
  5.1 Introduction 70
  5.2 Linear Viscoelastic Model 70
  5.3 Comparison of 2D and 3D Models Under Sinusoidal Loading 72
  5.4 Dynamic Modulus 74
  5.5 Analysis of Factors Influencing the Viscoelastic Behavior of MREs 76
    5.5.1 Magnetic Field Dependent Behavior 76
    5.5.2 Strain Dependent Behavior 84
    5.5.3 Frequency Dependent Behavior 87
  5.6 Conclusions 88

Chapter 6 Modeling of Visco-hyperelastic Behavior of Magnetorheological Elastomers (MREs) 89
  6.1 Introduction 89
  6.2 Hyperelastic Model 89
  6.3 Strain Amplitude Dependent Behavior 91
  6.4 Modeling the Payne Effect 94
  6.5: Strain-Dependent Behavior of the Model with Magnetic Field 96
  6.6 Comparative Analysis of Full Coupling and Partial Coupling Models 98
  6.7 Conclusions 101

Chapter 7 Modeling of Interface Behaviors of Magnetorheological Elastomers (MREs) 103
  7.1 Introduction 103
  7.2 Debonding Analysis with Cohesive Zone Model (CZM) 103
  7.3 Modeling of MREs with Various Initial Debonding States 109
  7.4 Interface Analysis 113
    7.4.1 Modeling of Interface Condition Under Magnetic Field 114
    7.4.2 Modeling of Particle Rotation 122
  7.5 Impact of Interface-Related Parameters on the Dynamic Behavior of MREs 125
  7.6 Comparison of Model Predictions with Experimental Data 130
  7.7 Conclusions 135

Chapter 8 Instability Analysis of Magnetorheological Elastomers (MREs) 136
  8.1 Introduction 136

8.2 Modeling of Macroscopic Instability 136
8.3 Modeling of Microscopic Instability 140
8.4 Modeling of Interface Stability 154
8.5 Conclusions 158

Chapter 9 Conclusions and Future Works 159
9.1 Conclusions 159
9.2 Future Works 160

References 163

List of Figures

Page

Figure 3.1 Flow chart of the random placement method for particle distribution in MRE simulations. 24

Figure 3.2 A sketch of microstructure variations at different volume fractions using the random placement method. (a) 10% volume fraction, (b) 20% volume fraction, (c) 30% volume fraction, (d) 40% volume fraction. 25

Figure 3.3 Flow chart of the shaking method for particle distribution in MRE simulations. 26

Figure 3.4 Microstructures of MREs generated by the shaking method at 50% volume fraction (a) initial square periodic distribution, (b) microstructure after 50 shakes, (c) microstructure after 500 shakes. 27

Figure 3.5 MREs featuring randomly distributed particles that intersect the matrix edges with a volume fraction of 30%. 28

Figure 3.6 Schematic representation of MRE composites with (a) a square and (b) a hexagonal distribution of particles. 29

Figure 3.7 Schematic representation of MAE composites with (a) a wavy and (b) a straight chain distribution of magnetoactive particles in the matrix. 30

Figure 3.8 A schematic of the dipole interaction model. 31

Figure 3.9 A schematic of the vertical interaction force model. 34

Figure 3.10 Normalized magnetic forces in the y direction as a function of l, with all forces normalized by dividing them by the magnetic force from the dipole model at l=2. 35

Figure 3.11 A schematic of the rotational interaction force model. 36

Figure 3.12 Normalized magnetic forces as a function of l (a) x component of the magnetic force, (b) y component of 38 the magnetic force. All magnetic forces have been normalized by dividing them by the magnitude of magnetic force Fx calculated using the dipole model. The positive value indicates attraction, while the negative value indicates repulsion.

Figure 3.13 Periodic boundary condition of a single-particle RVE 44

Figure 3.14 RVE with 1% shear strain (a) RVE with quarter particles, (b) RVE with full particles. 46

Figure 3.15 Adjustments to RVE using periodic boundary conditions with boundary-intersecting particles: (a) initial random distribution, (b) distribution after spatial correction. 47

Figure 4.1 The effect of shear strain amplitude on relative MR effect for body force method and energy method. 57

Figure 4.2 3D RVE showcasing a square periodic distribution generated using ANSYS. 59

Figure 4.3 Effective shear modulus comparison for RVEs with random and periodic distribution. 62

Figure 4.4 Relative MR effect for straight chain RVEs with varying particle numbers. 65

Figure 4.5 A sketch of the 2 particle interaction model under shear deformation. 66

Figure 4.6 Normalized magnetic force Fmx vs. distance ratio q. 67

Figure 4.7 Normalized MR effect vs. distance ratio q. 67

Figure 5.1 Sketch of the generalized Maxwell viscoelastic model. 71

Figure 5.2 The comparison of 2D and 3D models. 72

Figure 5.3 Hysteresis loop with magnetic flux densities B = 0 mT, 50 mT, 100 mT, 150 mT, and 200 mT. 77

Figure 5.4 Dynamic modulus for different magnetic flux densities: (a) storage modulus, (b) loss modulus, (c) loss factor. 78

Figure 5.5 Comparison of the hysteresis loop in Norouzi’s experiment with simulation results: (a) B = 0 mT, (b) B = 272mT. 81

Figure 5.6 Comparison of the hysteresis loop in Dargahi's experiment with simulation results: (a) B = 0 mT, (b) B = 150 mT. 82

Figure 5.7 Hysteresis loop subjected to different strain amplitudes at B = 0 mT: (a) model prediction, (b) Dargahi's experiment. 86

Figure 6.1 Comparison of hysteresis loops from Norouzi's experiment with model prediction at different strain amplitudes, B = 0 mT: (a) 2.5% strain, (b) 5% strain, (c) 10% strain, (d) 20% strain. 92

Figure 6.2 Comparison of the hysteresis loop from Norouzi's experiment with model prediction at 20% strain amplitude considering the Payne effect. 95

Figure 6.3 Model prediction of hysteresis loop at different strain amplitudes with B = 75 mT. 97

Figure 6.4 Comparison of hysteresis loops simulated using full coupling and partial coupling methods at different strain amplitudes, B = 75 mT: (a) 2.5%, (b) 5%, (c) 10%, (d) 20%. 100

Figure 7.1 Analysis of Dominant CZM Modes in Debonding Behavior of MREs through Effective Shear Modulus Curves under Increasing Compressive Strain. 105

Figure 7.2 Debonding behavior with CZMs of different stiffness under compression. 106

Figure 7.3 Illustration of interface debonding process using FEM model. 108

Figure 7.4 A sketch of the interface debonding status model with four regions. 110

Figure 7.5 The influence of magnetic field on the hysteresis behavior of models with different debonding conditions. 113

Figure 7.6 FE model illustration of different interface conditions within a chain under the magnetic field. 115

Figure 7.7 Friction energy of different interface conditions: (a) interface 1, (b) interface 2, (c) interface 3. 118

Figure 7.8 Friction energy per cycle of different interface conditions: (a) interface 1, (b) interface 2, (c) interface 3. 121

Figure 7.9 Rotation angle of particle 2 with different interface friction coefficients under cyclic loading. 124

Figure 7.10 Rotation angle of particle 2 (f = 0.4) with and without magnetic field under cyclic loading. 124

Figure 7.11 The influence of interface friction coefficient t and magnetic flux density on (a) storage modulus, (b) loss modulus, (c) loss factor. 128

Figure 7.12 Impact of microstructure on the loss factor in MREs. 130

Figure 7.13 Variation of dynamic damping in MREs with applied magnetic field: Data from Li's experiment. 131

Figure 7.14 Dependence of the shear storage modulus (a) and loss factor (b) on the applied magnetic flux density: Data from Yu's experiment. 132

Figure 7.15 Comparison of model predictions with experimental results on loss factor: (a) Li's experiment, (b) Yu's experiment. 134

Figure 8.1 Sketch of a unit cell. 138

Figure 8.2 Critical compressive strain vs. applied magnetic field strength. 139

Figure 8.3 Critical strain detection using the first three particles of a six-particle chain model: (a) particle 1, (b) particle 2, (c) particle 3. 142

Figure 8.4 Strain distribution (ε_{yy}) in the MRE model, with compressive strain at (a) 0.32, (b) 0.33, (c) 0.34. 143

Figure 8.5 Dependence of critical strain on particle radius. 144

Figure 8.6 Effective shear modulus vs. compressive strain of MRE with a straight chain. 145

Figure 8.7 Geometry of the particle wavy chain. 147

Figure 8.8 Effective shear modulus vs. compressive strain of MRE with wavy chains. 148

Figure 8.9 Influence of magnetic flux density on critical strain. 150

Figure 8.10 Effective shear modulus vs. compressive strain with and without the magnetic field. 151

Figure 8.11 Effective shear modulus vs. compressive strain with and without the magnetic field for MRE with wavy chains. 152

Figure 8.12 FEM model illustration of interface conditions at strain: (a) 0.25, (b) 0.3, (c) 0.35. 154

Figure 8.13 Critical strain detection with the weakly bonded model of straight chain. 155

Figure 8.14 FEM model illustration of interface conditions of wavy chains at strain: (a) 0.15, (b) 0.2, (c) 0.25, (d) 0.3. 156

Figure 8.15 Critical strain detection with the weakly bonded model of wavy chain. 157

List of Tables

Page

Table 5.1 Parameters for the Prony series model. 72

Table 5.2 Material properties of the FEM model for comparison with experimental data. 80

Acknowledgments

I would like to express my deepest gratitude to my advisor, Lizhi Sun, whose guidance, patience, and support from the initial to the final level enabled me to develop an understanding of the subject. His/her/their insights and expertise have been invaluable throughout this process.

I am also grateful to my colleagues and mentors in the Department of Civil and Environmental Engineering (CEE). Their broad knowledge and responsive assistance have played a crucial role in the completion of this project.

I must also extend my heartfelt thanks to my friends, who provided me with motivation and a sense of community throughout my studies. Their constant encouragement and good-natured support have been a pillar of strength.

Lastly, but most importantly, I wish to thank my family for their unwavering support and endless love. Their belief in my abilities and their reassurance through challenging times were essential to my success. This achievement is as much theirs as it is mine.

Vita

Shengwei Feng

2013-2017	Bachelor of Engineering in Civil Engineering Xi'an University of Architecture and Technology
2017-2019	Master of Science in Civil Engineering University of California, Irvine
2019-2024	Doctor of Philosophy in Civil Engineering University of California, Irvine

Abstract of the Dissertation

Multiscale Magneto-mechanical Coupling Framework of Magnetorheological Elastomer Composites

By

Shengwei Feng

Doctor of Philosophy in Civil Engineering

University of California, Irvine, 2024

Professor Lizhi Sun, Chair

This dissertation introduces a multiscale modeling and simulation framework for studying magnetorheological elastomer (MRE) composites, effectively bridging the gap between detailed microscopic modeling and experimental findings. Preliminary investigations focus on understanding the baseline magneto-mechanical properties of MREs, setting the stage for deeper inquiries into specific behaviors. Subsequent simulations integrate viscoelastic and hyperelastic properties to examine how the models respond under cyclic loading, with a particular focus on behavior that depends on magnetic field strength and strain variations. By scrutinizing microstructural influences such as particle distribution and interface conditions, the research elucidates how these factors affect MRE responses to magnetic fields and mechanical stresses. Modeling and simulations reveal that interface friction and particle dynamics are crucial in determining MREs' damping characteristics and overall stability. Notably, the study identifies how variations in interfacial interactions under different magneto-mechanical conditions significantly impact the performance and reliability of MRE composites. This comprehensive analysis deepens our understanding of MRE behavior and paves the way for optimizing the

design and application of these smart materials in adaptive systems, potentially transforming their use in various industrial and technological sectors.

Chapter 1 Scope of Thesis

This dissertation establishes a comprehensive multiscale framework for analyzing magnetorheological elastomer (MRE) composites, aimed at bridging the gap between microscopic-based modeling and experimental observations. The research begins by validating and comparing existing modeling methodologies, focusing on aspects critical to understanding MREs, such as magneto-mechanical coupling methods, boundary conditions, particle distribution, and homogenization techniques. The thesis progressively develops models that encompass increasingly complex particle distributions, integrating viscoelastic and hyperelastic properties, and considering non-affine large deformation effects. A particular emphasis is placed on detailed interfacial behavior and instability analyses. The models aim to replicate experimental results, highlighting the significant role of interface friction in the increase of dynamic damping properties under magnetic fields.

The research reveals that differences in interface properties and friction behavior between particles and the matrix substantially affect the dynamic responses of MREs, especially damping. Moreover, the instability modeling shows that MREs subjected to combined compressive and shear forces may exhibit premature buckling. By integrating instability simulations with interface models, it is discovered that instabilities develop earlier and are accompanied by distinctive friction behaviors under compression, potentially explaining the notable increase in damping observed in MREs during such conditions.

This dissertation is organized as follows:

Chapter 2 reviews the existing literature on magnetorheological elastomers (MREs), focusing on the evolution of experimental validations, modeling methodologies and discusses the motivation and objectives of this study.

Chapter 3 delves into the modeling and simulation methodologies applied to MREs, emphasizing particle creation algorithms for varying distributions within the elastomer matrix. This chapter evaluates different mechanical and magnetic coupling methods, discusses the implementation of appropriate boundary conditions, and explores homogenization techniques critical for accurate microstructural modeling and simulations. Objectives include demonstrating the effectiveness of various modeling and simulation methods and providing guidelines on their appropriate application.

Chapter 4 investigates the influence of chain structures and particle distributions on the magnetorheological effect under quasi-static conditions. It employs detailed simulations to provide a thorough understanding of these phenomena, forming a stable foundation for the dynamic analyses in later chapters.

Chapter 5 examines the dynamic responses of MREs, particularly how their properties vary with changes in magnetic field strength, strain amplitude, and frequency. The chapter uses finite element models incorporating a linear viscoelastic matrix under small deformations to simulate these dynamics. Comparisons with experimental results are made to discuss the model's strengths and limitations in replicating observed behaviors.

Chapter 6 introduces a visco-hyperelastic model designed to capture the complex non-linear behaviors of MREs under significant strain amplitudes. It considers large strain effects such as magneto-mechanical coupling and Payne’s effect. Model predictions are validated against experimental results to evaluate accuracy and applicability in real-world scenarios.

Chapter 7 focuses on the interface behavior within MREs, especially examining debonding events and interactions between particles and the matrix under dynamic conditions. It includes an in-depth analysis of how interface parameters influence the damping and stiffness properties of MREs. A model incorporating adjustable microstructural and interface parameters is presented to elucidate these interactions, supported by experimental comparisons.

Chapter 8 explores various instabilities in MREs under different loading conditions, including macroscopic, microscopic, and interface instabilities. It assesses how factors like particle distribution, material properties, magnetic fields, and interface conditions contribute to these instabilities, providing a comprehensive analysis of their implications on the performance and reliability of MREs.

Chapter 9 concludes the findings of the thesis, discussing their implications and proposing future research directions.

Chapter 2 Literature Review

2.1 Introduction

Magnetorheological (MR) materials are a distinctive category of smart materials that dynamically adapt their mechanical properties—such as stiffness, damping, and hysteresis—in response to external magnetic fields. These composites, comprising magnetically polarizable particles embedded within carriers like fluids, elastomers, gels, or foams, showcase transformative potential across a range of applications due to their reversible and rapid property changes [1]. The inception of MR technology traces back to the pioneering work of Thomas Rabinow in 1948, who introduced the concept of magnetic fluids [2]. Rabinow's subsequent discovery of the magnetorheological effect in 1951 laid the foundational principles that catalyzed further research in this field, highlighting the transformative potential of MR materials in various applications, from automotive systems to medical devices.

In their default state, MR fluids consist of randomly distributed magnetic particles suspended in a carrier fluid. Upon application of a magnetic field, these particles align into chain-like structures, markedly altering the fluid's viscosity and forming a semi-solid that responds in milliseconds. While MR fluids offer distinct advantages such as low power requirements and significant changes in their mechanical moduli, they encounter challenges like particle sedimentation and fluid leakage, which can compromise performance and durability [3]. These limitations have spurred developments to refine MR fluid formulations and deployment methods, enhancing their application scope and effectiveness.

To address the inherent limitations associated with fluid-based magnetorheological systems, Magnetorheological Elastomers (MREs) have been developed as a solid counterpart to MR fluids. The concept of MREs was first introduced by Rigbi and Jilken in 1983[4], who embedded ferrite particles within an elastomer matrix. This pioneering work laid the groundwork for further exploration into the properties of MREs. Subsequent significant advancements were made in 1996 when Jolly et al. [5] began comprehensive studies on MRE behavior. Since then, the various properties of MREs have been extensively investigated, contributing greatly to the understanding and application of these materials. This configuration prevents issues prevalent in MR fluids, such as particle sedimentation and fluid leakage, thereby extending the material's functional lifespan and reliability.

MREs are particularly noted for their field-dependent mechanical properties, which can be finely tuned by adjusting factors such as the elastomer matrix composition, particle size and distribution, and magnetic field strength. The ability to control these parameters allows for the customization of MREs' viscoelastic properties to meet specific application requirements, ranging from vibration damping systems to adaptive robotics [6]-[8].

2.2 Fabrication and Experimental Studies of MREs

MREs are engineered composites composed of three fundamental elements: ferromagnetic particles, an elastomeric matrix, and various additives that enhance the composite's performance. Often, researchers opt for iron particles [9,10]. Particularly favored are Carbonyl Iron Particles (CIPs) for their high saturation magnetization, which enables a robust MR effect over a broader range of magnetic fields, making them ideal for diverse MR applications [11,12]. The size of these particles is crucial; while many studies utilize particles ranging from 3um to 9um to optimize the MR effect, there are variations where sizes as small as 0.5um and as large as 100um are employed to meet specific performance criteria [13,14].

Various types of elastomeric matrices, such as silicone rubber, natural rubber, thermoplastic elastomers, and polyurethane, are selected based on the desired properties of the final MRE product. These matrices determine the flexibility, durability, and response rate of the MRE under magnetic influence [15]. Additives play a significant role in improving the processability and stability of the composite. For instance, silicone oil is commonly added as a softening agent, which not only decreases the storage modulus of the elastomer but also helps prevent the agglomeration of ferromagnetic particles, thereby enhancing the overall uniformity and compatibility of the MRE [16,17].

The manufacturing process of MREs involves a meticulous mixing of these primary components, followed by the extraction of air bubbles under vacuum in a controlled environment to ensure a flawless matrix. Depending on the desired characteristics of the MRE, the mixture can either cure in the absence of a magnetic field to form isotropic MREs where particles are uniformly distributed [18] or in the presence of a magnetic field to create anisotropic MREs characterized by chain-like structures of particles aligned along the field lines [19]. While some silicone rubbers used in MREs cure at room temperature, curing temperatures above 100°C are generally recommended to expedite the process and enhance the material's mechanical properties.

The MR effect in MREs is intricately linked to the orientation of magnetic particles within the matrix. Traditionally, controlling this orientation during the curing process has proven challenging due to the difficulty in precisely manipulating the microstructural arrangement. This lack of control often leads to variability in the properties of the finished products. Recently, however, the advent of 3D printing technology has revolutionized the fabrication of MREs. Advanced 3D printing techniques allow for the precise and accurate placement of magnetic particles within the matrix materials, ensuring consistent orientation without the necessity of an external magnetic field [24-25].

The mechanical properties of Magnetorheological Elastomers (MREs) are known to undergo significant changes under the influence of magnetic fields. These changes are typically assessed using various testing equipment such as servo-hydraulic material testing machines, dynamic mechanical analyzers, and rheometers [26-28]. A breadth of research has been dedicated to the experimental characterization of MREs across various excitation modes. Studies have documented the response of MREs under conditions of compression [29,30], shear [31,32], tensile [33,34], and mixed-mode [35,36] testing. Research highlights the ability of MREs to adjust their stiffness and damping properties through the application of magnetic fields. This phenomenon, central to the functionality of MREs, has been extensively studied to understand the factors that influence the MR effect and the materials' damping capabilities.

Volume fraction and particle size are considered one of the crucial factors influencing the properties of MREs. Guan et al. [23] investigated the magnetostrictive properties of MREs consisting of carbonyl iron particles embedded within a silicone rubber matrix. Their findings revealed that magnetostriction in MREs increases with the volume fraction of iron particles. However, this effect reaches a saturation point at higher magnetic fields, underscoring that the interaction between the particles and the silicone matrix is the primary driver of magnetostriction. Lu et al. [20] conducted a study on the effects of large particle size carbon black (CB) on MREs. They discovered that CB type N990, which has the largest particle size, significantly enhances the magnetorheological effects and damping performance, thereby improving the viscoelastic properties and structural integrity of MREs. Conversely, Hegde et al. [21] indicate that larger particles can decrease the initial shear modulus while increasing the saturated magnetic-induced shear modulus to a certain extent, beyond which it begins to decline. This research identifies an optimal particle size that maximizes the MR effect. Similarly, an ideal particle size for dynamic damping has been identified, as highlighted in another piece of research [22]. Furthermore, research conducted by Stepanov et al. [37] has demonstrated that mixing iron particles of varying sizes within MRE formulations can enhance the material's properties. Specifically, they observed that a blend of smaller and larger iron particles resulted in a higher storage modulus and a higher loss modulus compared to formulations with monodisperse iron particles. This observation is corroborated by Li and Zhang [38], who also noted improved performance in polydisperse samples. The enhancement is possibly attributed to a higher degree of iron particle packing within the chain-like aggregates in polydisperse samples compared to those in monodisperse samples.

Particle distribution significantly influences the MR behavior of Magnetorheological Elastomers (MREs). Varga et al. [39] explored the impact of particle distribution under magnetic fields. Their study revealed that isotropic MREs with randomly distributed particles exhibit a moderate increase in elastic modulus when exposed to external magnetic fields. The enhancement is uniform across the material without any directional dependency. In contrast, anisotropic MREs, which feature aligned particles, demonstrate a notably larger increase in elastic modulus under magnetic influence. This increase is particularly marked when the magnetic field aligns parallel to the particle chains. The degree of modulus enhancement in anisotropic MREs is strongly contingent upon the alignment of the magnetic field relative to the chain-like structures of the particles, with the maximum increase observed when the magnetic field direction and the direction of particle chains coincide with the applied stress. This phenomenon is further corroborated by Khanouki et al. [40], who reported that anisotropic MREs not only exhibit a greater increase in stiffness and damping upon exposure to magnetic fields but also achieve higher levels of mechanical performance enhancement at lower field strengths. Their findings highlight the efficiency of anisotropic MREs in utilizing magnetic fields to optimize their mechanical properties, reinforcing the impact of particle orientation on the effectiveness of the MR effect.

A multitude of other factors can also significantly influence the mechanical and rheological properties of MREs. The shape of the filler is one such factor, with distinct impacts observed depending on the particle geometry. For instance, Tong et al. [41] explored the effects of irregular flower-like Cobalt particles, while Hapipi et al. [42] investigated the properties of MREs incorporating plate-like Carbonyl Iron Particles (CIP). Beyond particle shape, the type of particle [43], the matrix material [44], and the type of additives used [45,46] also play critical roles in defining the overall behavior of MREs. Additionally, experimental conditions contribute substantially to the variability in results. Factors such as temperature [50], strain amplitude [47], frequency [48], and magnetic field strength [49] are crucial in shaping the experimental outcomes, leading to diverse findings. While many studies published in refereed journals converge on certain aspects, illustrating consistent trends or effects, others present contradictory results, underscoring the complexity of accurately predicting MRE behavior.

2.3 Modeling of MREs

Alongside experimental characterization, developing models that can accurately predict the response of MREs under varying conditions—such as applied magnetic field, driving frequency, strain amplitude, and other operational and environmental factors—is crucial for their effective use in adaptive devices. There are three general modeling approaches employed to simulate the behavior of MREs.

The first approach is the phenomenological method, which utilizes configurations of spring and damper elements to simulate the dynamic stiffness and damping properties of MRE materials. This technique is particularly effective in capturing the viscoelastic behavior of MREs under different loading conditions, making it a valuable tool for applications requiring dynamic response modulation.

Another approach is the magnetoelastic or continuum mechanics method, where the MRE is considered a continuous medium. The effects of iron particles are seamlessly integrated into the elastomeric matrix. This method enables researchers to examine the macroscopic behavior of the material through coupled equations of elasticity and magnetism, providing deep insights into how MREs respond to magnetic influences.

Additionally, microscale predictive models based on micromechanics offer a granular perspective by focusing on the microstructure of MREs. These models account for the isotropic or anisotropic distribution of magnetic particles within the matrix and assess the magnetic interactions between the particles and their influence on the overall mechanical properties of the elastomer. This detailed approach is invaluable for understanding and predicting material behavior at the microscopic level, where particle interactions play a crucial role in determining the performance of MREs.

The phenomenological model is extensively employed to predict the viscoelastic properties of MREs, addressing behaviors such as creep, stress relaxation under constant stress, stress-strain hysteresis loops under oscillatory loading, and the frequency dependence of the stress-strain curve. Li et al. [51] utilized a four-parameter spring-dashpot viscoelastic model to effectively simulate the stress-strain hysteresis curve of MREs, as illustrated in Figure 2.1. This model adequately captures the linear viscoelastic behavior of MREs under specific loading conditions. However, the assumption of linear viscoelasticity becomes insufficient when the loading conditions change, a limitation noted by Agirre-Olabide et al. [52].

To address this nonlinearity, Chen and Jerrams [53] modified the existing model by incorporating a variable stiffness spring and a spring-Coulomb friction slider. This enhancement aims to better represent the interfacial slippage between the matrix and the particles, further details of which are depicted in Figure 2.2. This model can be divided into three parts to depict linear viscoelastic behavior, field-dependent mechanical properties, and interface slip between the particles and matrix. Such refinements have been instrumental in simulating more complex behaviors, allowing for a nuanced analysis of the interaction dynamics within the composite under varied environmental and operational conditions.

Despite these advancements, numerous nonlinear behaviors persist in MREs, especially when they are integrated into devices with other materials. In response to these complexities, some researchers have turned to the Bouc-Wen model, initially introduced by Bouc [54] and later expanded by Wen [55]. Renowned for its capability to emulate a variety of hysteretic cycle shapes, this model is well-suited for a broad range of hysteretic systems. It has been adapted to analyze the behavior of MREs, with Yang et al. [56] proposing a Bouc-Wen-based phenomenological model to characterize phenomena such as strain stiffening and the nonlinear force-velocity relationship in MRE devices. In their approach, the original Bouc-Wen model is integrated in parallel with a Voigt element to more accurately depict both mechanical behavior and hysteresis, as shown in Figure 2.3.

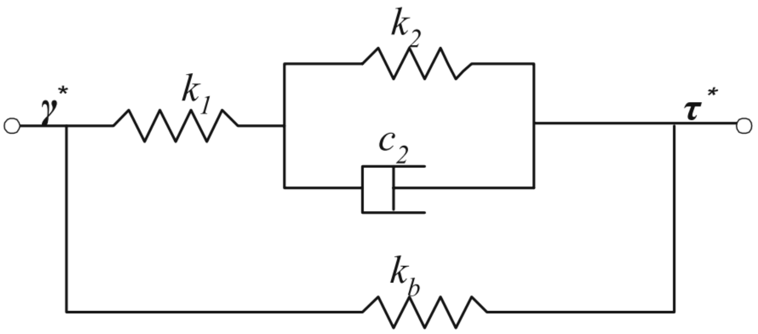

Figure 2.1 Four-parameter viscoelastic model for MREs [51].

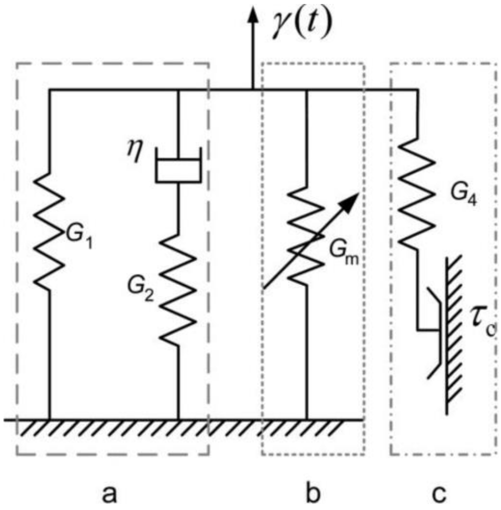

Figure 2.2 Modified rheological model for MREs [53].

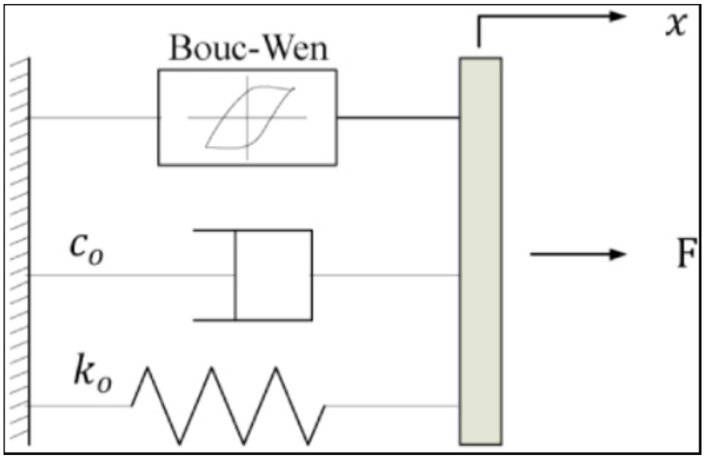

Figure 2.3 MRE isolator model with Bouc-Wen element [56].

The theoretical foundations for the magnetoelastic response of solids, established in the 1960s, began with the pioneering work of Truesdell and Toupin [57], who utilized direct methods from the conservation laws of continuum mechanics. Their initial theories were further developed by Tiersten [58], who formulated comprehensive field equations specifically for magnetically saturated media. Concurrently, Maugin and Eringen [59] delved into the complex interactions between magnetic and mechanical domains, highlighting the coupling between electronic spin and lattice continua.

Building on these foundational studies, Kankanala and Triantafyllidis [60] explored the efficacy of traditional direct methods alongside energy methods based on the principle of energy minimization. Their comparisons revealed that for isotropic distributions of particles, both approaches produce equivalent governing equations and boundary conditions. However, they noted that the energy minimization method is particularly advantageous for addressing complex, nonlinear problems or situations that involve multiple physical effects, offering improved flexibility, accuracy, and analytical depth.

Further expanding the theoretical landscape, Dorfmann and Ogden [61] provided a comprehensive framework for analyzing boundary-value problems in electro-sensitive elastomers capable of undergoing large electroelastic deformations. Their work meticulously outlined the governing equations for electroelastic conditions, primarily focusing on static scenarios. They clarified the constitutive laws for the Cauchy stress tensor and electric field vectors, streamlining the formulation into compact expressions that simplify the resolution of complex boundary-value problems. Their analysis included practical examples such as the influence of a radial electric field on the azimuthal shear response of a circular cylindrical tube and the deformation characteristics of an internally pressurized spherical shell. A 'total' free energy function was also defined, integrating mechanical and electrical energy densities to better facilitate the understanding of electro-mechanical interactions within these materials.

Since these seminal contributions, the framework of magneto-elasticity has become well-established. However, the mathematical modeling of Magnetorheological Elastomers (MREs) continues to present significant challenges, primarily due to the strong nonlinear coupling between mechanical and electromagnetic responses. Some researchers in this field are enhancing theoretical models, for example, developing implicit constitutive relations and striving towards the linearization of existing models [62]. Meanwhile, others are leveraging numerical solutions and Finite Element Method (FEM) models [63-65] to circumvent some of the inherent complexities of traditional modeling approaches.

While previous models primarily focus on the macroscopic properties of MREs, microscale models, which consider the material's microstructure, are pivotal in addressing the distribution of particles within the matrix. Pioneering work by Jolly et al. [4] and Davis [66] introduced a two-particle model that utilizes the interaction between magnetic dipoles to predict the mechanical behavior of MREs both with and without the influence of a magnetic field. By calculating the magnetic energy between adjacent dipoles, they successfully derived the field-induced shear modulus as a function of applied magnetic field density and particle volume fraction.

While the magnetic point dipole approach may provide essential guidance for the magnetic microstructure behavior of MREs, it cannot accurately describe the overall magneto-mechanical behavior of MREs. Experimental studies by Danas et al. [67] have highlighted the significant impact of microstructural properties on the magneto-mechanical behavior of Magnetorheological Elastomers (MREs). Building upon this foundation, subsequent research expanded the basic two-particle model to more intricate straight-chain models. These models assume that particles, small enough to be considered magnetic dipoles, are aligned with the external magnetic field, an arrangement known as the dipole model. Coquelle et al. [68] noted that the relative positioning of these particles within the chain critically influences the increase in shear modulus of MREs under a magnetic field.

However, while these models effectively predict the MR effect under shear, they fall short in explaining the MR effect under tension/compression scenarios, where the MR effect is typically negative. Further investigations using Scanning Electron Microscopy (SEM) by researchers such as Bobarth et al. [69], Chen et al. [70], and Coquelle and Bossis [71] have provided micrographs showing that particle chains in MREs are often wavy rather than strictly straight. This waviness is explained by variations in magnetic flux density during the preparation of MREs, which is not uniformly distributed across the cross-sectional area of the magnetic conductor, leading to irregularly shaped chains.

In response to these findings, Ivaneyko et al. [72] proposed a model where iron particles form a rectangular-lattice microstructure, suggesting that wavy chains could account for the observed increase in tensile modulus. Building on this idea, Han et al. [73] developed a model to examine the MR effect on particle alignment. This model differentiates between three types of chain formations: straight, wavy, and finite-length chains, as depicted in Figure 2.4.

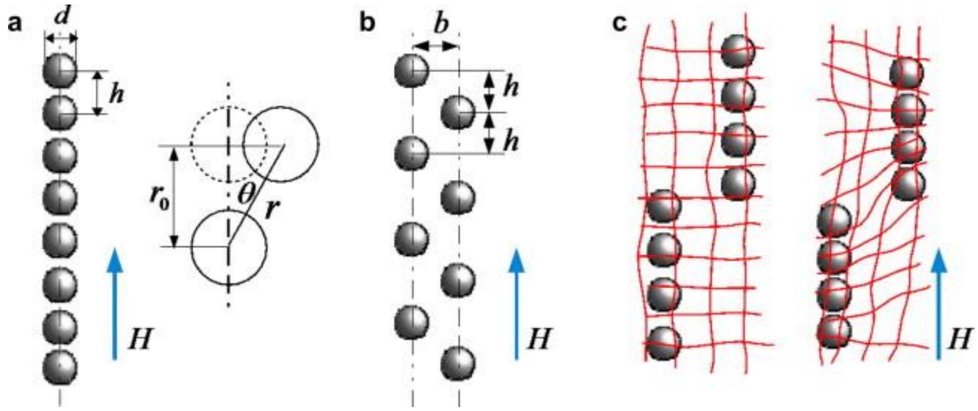

Fig 2.4 Schematics of three possible mechanisms of the field-stiffening effect in an MRE: (a) dipolar interaction between particles in a straight chain, (b) dipolar interaction in a wavy particle chain, and (c) particle chains of finite lengths [73].

Their findings indicate that the magnetic interaction energy In MREs depends on the ratio b/h, where h is the vertical center-to-center particle spacing and b is the horizontal center-to-center particle spacing. Smaller b/h ratios are typically associated with straight particle chains, while intermediate b/h values indicate wavy chains. When MREs are subjected to tension or compression that aligns with the direction of particle chains, the b/h ratio changes, leading to additional stress and a change in tensile modulus.

In addition to chain models, the study of particle arrangement within MREs has also utilized regular or periodic structures as idealized spatial dispersions of particles. Various lattice structures have been explored to investigate their impact on the field-induced properties of MREs[80-82]. Ivaneyko et al. [74,75] analyzed three specific lattice models: simple-cubic (SC), body-centered-cubic (BCC), and hexagonal-close-packed (HCP). These models were instrumental in studying the behavior of both isotropic and anisotropic MREs under homogeneous magnetic fields. Expanding on this approach, Khanouki et al. [76,77] considered a broader range of lattices, including edge-centered-cubic (ECC), body-&-edge-centered cubic (BECC), face-&-edge-centered cubic (FECC), and body-&-face-&-edge-centered cubic (BFECC). Their research aimed to delve deeper into the magneto-mechanical behavior of MREs by examining how these complex lattice structures influence material properties. The magnetic energy within these structures was defined as a function dependent on the lattice type and particle arrangement, with the total energy computed as the sum of the matrix's elastic energy and the particles' magnetic energy. The stress and modulus of the MREs were then derived from this energy function. Despite most lattice structures contracting in the direction of the applied homogeneous magnetic field due to magnetic particle interactions, it was observed that structures with a random isotropic particle distribution tended to extend in the direction of the magnetic field. Moreover, increases in the magnetic field generally led to an increase in shear modulus for most particle distributions. However, it was noted that the BCC and FCC lattices exhibited a decrease in shear modulus under magnetic field application, a finding that contradicts experimental observations.

Research into the microstructure of MREs has been extensively pursued by various other studies. For instance, Galipeau, Evan, et al. [78] applied magnetoelastic theory to develop models that include both periodic microstructures, such as rectangular and quasi-hexagonal unit cells, and random microstructures. Their research underscores that although magnetic susceptibility might be similar across composites, magnetoelastic effects can vary significantly due to differences in microstructure, influencing the local fields and effective properties of the materials. In another study, Coquelle et al. [79] introduced an analytical model that simulates the progressive breaking of polymer-to-particle bonds during mechanical stretching. This model, which focuses on the stress-strain behavior of a two-sphere system, generally aligns with experimental observations but tends to overestimate the size of the debonding cavity. This discrepancy indicates that while the model effectively captures the initial stages of debonding, it may not fully account for the complexities of real material behavior under diverse strain conditions. Further expanding on the theme of microstructural influence, Khanuki et al. [83] developed a coarse-grained network model using Lagrange's equations to calculate relaxation times. This study emphasizes the critical role of microstructure, particularly the arrangement of magnetic particles, in determining the material's viscoelastic properties under magnetic fields. Utilizing a cubic network with particles connected by elastic springs, the model predicts changes in storage and loss moduli, which have been corroborated by experimental data. Theoretical insights from this model suggest that debonding or structural failures within MREs could be indirectly inferred from analyzing relaxation times and moduli changes under various loading conditions.

2.4 Motivation and Objectives

While considerable research has focused on the phenomenological modeling and magnetoelastic properties of MREs, the exploration of their magneto-mechanical properties through microstructure-based theories has been less extensive. These theories are essential for addressing the particle distribution within MREs and elucidating their intricate microstructural behaviors. Recent developments have seen hybrid models that integrate the advantages of different modeling approaches, promising more comprehensive analyses. Notable efforts by researchers [84-88] have aimed to unify continuum and microstructure theories, creating models that reflect both macroscopic and particle-scale phenomena. Furthermore, Nguyen et al. [89] advanced viscoelastic modeling by incorporating two-particle interaction elements into conventional phenomenological models, thereby enhancing the depiction of inter-particle dynamics and magnetic interactions.

Despite these advancements, current models still exhibit significant limitations. Continuum mechanics-based models, while providing clear physical insights, are primarily suitable for quasi-static conditions and often fail to capture the complex nonlinear behaviors that occur under dynamic loading conditions, including high strains and magnetic field intensities. Moreover, these models struggle to accurately represent the intricate interfacial interactions between particles and the matrix, which are critical for understanding the real-world performance of MREs. Conversely, phenomenological models, adept at predicting nonlinear viscoelastic behaviors through sophisticated curve fitting, rely heavily on empirical data. While they incorporate elements like friction, magnetic forces, and dampers to mimic physical phenomena, these models often lack a genuine representation of the underlying physical mechanisms, leading to discrepancies between modeling results and experimental observations.

Our research aims to bridge the gap between microscopic-based modeling and phenomenological approaches while aligning closely with experimental data through rigorous finite element modelings. Starting with a foundational two-particle dipole model to capture basic linear effects, we progressively expand our model to include complex chain structures, viscoelastic and hyperelastic properties, non-affine large deformations, and detailed interface behavior. We also explore instability phenomena within the material framework. Each enhancement is critically evaluated to determine its impact on overall simulation accuracy and robustness, with the goal of developing a versatile and precise model that can match and potentially surpass the capabilities of phenomenological models. Ultimately, we aim to not only emulate the accuracy observed in experimental setups but also to provide deep insights into the complex nonlinear behaviors noted in experiments, which have thus far eluded satisfactory explanation by existing models.

Chapter 3 Modeling and Simulation Methodologies for Magnetorheological Elastomers (MREs)

3.1 Introduction

In this chapter, we explore the various modeling and simulation methodologies employed to study the behavior of MREs. This includes detailed discussions on particle distributions, magnetic potential force calculation methods, mechanical and magnetic coupling approaches, boundary conditions, representative volume element (RVE) selection, and homogenization techniques. These methodologies are critical for accurately modeling the complex interactions within MREs, enabling the prediction and optimization of their properties for practical applications.

We begin by examining different particle distribution models, followed by the calculation methods for magnetic potential forces using both dipole and Maxwell methods. Then, we delve into the coupling of mechanical and magnetic responses under both small and finite deformation conditions. Subsequent sections cover the selection of boundary conditions and RVEs, culminating in an in-depth discussion on homogenization techniques, including the volume averaging and boundary traction methods. These foundational concepts and advanced methods provide a comprehensive framework for simulating MREs, setting the stage for the detailed evaluations presented in the following chapters.

3.2 Modeling of Particle Distribution

MREs represent a class of smart materials that have garnered substantial attention for their ability to alter mechanical properties in response to magnetic fields. This functionality is predominantly influenced by the internal structuring of magnetic particles within the elastomer matrix. The manufacturing process of MREs dictates the alignment and distribution of these particles, categorizing the elastomers into isotropic and anisotropic types. Isotropic MREs are characterized by a uniform distribution of particles without preferential alignment, offering consistent properties irrespective of the magnetic field direction. In contrast, anisotropic MREs exhibit a directional dependence due to the aligned particles, which enhances their response to magnetic fields aligned with the orientation of the particles.

The behavior of MREs under magnetic influence is critically dependent on the particle distribution within the matrix. To comprehensively understand the mechanics and dynamics of MREs, it is imperative to simulate various particle distributions and evaluate their influence on the material properties. This section delves into the modeling setups for three distinct types of particle distributions: random distribution, periodic distribution, and chain distribution.

3.2.1 Random Distribution

In the setup for random distribution, particles are randomly scattered throughout the matrix to simulate isotropic MREs, though this method can lead to variations in local particle density. We have devised two algorithms to construct the microstructure of MREs with such random distributions. The primary method is termed 'random placement.' Initially, a matrix is generated, and particles are then randomly inserted. Should a particle intersect with existing particles or come into contact with the boundary, it is relocated. This procedure is repeated until the specified particle count or volume fraction is reached. Figure 3.1 is a flowchart illustrating this method:

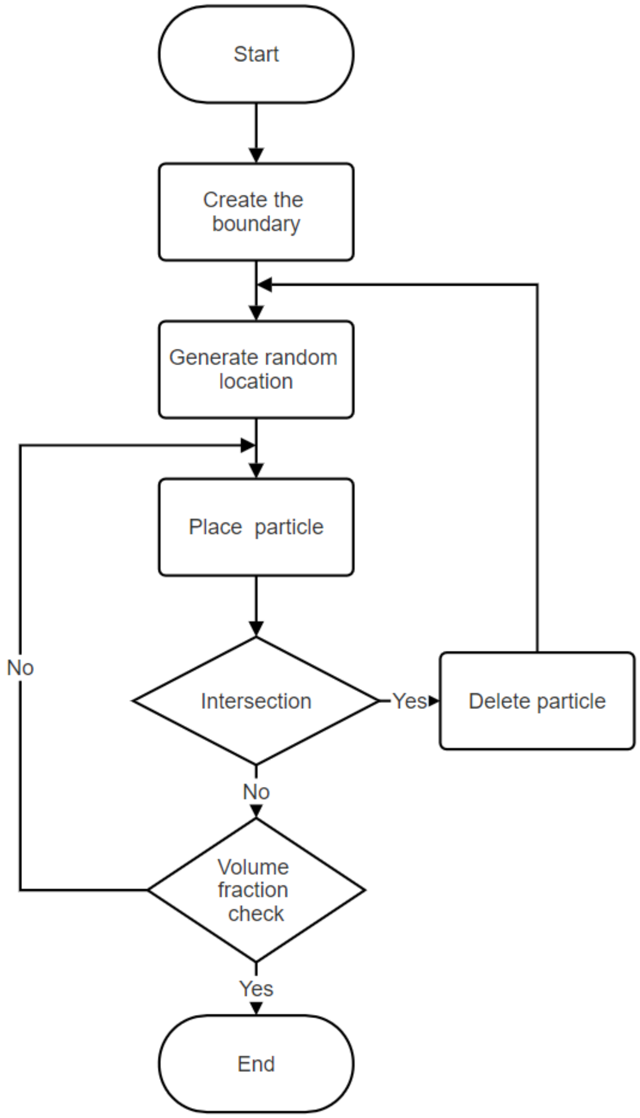

Figure 3.1 Flow chart of the random placement method for particle distribution in MRE simulations

The random placement method effectively generates MREs with random microstructures. Some examples of the generated microstructures are shown in Figure 3.2. These structures contain 16 particles each, with volume fractions ranging from 10% to 40%.

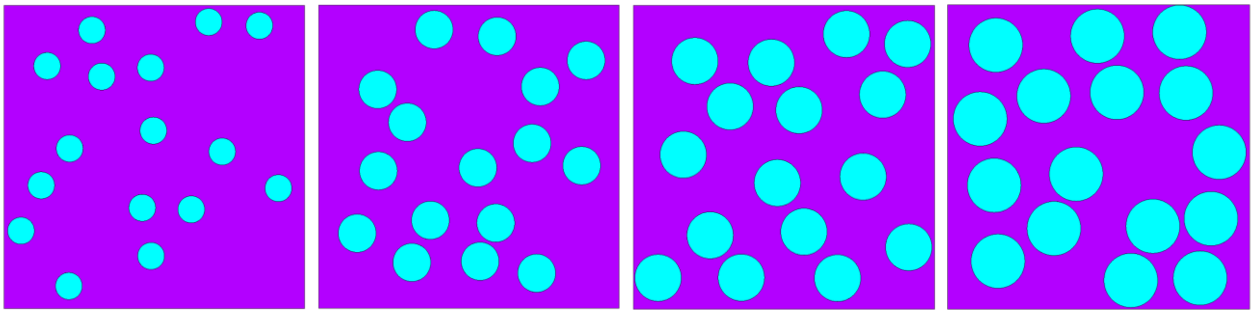

(a) (b) (c) (d)

Figure 3.2 A sketch of microstructure variations at different volume fractions using the random placement method. (a) 10% volume fraction, (b) 20% volume fraction, (c) 30% volume fraction, (d) 40% volume fraction.

The random placement method tends to become inefficient for higher volume fractions, notably those exceeding 50%. This method, while straightforward, requires frequent adjustments to avoid particle overlaps, making it increasingly cumbersome and less effective as the volume fraction rises. To enhance the efficiency of particle distribution, especially at higher densities, we employ an alternative referred to as the 'shaking method.' This technique starts with particles initially arranged in a densely packed, periodic pattern within the matrix, corresponding to the desired volume fraction. The matrix is then subjected to a process termed 'shaking,' where each particle can move randomly within predefined limits, ensuring no overlap with other particles or the matrix boundary. Each individual movement of a particle is termed a 'shake,' and achieving a genuinely random distribution requires at least hundreds of shakes of each of the particles.

For clarity, the procedural steps of the shaking method are outlined in a flowchart presented in Figure 3.3. Furthermore, to demonstrate the effectiveness of this method, Figure 3.4 shows the evolution of the particle distribution over several iterations at a 50% volume fraction. After 500 shakes, the arrangement distinctly diverges from its initial structured configuration, achieving randomness comparable to that produced by the random placement method, thus validating the efficacy of the shaking method in creating homogeneous and isotropic distributions in MREs.

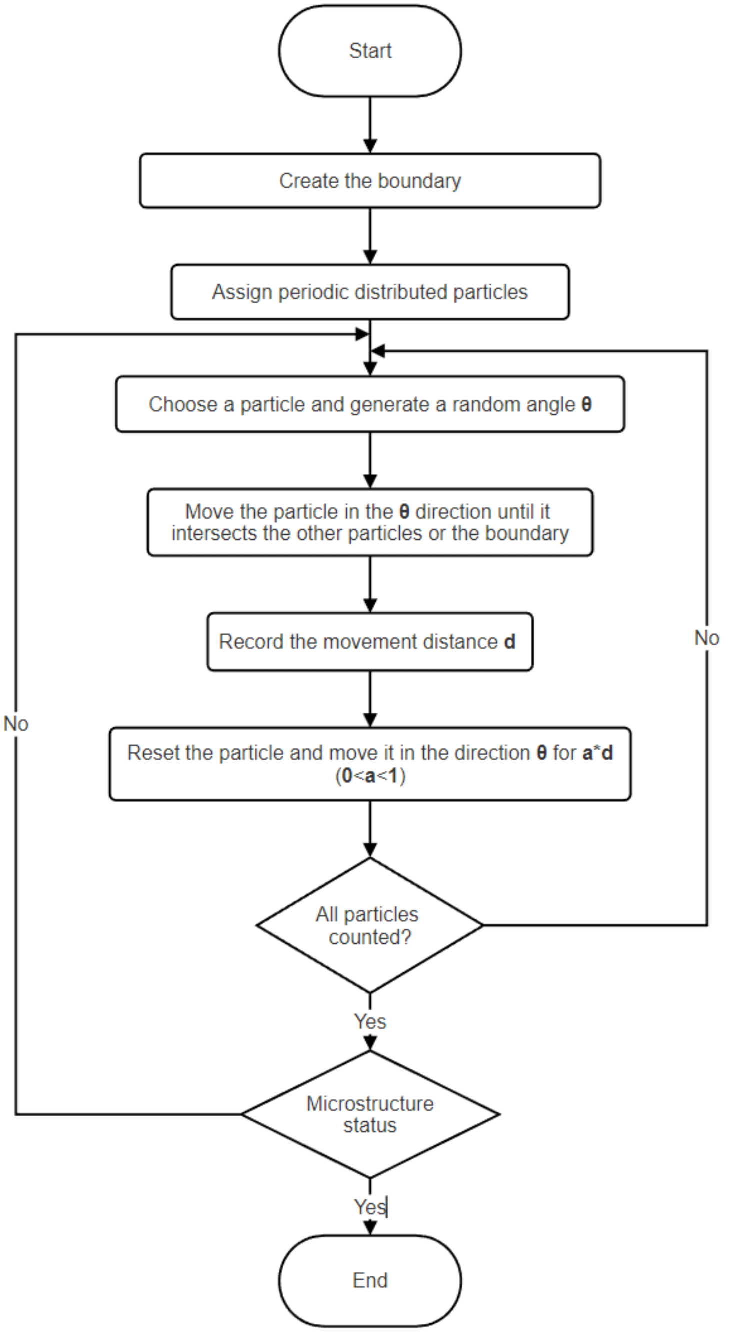

Figure 3.3 Flow chart of the shaking method for particle distribution in MRE simulations

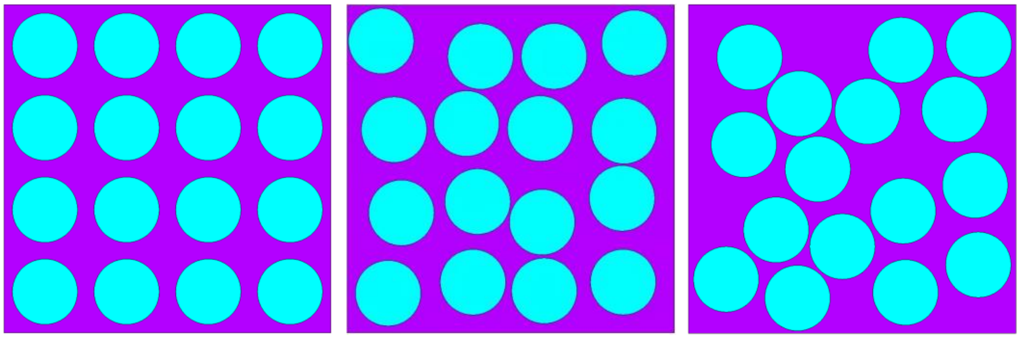

(a) (b) (c)

Figure 3.4 Microstructures of MREs generated by the shaking method at 50% volume fraction (a) initial square periodic distribution, (b) microstructure after 50 shakes, (c) microstructure after 500 shakes.

For modeling high volume fractions, we can utilize initial particle distributions like hexagonal periodic distributions that allow more dense packing, effectively handling scenarios with higher volume fractions. This approach is particularly beneficial when simulating conditions where close packing is crucial, although our current research does not focus on these high-volume fraction MREs. Thus, the random placement method, which efficiently meets our requirements, is predominantly used throughout our study.

In our simulations, we initially ensured that all particles were fully enclosed within the matrix without touching or intersecting the matrix boundaries. This approach simplifies the model's construction but may limit the randomness of the particle distribution, potentially affecting the simulation's fidelity to real-world MRE behaviors. To enhance the realism of our models, we have adapted our methods to allow for particle distributions where particles may intersect with the matrix boundaries. This adaptation is demonstrated in Figure 3.5, showing configurations where the particles extend to the edges of the matrix, increasing the randomness and potential applicability of our simulations in depicting more naturalistic particle arrangements.

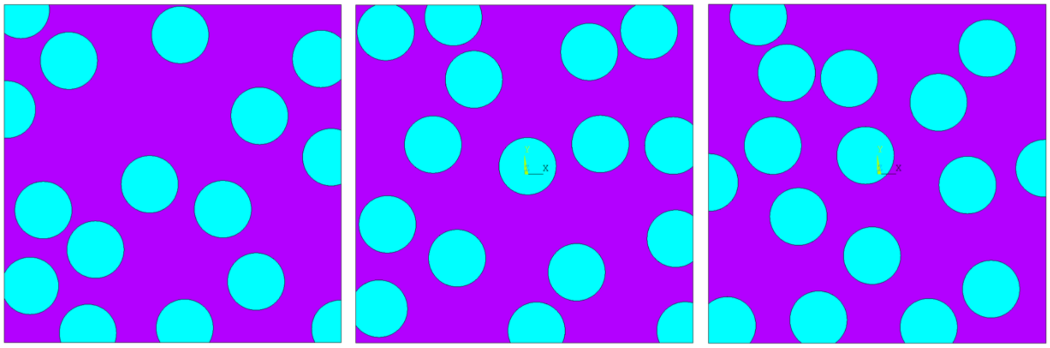

Figure 3.5 MREs featuring randomly distributed particles that intersect the matrix edges, with a volume fraction of 30%.

3.2.2 Periodic Distribution

Periodic particle distributions involve a systematic and repetitive placement of magnetic particles within the elastomer matrix, enhancing the predictability and uniformity of the material's mechanical properties. In our study, we focus on two specific types of periodic distributions: square and hexagonal. The square periodic distribution arranges particles in a grid-like pattern, forming a regular square lattice. This configuration allows for uniform spacing between particles but does not achieve maximum packing density. It is visually represented in Figure 3.6(a), where the simplicity and order of the square lattice are evident. On the other hand, the hexagonal periodic distribution, as depicted in Figure 3.6(b), features particles organized in a hexagonal lattice. This arrangement is known for its high packing efficiency and is often preferred in studies aiming to maximize particle density within the matrix. The hexagonal pattern, due to its close packing, potentially enhances the composite's mechanical properties by reducing the matrix's influence and allowing for more direct particle-to-particle interactions.

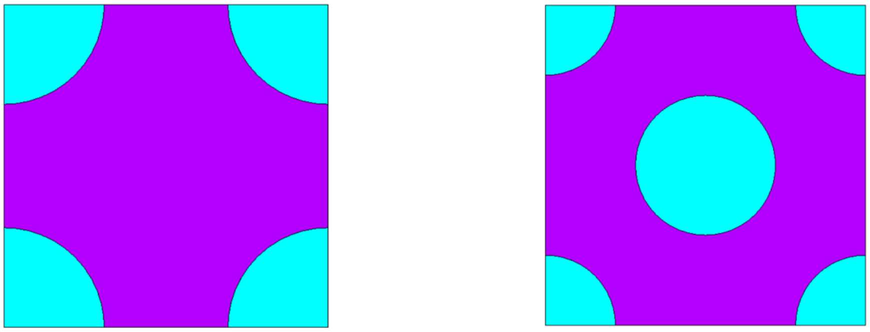

(a) (b)

Figure 3.6 Schematic representation of MRE composites with (a) a square and (b) a hexagonal distribution of particles.

3.2.3 Chain Distribution

The chain distribution in MREs is pivotal for understanding their anisotropic behaviors, especially under magnetic influence during the curing process. This configuration typically manifests in two distinct forms: straight and wavy chains, as illustrated in Figure 3.7, where (a) represents wavy chains and (b) depicts straight chains. Straight chain distributions, where particles are aligned in uninterrupted linear formations, are known to enhance the material's stiffness and magnetic responsiveness along the chain's axis. This alignment optimizes the MRE's mechanical properties under magnetic fields, offering pronounced improvements in both stiffness and damping capabilities. Conversely, real-world observations and micrographic analyses [69-71] often reveal that particle chains within MREs display a wavy rather than perfectly straight configuration. This waviness introduces complexities in the material's response to mechanical and magnetic stimuli. Simulation studies corroborate these findings, consistently demonstrating that wavy chains more accurately replicate the MR effects observed in experimental setups under both compression and tension modes. Therefore, while straight chains are ideal for theoretical studies due to their simplicity and enhanced magnetic properties, the inclusion of wavy chains in our analysis is essential.

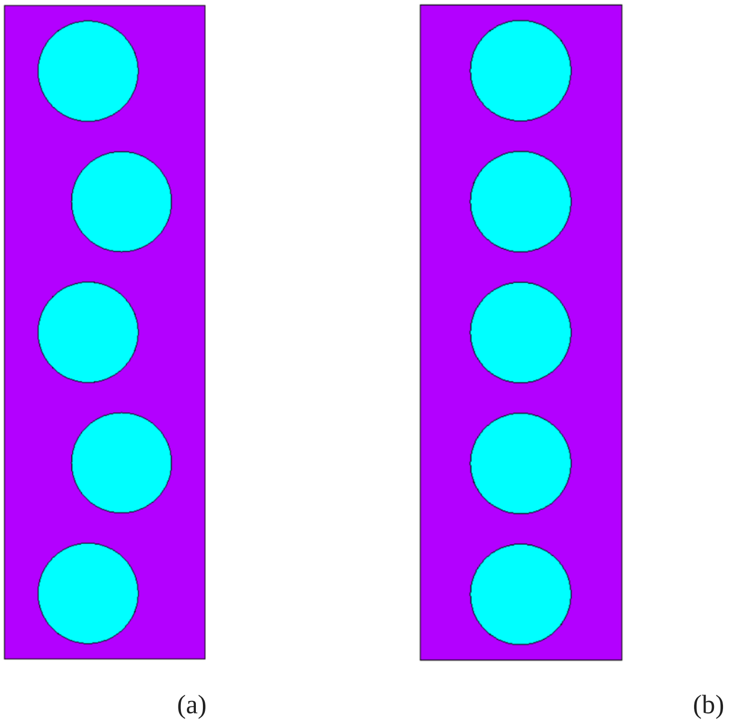

Figure 3.7 Schematic representation of MAE composites with (a) a wavy and (b) a straight chain distribution of magnetoactive particles in the matrix.

3.3 Magnetic Interaction of Particles

MREs possess unique properties that encompass both mechanical and magnetic aspects. Accurately modeling the behavior of MREs requires correctly applying the magnetic effects, as they significantly influence the overall performance of these materials. This section introduces the methods used to calculate the magnetic potential forces within MREs. This study employs two primary techniques: the Dipole method and the Maxwell method.

3.3.1 Dipole Method

The Dipole method is used to calculate the magnetic potential by modeling each magnetic particle in the elastomer matrix as a dipole. This method focuses on the interactions between these dipoles, determining the forces that arise from the magnetic fields generated by each particle. By assessing the effects of these interactions, the method provides insights into the forces exerted on particles within the field. The model considers the mutual influence of dipoles on each other, which is crucial for understanding the complex behavior of magnetic particles under various magnetic field conditions. A diagram illustrating this setup is shown in Figure 3.8, which depicts how the dipoles are positioned and interact within the matrix.

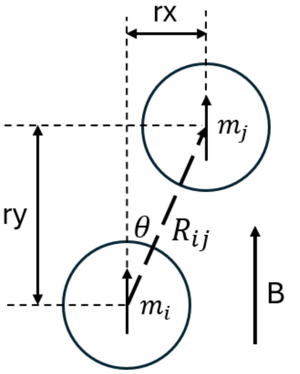

Figure 3.8 A schematic of the dipole interaction model.

The dipole method involves treating each magnetic particle embedded in the elastomer as an individual magnetic dipole. For spherical particles of the same size, the magnetic moment of each particle is given by the following equation:

$$\vec{m} = \frac{4}{3}\pi r^3 \vec{M} \,, \tag{3-1}$$

where $\vec{M} = \chi\vec{H}$, $\vec{M}$ is the magnetization, χ is the susceptibility, $\vec{H}$ is the magnetic field strength, and r is the radius of particles.

The magnetic potential energy between the magnetic particles i and j is as follows:

$$U_{ij} = -\frac{1}{4\pi\mu_r\mu_0}\left[\frac{3(\vec{m}_i\cdot\vec{R}_{ij})(\vec{m}_j\cdot\vec{R}_{ij})}{\left|\vec{R}_{ij}\right|^5} - \frac{(\vec{m}_i\cdot\vec{m}_j)}{\left|\vec{R}_{ij}\right|^3}\right], \tag{3-2}$$

where $\mu_0 = 4\pi \times 10^7 (H/m)$ is the vacuum permeability, $\vec{m}_i$ and $\vec{m}_j$ are the magnetic moments of particles i and j, $\vec{R}_{ij}$ is the direction vectors from particle i to particle j.

The magnetic forces can be obtained using the following equation:

$$F_{ij} = \vec{m} \cdot \nabla\vec{B}\,. \tag{3-3}$$

In the case of a two-dimensional plane problem, assuming that all the particles have the same magnetization intensity $\overrightarrow{m_\imath} = \overrightarrow{m_\jmath} = \vec{m}$, the two components of F_{ij} can be described using equations:

$$\overrightarrow{F_{\imath x}} = \frac{4\pi\mu_0\chi^2H^2r^6}{3\left|R_{ij}\right|^4}\left[(1 - 5\,cos^2\,\theta)\,sin\,\theta\right], \tag{3-4}$$

$$\overrightarrow{F_{\imath y}} = \frac{4\pi\mu_0\chi^2H^2r^6}{3\left|R_{ij}\right|^4}\left[(3 - 5\,cos^2\,\theta)\,cos\,\theta\right]. \tag{3-5}$$

3.3.2 Maxwell Method

The Maxwell method, in contrast, employs Maxwell's equations to compute the magnetic potentials, focusing on solving the magnetic field distribution within the MRE matrix. It then determines the forces exerted on each particle by integrating the Maxwell stress tensor over the particle's surface. This approach is grounded in magnetoelasticity theory, which posits that magnetic solids and conductors carrying electric currents undergo deformation when subjected to magnetic fields. The magnetic body force F^m can be obtained using the following equation [90]:

$$F^m = \oint_{\partial\Omega} \sigma^M \cdot n dS \ , \tag{3-6}$$

where Ω is the boundary of the particle, n is the boundary normal, and $\sigma^M$is the maxwell stress tensor, which can be described by the following equation:

$$\sigma^M = \frac{1}{2}(HB^T + BH^T - B^T HI) \ , \tag{3-7}$$

where H is magnetic field intensity vector, B is the magnetic flux density vector and I is the 2th rank unit tensor.

Both the dipole and Maxwell methods have distinct advantages and limitations. The dipole method is computationally simpler and less resource-intensive, making it suitable for systems with a low density of magnetic particles. However, its accuracy diminishes as particle concentration increases, as it approximates the magnetic interactions between dipoles. In contrast, the Maxwell method is more computationally demanding but provides a more detailed and accurate representation of the magnetic forces by considering the full magnetic field distribution and interactions. This makes it ideal for dense particle systems and more complex geometries.

3.3.3 Comparison of the Dipole and Maxwell Methods for Magnetic Interactions

We validated and compared the dipole and Maxwell methods using a simplified two-particle system to understand their effectiveness under controlled conditions. Calculations using the dipole method were carried out in MATLAB, focusing on scenarios with varied inter-particle distances to test the method's precision, especially where the dipole approximation might falter. Concurrently, the Maxwell method calculations were executed using the FEM software ANSYS, which allowed for a detailed analysis of magnetic field distributions and particle interactions. This comparative study, illustrated in Figure 3.9, aimed to identify the strengths and limitations of each method, particularly examining the dipole method's accuracy at shorter particle separations where its assumptions are most challenged. We placed two particles vertically along the y-axis and varied the inter-particle relative distance l from 2 to 5, where $l = ry/r$. For each value of l, we calculated the magnetic force using both methods and plotted the results, as illustrated in Figure 3.10.

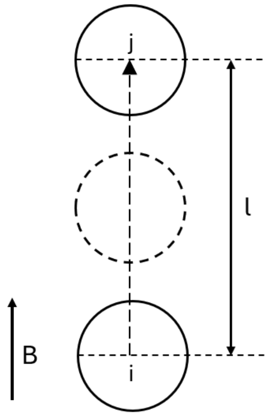

Figure 3.9 A schematic of the vertical interaction force model.

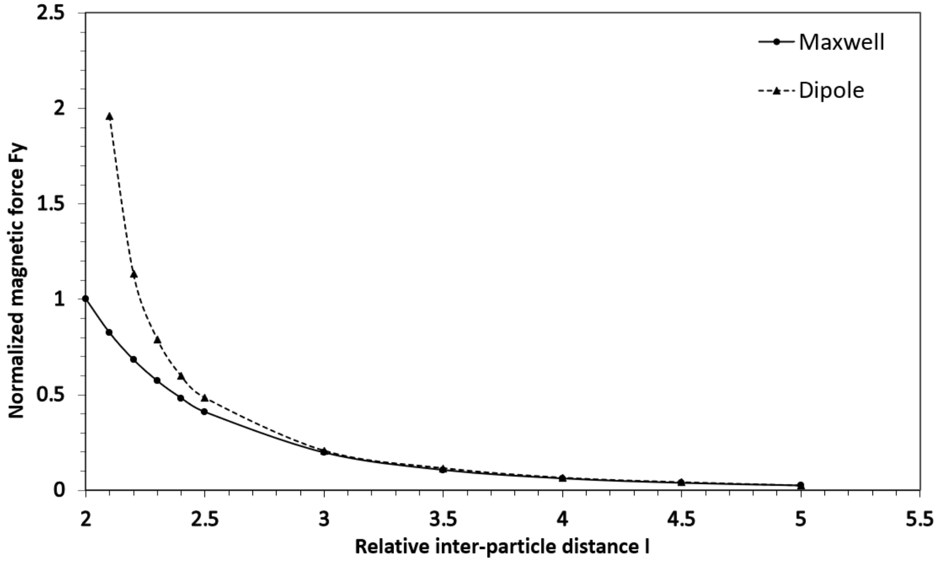

Figure 3.10 Normalized magnetic forces in the y direction as a function of l, with all forces normalized by dividing them by the magnetic force from the dipole model at l=2.

In this simulation, we plotted the normalized magnetic force F_y in the y-direction against the inter-particle distance l. Notably, the curve representing the Maxwell method begins at $l = 2.1$ instead of $l = 2$. This adjustment is necessary because when particles are in close proximity, the finite element method encounters difficulties in performing accurate calculations. These challenges are primarily due to numerical instabilities and limitations in mesh resolution.

A significant discrepancy is observed between the forces calculated using the Maxwell and dipole methods when the inter-particle distance l ranges from 2 to 2.5. If we consider the Maxwell method as the exact solution, it becomes evident that the dipole method is not suitable within this range due to its overestimation of the magnetic forces. As the inter-particle distance increases beyond $l = 2.5$, the differences between the two methods gradually diminish. This convergence suggests that the dipole method provides an effective approximation of the magnetic forces when the particles are sufficiently separated. Specifically, for $l > 2.5$, the results from the dipole method align more closely with those from the Maxwell method, indicating its utility as a computationally efficient alternative that offers reliable estimates in this expanded range.

Building on the previous conclusions, we sought to further evaluate the differences between the Dipole and Maxwell methods at an inter-particle distance of $l = 2.5$. To facilitate this investigation, we designed a model featuring a rotational particle arrangement, as depicted in Figure 3.11. This model allows for a detailed comparison under controlled variations in particle positioning, highlighting how each method responds to changes in the geometric configuration.

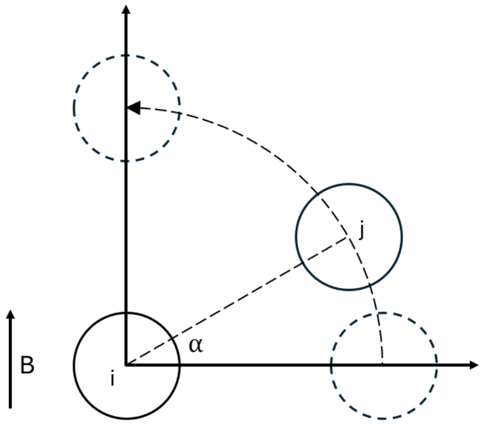

Figure 3.11 A schematic of the rotational interaction force model.

We initiated the experiment by positioning two particles along the x-axis, ensuring they were horizontally aligned. Subsequently, particle j was systematically rotated around particle i, achieving a 90-degree shift until the particles were aligned vertically. During this rotation, we maintained a constant inter-particle distance of 2.5r. For each position of particle j during its rotation, we meticulously calculated the magnetic forces exerted in both the x and y directions.

These calculations were performed using both the Dipole and Maxwell methods to capture comprehensive magnetic interactions at various angular orientations.

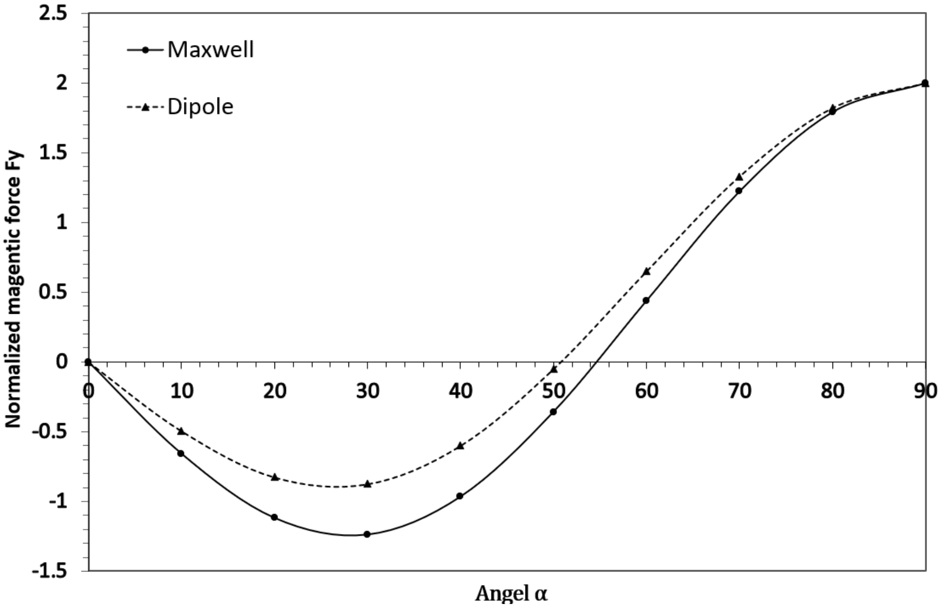

(a)

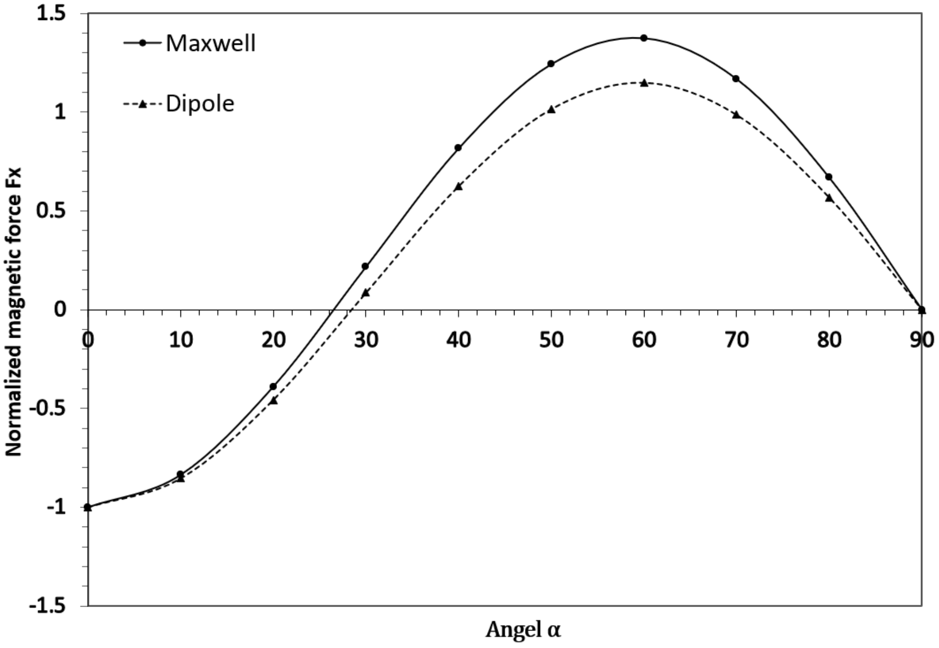

(b)

Figure 3.12 Normalized magnetic forces as a function of l (a) x component of the magnetic force, (b) y component of the magnetic force. All magnetic forces have been normalized by dividing them by the magnitude of magnetic force Fx calculated using the dipole model. The positive value indicates attraction, while the negative value indicates repulsion.

Figure 3.12 displays the outcomes from comparing the dipole and Maxwell methods as applied to the rotational model. Some crucial insights emerged from this comparison. Both methods yield consistent results when particles are aligned either vertically or horizontally, demonstrating the dipole method's reliability in these specific orientations. Nonetheless, notable discrepancies arise in the intermediate angles, particularly when the angle α between the particles shifts from 0 to 90 degrees. Here, the dipole method generally reports lower absolute magnetic forces in both the x and y directions when compared to the Maxwell method. The most significant divergence in the x-direction occurs at approximately α=60 degrees, where the dipole method underestimates the force by around 16%. Conversely, the largest discrepancy in the y-direction is seen at α=30 degrees, with a 29% underestimation. Similar phenomena have also been observed by other researchers [93, 94].

These findings underscore the dipole method's limitations in accurately capturing the complex dynamics of magnetic interactions at non-aligned angles. Despite these limitations, the method is remarkably effective for configurations such as straight or wavy chains where angles remain minimal, as well as for square periodic particle distributions. The dipole method offers a practical compromise between computational efficiency and accuracy in these scenarios. However, it falls short in more complex configurations like hexagonal periodic distributions or random particle orientations, where the Maxwell method's superior precision and comprehensive analytical approach make it the preferred choice for detailed and accurate magnetic interaction modeling.

3.4 Mechanical and Magnetic Coupling Methods

To accurately model MREs, it is crucial to consider the effects induced by both magnetic and mechanical fields. We approach this by categorizing strategies into two methods. Partial coupling treats the magnetic and mechanical effects as independent, simplifying the analysis but potentially overlooking interactions. Full coupling, on the other hand, acknowledges and incorporates the interdependence of these effects, ensuring a more comprehensive simulation of MRE behavior under various operational conditions.

3.4.1 Partial Coupling Method

The partial coupling method calculates the mechanical and magnetic responses independently and later combines them to assess the overall behavior of the material. This strategy is particularly effective under conditions of small deformations and low magnetic fields, where it is assumed that the deformation remains affine—uniform and directly proportional to the applied forces—and that the magnetic fields do not significantly alter the mechanical properties of the material. Utilizing the dipole method, the magnetic potential energy between each pair of dipoles can be expressed as follows:

$$E_{ij} = \frac{m^2\left(1-3\,cos^2\,\theta\right)}{4\pi\mu_1\mu_0 r^3}\;. \tag{3-8}$$

To accurately capture the changes of θ in the system, we relate the interparticle distances r_x and r_y based on the affine deformation assumption as shown below:

$$r_x = r_{x0}(1+\varepsilon_{11}) + r_{y0}(1+\varepsilon_{22})\varepsilon_{12}\;, \tag{3-9}$$

$$r_y = r_{y0}(1+\varepsilon_{22})\;, \tag{3-10}$$

$$cos\,\theta = \frac{r_y}{\sqrt{r_x^2+r_y^2}}\;, \tag{3-11}$$

where r_{x0} and r_{y0} are the initial interparticle distances in the x and y direction. According to the in compressibility of the matrix $\varepsilon_{11} = \left(\frac{1}{1+\varepsilon_{22}} - 1\right)$. The average potential energy over the volume can be calculated as follows:

$$U = \frac{1}{V}\sum_i^n \sum_j^n \frac{1}{2} E_{ij}\;. \tag{3-12}$$

The magnetic-induced modulus is therefore given by:

$$G_m = \frac{\partial^2 U}{\partial \varepsilon^2}\,. \tag{3-13}$$

By combining it with the mechanical simulation, we can obtain the coupled magnetic and mechanical properties.

In the partial coupling method, the mechanical response of the MRE is calculated based solely on the mechanical forces applied, while the magnetic response is assessed independently based on the influence of the magnetic field on the particles within the material. The total response is then determined by combining these two responses. This method is efficient for computational purposes and provides adequate accuracy under conditions of small deformations and low magnetic fields. However, its effectiveness decreases with increasing deformation and magnetic field strength, where the interactions between mechanical and magnetic effects become more significant.

3.4.2 Full Coupling Method

For scenarios involving finite deformations and stronger magnetic fields, the interdependencies between the mechanical and magnetic responses of the material become crucial, requiring the adoption of a full coupling approach. Under such conditions, the straightforward assumption of affine deformations is inadequate as the magnetic field may induce additional deformations. The full coupling method addresses these complexities through two main strategies: direct integration into finite element modelings and iterative magnetic force updates. Direct integration method involves embedding magnetic force calculations directly into the motion equations of finite element models. This allows for a concurrent assessment of both mechanical and magnetic effects on the material's behavior. The coupled kinematic equation is shown below:

$$\begin{bmatrix} [K]+[K^{uu}] & [K^{uA}] \\ [K^{uA}]^T & [K^{AA}] \end{bmatrix} \begin{Bmatrix} \{u\} \\ \{A\} \end{Bmatrix} + \begin{bmatrix} [C] & [0] \\ [0] & [0] \end{bmatrix} \begin{Bmatrix} \{\dot{u}\} \\ \{\dot{A}\} \end{Bmatrix} \tag{3-14}$$

$$+ \begin{bmatrix} [M] & [0] \\ [0] & [0] \end{bmatrix} \begin{Bmatrix} \{\ddot{u}\} \\ \{\ddot{A}\} \end{Bmatrix} = \begin{Bmatrix} \{F\} \\ \{J^S\}+\{J^{pm}\} \end{Bmatrix}.$$

The parameter $\{u\}$ represents the structural displacements while $\{A\}$ denotes the magnetic potential. The element structural stiffness matrix is denoted by $[K]$.$[K^{uu}] = \frac{\partial\{F^M\}}{\partial\{u\}}$ and $[K^{uA}] = \frac{\partial\{F^M\}}{\partial\{A\}}$ are the magnetic softening matrix and the magnetic Maxwell force coupling matrix. The element mass matrix is denoted by $[M]$, and the element magnetic reluctivity matrix is represented by $[K^{AA}]$. The element structural damping matrix is indicated by $[C]$. The vector of nodal and surface forces is represented by $\{F\}$. $\{J^S\}$and $\{J^{pm}\}$ are the element source current density and element remnant magnetization load vectors.

Alternatively, the iterative magnetic force update method operates by first calculating the magnetic response, which is then used to apply magnetic forces on the particles. Following this, the deformation of the particles is computed. This deformation data is used to update the magnetic forces in a recurrent manner. The process involves recalculating the magnetic forces at each time step, based on the latest deformation, and continues until the solutions converge within an acceptable error margin. This method is highly dependent on the number of substeps used; if nonlinear deformations are significant, any non-convergence in an early substep can adversely affect all subsequent steps. Thus, careful application and rigorous monitoring of convergence are critical when using this approach to ensure accuracy and stability in the simulations.

In summary, the choice between partial and full coupling methods depends on the deformation magnitude and the strength of the magnetic field. The weak coupling method is suitable for scenarios involving small deformations and low magnetic fields, offering computational efficiency and simplicity. In contrast, the strong coupling method is necessary for accurately modeling MREs under finite deformations and strong magnetic fields, capturing the intricate interactions between mechanical and magnetic responses.

3.5 Boundary Conditions and RVE Selection

This section explores the boundary conditions and the selection of the Representative Volume Element (RVE) that are fundamental to our simulations. Boundary conditions are categorized into magnetic and mechanical types, which are pivotal in relation to the coupling methods outlined in the preceding chapter. The choice of RVE is intricately linked to these boundary conditions, underscoring their importance in ensuring accurate and relevant simulation results.

The boundary conditions for our simulations are integral to accurately depicting the behavior of MREs under various mechanical and magnetic influences. These conditions are divided into mechanical and magnetic types, each tailored to align with the coupling methods discussed in the previous chapter. Mechanical boundary conditions typically involve the use of periodic boundary conditions, which are particularly effective for our purposes. These conditions allow the simulation to emulate a material behaving uniformly in all directions, effectively mimicking an infinite material. The periodic boundary conditions (PBC) are applied using the FEM according to the following relationships[91]:

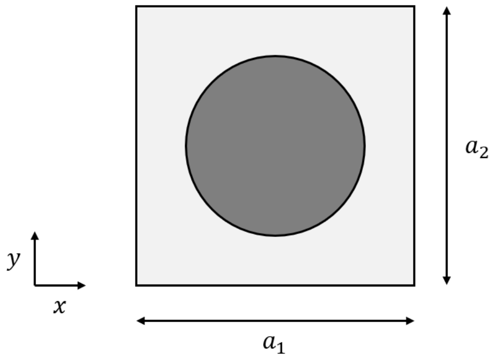

$$\begin{cases} u_1^R - u_1^L = \overline{\varepsilon_{xx}} a_1 \,, \\ u_2^R - u_2^L = \overline{\varepsilon_{yx}} a_1 \,, \end{cases} \tag{3-15}$$

$$\begin{cases} u_1^T - u_1^B = \overline{\varepsilon_{xy}} a_2 \,, \\ u_2^T - u_2^B = \overline{\varepsilon_{yy}} a_2 \,. \end{cases} \tag{3-16}$$

Figure 3.13 Periodic boundary condition of a single-particle RVE

The displacements of the nodes on the left and right faces (u^L and u^R), as well as those on the top and bottom faces (u^T and u^B), are coupled to create the periodic boundary conditions. The corner node requires careful measurement and the application of coupling equations on both faces to which it is attached.

Magnetic boundary conditions vary depending on the coupling method employed. For partial coupling, where the mechanical and magnetic responses are calculated separately, it is sufficient to select a suitable magnetic boundary condition independently. This flexibility allows for simpler simulations where the magnetic effects do not strongly interact with the mechanical deformations. However, the choice of boundary condition still needs to be carefully considered to avoid introducing artificial effects that could distort the simulation results.

In cases of direct integration, where magnetic and mechanical factors are strongly coupled, the magnetic boundary condition must be compatible with the mechanical boundary condition to accurately capture the interactions between the two fields. For these scenarios, periodic magnetic boundary conditions are essential. These conditions ensure that the magnetic field distribution remains consistent across the boundaries, similar to the mechanical field, thus preserving the integrity of the coupled simulation. To create a uniform magnetic field in the y direction, the following periodic magnetic boundary condition needs to be applied [92]:

$$\begin{cases} U^T = U^B + \overline{H} a_2 \\ U^L = U^R \end{cases}, \tag{3-17}$$

where $\overline{H}$ is the effective magnetic density. For simulations using the magnetic force method, the magnetic response is treated as a body force applied throughout the volume of the RVE rather than as a boundary condition applied at the edges. This approach models the internal forces generated by the magnetic particles and their interactions without constraining the field at the boundaries. However, this method requires careful RVE selection to minimize boundary effects. If the RVE is too small or improperly chosen, edge effects can significantly impact the results, leading to inaccurate predictions of the material behavior.

RVE selection is critical in simulations, as it must effectively represent the material's microstructure while managing computational complexity. For MREs, the RVE should include a diverse arrangement of magnetic particles to accurately reflect the influence of particle distribution on the material's properties. For periodic structures, we conducted two examples of the same distribution and volume fraction but different sizes as shown in Figure 3.14.

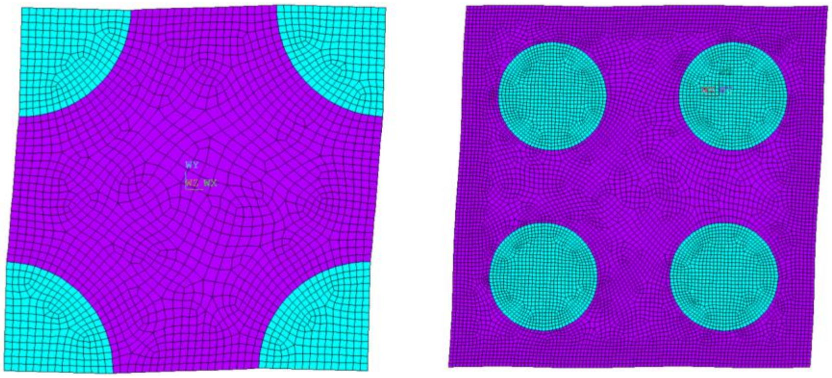

(a) (b)

Figure 3.14 RVE with 1% shear strain (a) RVE with quarter particles, (b) RVE with full particles.

We employ a square periodic distribution for the two RVEs under investigation. Periodic boundary conditions, coupled with a nominal shear strain of 1%, are utilized to facilitate the measurement of the effective shear modulus. The outcome reveals identical results across both RVEs, underscoring that variations in size do not influence the mechanical properties of the periodic structure. However, this consistency contrasts with the challenges posed by random distributions, where the application of periodic boundary conditions necessitates meticulous mesh adjustments.

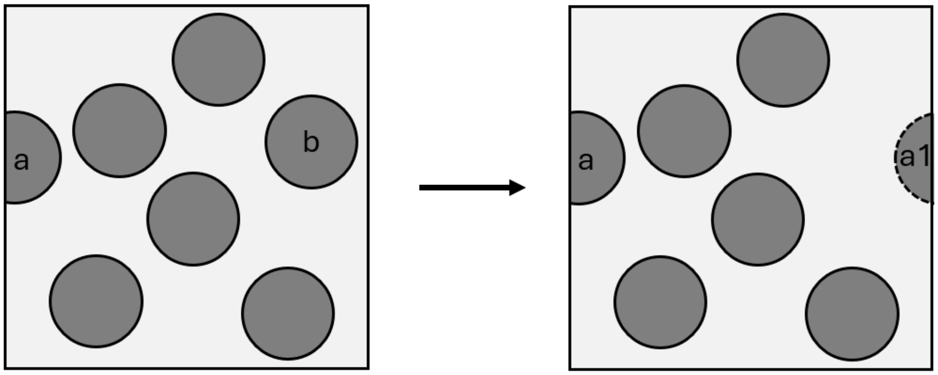

(a) (b)

Figure 3.15 Adjustments to RVE using periodic boundary conditions with boundary-intersecting particles: (a) initial random distribution, (b) distribution after spatial correction.

Figure 3.15 (a) illustrates the initial microstructure after generating an RVE with a random distribution. Notice that particle a a is located on the left boundary. To satisfy periodic boundary condition requirements, an identical particle a must be generated on the right boundary to maintain a consistent mesh. However, directly copying particle $a$to the right would cause it to intersect with particle b. Therefore, a decision must be made to either reassign the position of particle $a$or remove particle b. By removing particle $b$and copying particle a, we achieve the configuration shown in Figure 3.15 (b). It is apparent that the volume fractions in (a) and (b) differ. When a particle intersects a corner, the situation becomes more complex, requiring duplication on both adjacent boundaries.

To address the challenges associated with random particle distributions and PBC, we can employ a new RVE with a modified boundary condition approach. This method involves selecting a larger RVE that maintains the same particle distribution. Within this larger RVE, a smaller RVE of interest is delineated for detailed study. All homogenization processes and post-processing steps are conducted with reference to the boundaries of this smaller RVE. Since we are not required to apply PBC on the outer boundary of the larger RVE, there is no need for particle duplication or cancellation. This approach effectively resolves the issues introduced by manually adjusting the mesh, which can lead to disturbances in the material properties. By avoiding these modifications, we preserve the integrity of the original particle distribution and the inherent properties of the MRE. Prior research suggests that if the distance between the boundaries of the smaller RVE and the larger RVE exceeds a characteristic length (typically the average distance between the centers of two adjacent particles), the effects of the boundary can be disregarded. This ensures the accuracy of the results by minimizing boundary effects. Additionally, this method allows for a more straightforward and accurate representation of the material's behavior, as it avoids the complexities and potential inaccuracies associated with enforcing PBC on random distributions. A more detailed evaluation of this method, including specific examples and comparative analyses, will be presented in the next chapter. This evaluation will demonstrate how the modified boundary condition approach improves the reliability of simulation results for MREs with random particle distributions, providing a more robust framework for analyzing and optimizing these materials.

3.6 Homogenization Methods

In this section, we delve into the concept of homogenization and its application within the framework of computational micromechanics. Homogenization is a process used to derive the effective properties of a composite material by averaging its microstructural properties. This method is essential in computational micromechanics, which involves simulating the behavior of materials by considering their microstructure. By applying homogenization techniques, we can bridge the gap between the micro-scale interactions and the macro-scale response, enabling accurate predictions of material behavior under various loading conditions.

The basic principle of homogenization can be expressed through the volume averaging method. For a given microscopic stress σ_{ij} and strain ε_{ij}, the effective property of the composite material can be obtained by averaging the property over the volume of the representative volume element as shown below:

$$\overline{\varepsilon_{ij}} = \frac{1}{V}\int_V \varepsilon_{ij}\, dV \,, \tag{3-18}$$

$$\overline{\sigma_{ij}} = \frac{1}{V}\int_V \sigma_{ij}\, dV \,. \tag{3-19}$$

In the context of mechanical properties, the Hill-Mandel principle of macro-homogeneity is often used as a foundational concept. This principle states that the macroscopic work done by the average stress on the average strain in a representative volume element is equal to the volume average of the microscopic work done by the microscopic stress on the microscopic strain:

$$\langle\sigma\rangle : \langle\varepsilon\rangle = \frac{1}{V}\int_V \tilde{\sigma} : \tilde{\varepsilon} dV \,, \tag{3-20}$$

where σ and ε are the macro stress and strain, $\tilde{\sigma}$ and $\tilde{\varepsilon}$ are their microscopic counterparts. The angled brackets $\langle\cdot\rangle$ denote the volume average over the RVE. This principle is crucial because it ensures that the macroscopic behavior of the material is representative of the microscopic interactions within the RVE. The Hill-Mandel principle effectively links the micro-scale and macro-scale properties, providing a rigorous basis for homogenization.

In the context of considering magnetic forces in the homogenization process, the original equation needs to be updated to account for these additional forces. One way to do this is by treating the magnetic forces as body forces and adding extra terms in the homogenization equation to represent the magnetic forces. The First Piola–Kirchhoff stress tensor P_{ij} at the macro-scale can be calculated by:

$$P_{ij} = \frac{1}{V_\mu} \int_{V_\mu} \left(P_{ij}^{\mu} - f_j^{\mu} x_i \right) d\,V_\mu \,, \qquad (3\text{-}21)$$

where P_{ij}^{μ} is the microscopic First Piola–Kirchhoff stress tensor, V_μ is the volume of the RVE, f_j^{μ} is the magnetic body forces in the j-direction with a distance x_i to the central axis.

While this method is straightforward and can be effective for linear, small deformation cases, it has several disadvantages. For nonlinear, finite deformation cases, the inclusion of magnetic forces requires significant changes to the fundamental finite element method matrices to account for the nonlinear interactions between mechanical and magnetic fields. Additionally, this method is unable to adequately account for time-history effects, which are critical in dynamic simulations where the material response depends on its deformation history. To overcome these challenges, we employ an alternative method based on the divergence theorem, using boundary tractions to perform homogenization. This method offers precise results while being computationally efficient. The homogenization equation using the boundary traction method is given by:

$$P_{ij} = \frac{1}{V_\mu} \int_{\Gamma_\mu} t_j^{\mu} x_i d\,\Gamma_\mu \,, \qquad (3\text{-}22)$$

where Γ_μ is the boundary of the RVE and t_j^μ is the reactive boundary traction in the j-direction with a distance x_i to the central axis.

This approach simplifies the integration process, especially when dealing with complex microstructures and magnetic forces. By focusing on the boundary tractions rather than the volume stresses, the method bypasses the need to modify the internal FEM matrices for nonlinear effects. However, to ensure the accuracy of the calculations, it is crucial to place more nodes on the boundary of the RVE. This increased nodal density helps capture the detailed stress distribution along the boundary, ensuring that the computed tractions accurately represent the internal forces.

3.7 Conclusions

In Chapter 3, we explored the methodologies essential for accurately simulating MREs, beginning with the development of realistic microstructures that replicate the random and periodic particle arrangements found in these materials. We examined the role of magnetic interactions within these microstructures, comparing different approaches to understand how magnetic forces influence the overall behavior of MREs. The chapter also delved into the importance of coupling mechanical and magnetic responses, particularly emphasizing the need for a full coupling approach when dealing with significant deformations and strong magnetic fields. Additionally, we discussed the selection of appropriate boundary conditions and RVEs to ensure that simulations accurately reflect bulk material properties while balancing computational efficiency. Finally, we addressed the traction-based homogenization method, which is crucial for translating detailed microstructural behavior into effective macroscopic properties for dynamic simulation.

Chapter 4: Quasi-static Analysis of Magnetorheological Elastomers (MREs)

4.1 Introduction

This chapter is dedicated to validating and comparing various modeling and simulation methods for MREs under quasi-static conditions with a linear elastic matrix. Our primary goal is to evaluate the effectiveness of different modeling approaches in accurately predicting the behavior of MREs across a range of scenarios. Key topics include the initial verification of our homogenization process, in-depth comparisons of magnetic coupling methods, and practical considerations for selecting between 3D and 2D models. Additionally, we explore the impact of chain structures on the MR effect and assess how particle distribution influences simulation outcomes. This comprehensive analysis provides valuable insights for optimizing MRE simulations and guides the selection of appropriate methods for future research.

4.2 Sanity Check

The sanity check serves as an essential preliminary step to confirm that the homogenization process, facilitated by finite element modeling, is implemented accurately. Before diving into complex simulations, it's critical to verify that the RVE is constructed correctly and that the homogenization process yields valid results. To conduct this sanity check, we adjust the properties of the particles within the RVE to match those of the matrix material, effectively rendering the RVE homogeneous. This method ensures uniform properties throughout the material, simplifying the verification process. If the homogenization is functioning as intended, the effective properties derived from this homogenized RVE should align precisely with the known properties of the matrix. We carry out this verification by applying volume averaging and other suitable homogenization techniques to determine the effective properties of the material. This step is fundamental in establishing a reliable foundation for more detailed and specific simulations that follow.

For transversely isotropic materials, the effective stress and strain are related through the stiffness tensor as follows:

$$\begin{Bmatrix} \overline{\sigma_1} \\ \overline{\sigma_2} \\ \overline{\sigma_3} \\ \overline{\sigma_4} \\ \overline{\sigma_5} \\ \overline{\sigma_6} \end{Bmatrix} = \begin{bmatrix} C_{11} & C_{12} & C_{12} & 0 & 0 & 0 \\ C_{12} & C_{22} & C_{23} & 0 & 0 & 0 \\ C_{12} & C_{23} & C_{22} & 0 & 0 & 0 \\ 0 & 0 & 0 & (C_{22} - C_{23})/2 & 0 & 0 \\ 0 & 0 & 0 & 0 & C_{66} & 0 \\ 0 & 0 & 0 & 0 & 0 & C_{66} \end{bmatrix} \begin{Bmatrix} \overline{\varepsilon_1} \\ \overline{\varepsilon_2} \\ \overline{\varepsilon_3} \\ \overline{\gamma_4} \\ \overline{\gamma_5} \\ \overline{\gamma_6} \end{Bmatrix} . \tag{4-1}$$

The coefficient in the **C** are found by setting up FEM models with different boundary conditions. The following boundary conditions are used [95]:

$$\varepsilon_1 = 1; \varepsilon_2 = \varepsilon_3 = \gamma_4 = \gamma_5 = \gamma_6 = 0 \, , \tag{4-2}$$

$$\varepsilon_2 = 1; \varepsilon_1 = \varepsilon_3 = \gamma_4 = \gamma_5 = \gamma_6 = 0 \, , \tag{4-3}$$

$$\gamma_4 = 0; \varepsilon_1 = \varepsilon_2 = \varepsilon_3 = \gamma_5 = \gamma_6 = 0 \, . \tag{4-4}$$

Once these components have been determined, the elastic properties of the homogenized RVE can be computed by:

$$E_1 = C_{11} - \frac{2C_{12}^2}{C_{22}+C_{23}}, \tag{4-5}$$

$$E_2 = \frac{[C_{11}(C_{22}+C_{23})-2C_{12}^2](C_{22}-C_{23})}{C_{11}C_{22}-C_{12}^2}, \tag{4-6}$$

$$\upsilon_{12} = \frac{C_{12}}{C_{22}+C_{23}}, \tag{4-7}$$

$$\upsilon_{23} = \frac{C_{11}C_{23}-C_{12}^2}{C_{11}C_{22}-C_{12}^2}, \tag{4-8}$$

$$G_{12} = C_{66}, \tag{4-9}$$

where E_1 and E_2 are the longitudinal and transversal Young's moduli; υ_{12} and υ_{23} are the the longitudinal and transversal Poisson's ratios; G_{12} is the longitudinal shear modulus. After acquiring these properties, we conduct a comparison with the initially defined properties of the matrix. If the effective properties coincide with those of the matrix, it validates both the construction of the RVE and the accuracy of the homogenization process. This sanity check also includes verifying that the boundary conditions are appropriately applied and that the finite element mesh is sufficiently refined. Ensuring correct boundary conditions and high-quality mesh resolution is crucial to prevent numerical errors that might skew the results of the homogenization. Although subsequent sections may not explicitly mention it, this sanity check is a standard procedure conducted whenever there are modifications to the boundary conditions or the material properties of the matrix. This ongoing verification ensures the integrity and accuracy of our FEM analyses, thereby supporting the dependability of the modeling outcomes.

4.3 Comparative Analysis of Various Modeling Techniques

4.3.1 Comparison of Force and Energy Methods

In Chapter 3, we introduced both full and partial coupling methods, which differ primarily in whether they account for the interplay between magnetic and mechanical deformations. Additionally, there are several approaches to integrating magnetic influences into mechanical models, and we will explore two such methods in detail. The Magnetic Body Force Method (MBFM) applies magnetic responses directly as body forces on the particles, whereas the Magnetic Potential Energy Method (MPEM) calculates the potential energy from the magnetic field using small affine deformations, derives the magnetic-induced modulus, and integrates this with the mechanical modulus of the composite.

Finite element simulations were conducted using a periodic square distribution RVE to compare and validate these methods. Both approaches employed the dipole model to ensure consistent magnetic response calculations. A range of shear strains from 1% to 10% was applied to both models, allowing for the measurement of the effective shear modulus at various strain levels. The influence of the magnetic field on the shear modulus was assessed and is depicted in Figure 4.1. The same magnetic fields, material properties, and boundary conditions were maintained across both simulations to ensure a fair comparison of the two methods.

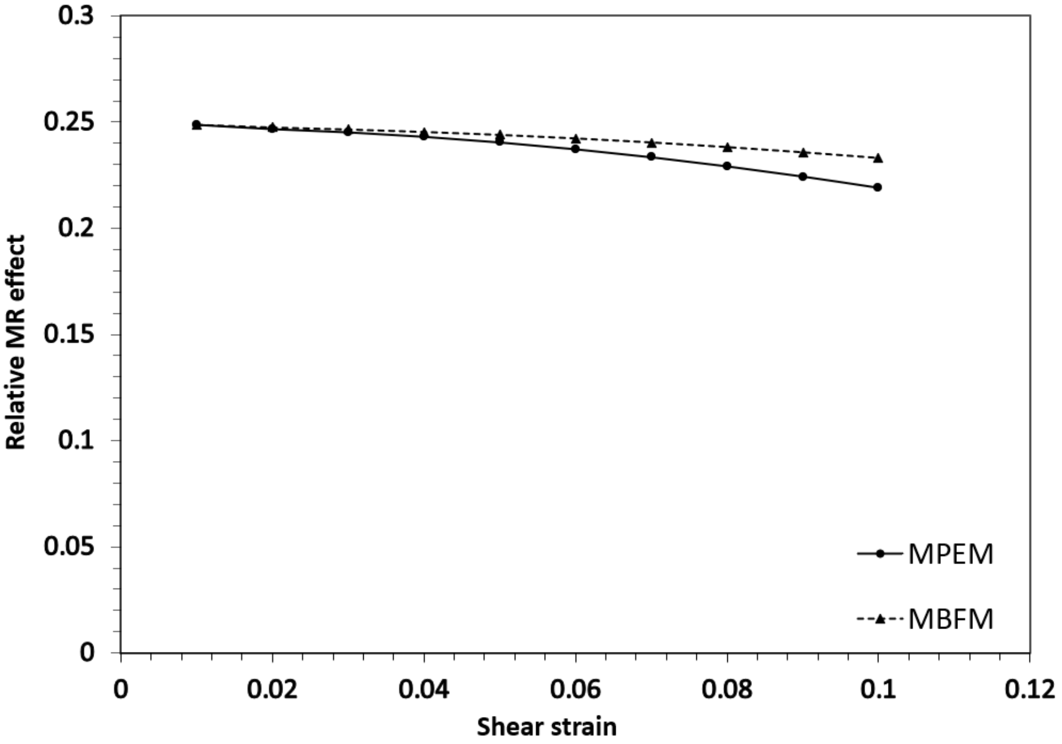

Figure 4.1 The effect of shear strain amplitude on relative MR effect for body force method and energy method.

From the results, it is evident that the relative MR effects of both methods are almost identical at a small shear strain of 1%. This agreement at lower strains indicates that both coupling methods can accurately capture the initial response of the material. However, as the strain increases, the differences between the methods become more pronounced. This discrepancy may be attributed to several factors, including the FEM mesh quality or the specific boundary conditions applied. In the RVE used, particles are bisected and located on the RVE boundary, causing parts of the particles to be constrained by the periodic boundary condition. When applying body forces, it is crucial to avoid the boundary regions since they are already constrained. This precaution may lead to eccentric effects as the shear strain increases, contributing to the growing difference observed between the two methods at higher strain levels.

Despite these potential issues, the difference between the methods is about 6% at a shear strain of 10%. This indicates that both methods are reliable and nearly identical for small deformation situations, as they are built under the affine deformation assumption. However, as the strain increases, the affine deformation assumption becomes invalid, and the accuracy of these methods may be compromised. For finite strains, where the deformation is nonlinear and more complex interactions occur, other methods need to be employed to accurately predict the material behavior.

4.3.2 Comparison of 2D and 3D Models

In this section, we explore the usage of three-dimensional models versus two-dimensional models in simulating the behavior of MREs. Due to the presence of particle chains, MREs are typically treated as transversely isotropic materials. Unlike fiber-reinforced composites, where the reinforcing elements are often elongated fibers, the particles in MREs are spherical. This distinction makes it challenging to directly convert 3D models into 2D representations, necessitating a detailed comparison between the two modeling approaches. A meshed 3D model of the square periodic distribution is shown in Figure 4.2.

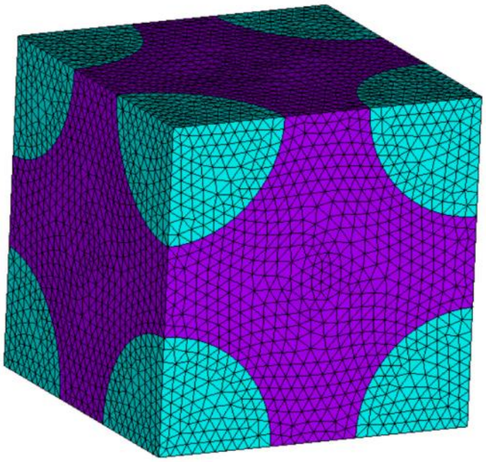

Figure 4.2 3D RVE showcasing a square periodic distribution, generated using ANSYS.

For 3D modelings, the application of PBCs is more complex. The faces, edges, and corners of the RVE need to be paired separately according to the deformation, ensuring that the RVE accurately represents the infinite material. Additionally, to prevent rigid body motion, specific displacement constraints must be applied to the corner nodes. These constraints are crucial for maintaining the stability and accuracy of the simulation. In contrast, 2D models involve simpler PBCs, typically applied to the boundaries of the 2D plane. The volume fraction is an important consideration due to the spherical shape of the particles. Under the same volume fraction and RVE size, the radius of the particles will differ between 3D and 2D models. This difference affects both the mechanical and magnetorheological properties of the material. In 3D models, the actual spatial arrangement and interaction of the spherical particles can be accurately captured, leading to more realistic simulations of the MR effect and mechanical behavior. In 2D models, particles are often represented as circles, and the packing density can differ significantly from the 3D case. This discrepancy can lead to variations in the predicted properties, as the interactions are simplified and may not fully capture the complexity of the three-dimensional particle network. The mechanical and magnetorheological effects in 3D models are influenced by the full spatial arrangement of the particles. This allows for a more comprehensive analysis of the stress distribution, deformation patterns, and magnetic interactions. The 3D nature of the particles and their interactions is critical for accurately predicting the material's response under various loading and magnetic field conditions. In 2D modelings, these effects are simplified, potentially overlooking important out-of-plane interactions and stresses.

However, given that we are only applying the load on the x-y plane of the model, the out-of-plane response is not as critical. Our primary objective is to measure the influence of different microstructural parameters on the behavior of MREs, rather than achieving highly precise simulations. And for this purpose, 2D models are sufficient. This approach significantly reduces the meshing requirements and computational time, making the simulations easier to converge. While this simplification might not be significant in linear simulations, it becomes crucial for later simulations involving interactions, buckling, and finite deformation, where computational efficiency is essential. A comparison of 2D and 3D models for hysteresis simulation will be presented in the next chapter.

4.3.3 Comparison of Random and Periodic Distribution

In this section, we aim to study the behavior of MREs with different particle distributions under a magnetic field. Utilizing the assumption of the partial coupling method, the magnetic response and mechanical response can be treated separately. Here, we focus specifically on the mechanical response, examining the effective shear modulus. To perform this analysis, we generate 100 RVEs with random particle distributions, each containing 16 particles with a volume fraction of

30%. A 1% shear strain is applied as the boundary condition. The effective shear modulus of these RVEs is calculated without applying a magnetic field to isolate the mechanical properties. In addition to the random distribution RVEs, the effective shear modulus for two periodic particle distribution RVEs discussed previously is also calculated. For reference, we include results from two analytical methods: the Hashin-Shtrikman lower bound (HSB-L) and the Self-Consistent Method (SCM).

The Hashin-Shtrikman lower bound provides a theoretical minimum for the effective modulus of composite materials. It assumes an idealized microstructure where the particles are perfectly dispersed within the matrix. The HSB-L for the shear modulus is given by [96]:

$$G_{HSB-L} = G_m + \frac{V_p(G_p - G_m)}{1 + \frac{V_m(G_p - G_m)}{G_p + G_m}}, \tag{4-10}$$

Where G_m is the shear modulus of the matrix, G_p is the shear modulus of the particles, V_m is the volume fraction of the matrix, and V_p is the volume fraction of the particles. For composites with hard inclusions like MREs, another method proposed by G. J. Weng [97] is able to yield identical results.

The Self-Consistent Method [98,99] is another analytical approach that estimates the effective properties of composite materials. It assumes that each phase in the composite behaves as if it were embedded in an effective medium whose properties are those of the composite. The effective shear modulus G_{SCM} is found by solving the following equation:

$$G_{SCM} = G_m + \frac{V_p(G_p - G_{SCM})}{1 + \frac{G_{SCM}(G_p - G_m)}{G_m(G_p + G_m)}}, \tag{4-11}$$

The results are summarized in Figure 4.3. According to the results, the effective shear modulus of the RVEs with random microstructures falls between the HSB-L and SCM estimates. This finding aligns with previous research, as the HSB-L typically provides a lower estimate, while the SCM tends to overestimate the effective modulus.

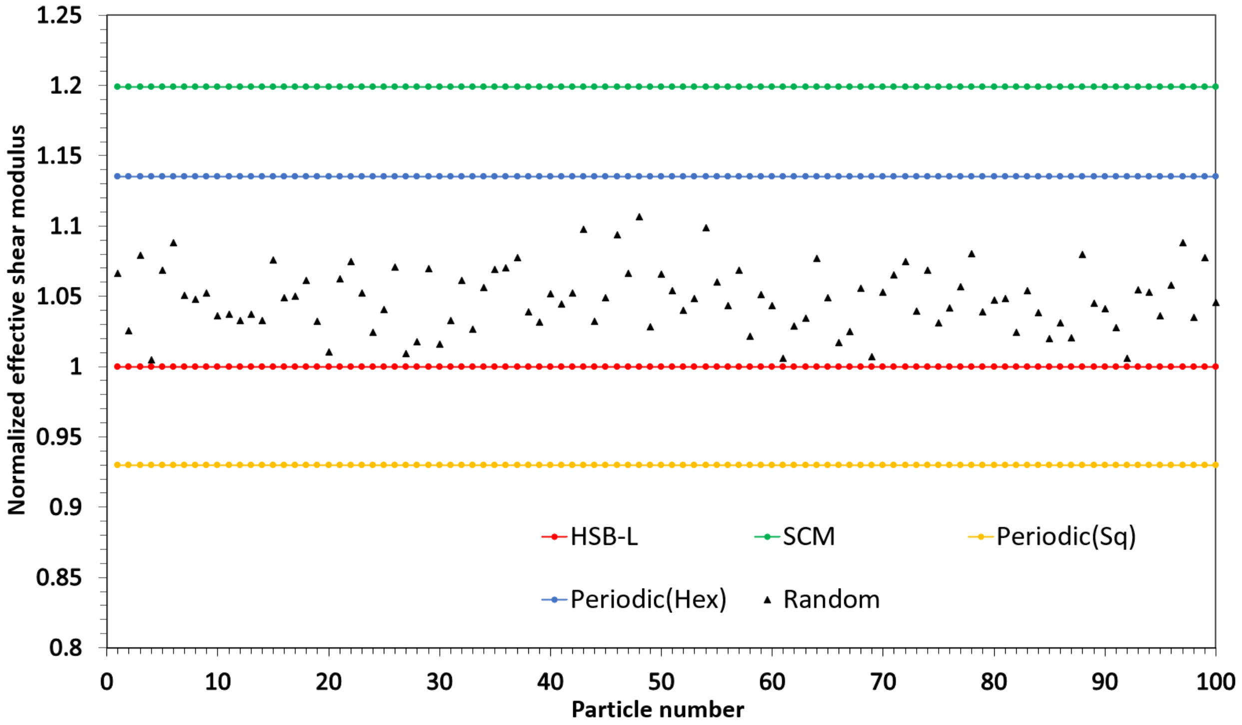

Figure 4.3 Effective shear modulus comparison for RVEs with random and periodic distribution.

According to the results, the effective shear modulus of the RVEs with random microstructures falls between the HSB-L and SCM estimates, aligning with previous research findings. This range indicates that the random distributions offer a realistic representation of the material's behavior, reflecting the variability and complexity inherent in actual MRE structures.

Additionally, the variation of the effective shear modulus due to the distribution is a maximum of

10%, which is relatively small and indicates a stable mechanical performance across different random configurations.

Interestingly, the two periodic distribution RVEs exhibit significant differences. The hexagonal periodic distribution, with a value of 1.13, exceeds the SCM estimate, suggesting an overestimation of the modulus due to the idealized arrangement. Conversely, the square periodic distribution, with a value of 0.93, falls below the HSB-L estimate. This deviation implies that periodic particle distributions may not be representative of the actual behavior of MREs in practical applications, where such ordered patterns are unlikely to occur naturally. Consequently, it is crucial to carefully consider the particle distribution used in modelings. Relying on periodic patterns might not provide an accurate depiction of the mechanical properties of MREs, and selecting appropriate microstructural models is essential for accurately predicting their behavior. The magnetic response is calculated separately from the mechanical response. While the mechanical response, represented by the shear modulus, remains relatively stable across different particle distributions, the MR effect in random distributions exhibits considerable instability, with significant variations depending on the specific particle arrangements. This variability is characterized by both positive and negative MR effects, indicating a wide range of responses to the applied magnetic field. Such significant fluctuations suggest that random distributions might not be ideal for detailed, consistent studies of the MR effect due to their inherent unpredictability.

Previous research has shown that the MR effect is most pronounced when particles are aligned in chain-like structures. These chain structures facilitate stronger magnetic interactions, leading to a more substantial and predictable MR effect. Therefore, to achieve more reliable and detailed studies of the MR effect, we focus on using RVEs with chain structures. It allows for a more controlled and systematic investigation of the MR effect, providing insights that are more applicable to real-world applications where predictable and robust MR behavior is desired.

4.4 Analysis of MREs with Chain Structures

In this section, we delve into modelings leveraging chain structures to examine the MR effect. Chain structures significantly amplify the MR effect due to the robust magnetic interactions among aligned particles. We discuss various RVEs designed for these structures and adopt the body force method to apply magnetic responses as body forces. The modelings consider two scenarios regarding chain length: entire chain and partial chain. The entire chain model treats the chain within the RVE as isolated, disregarding any interactions with particles outside the RVE. This simplifies the analysis but may not capture all realistic interactions. In contrast, the partial chain model views the chain inside the RVE as part of a larger continuum within the MRE. This requires implementing periodic magnetic boundary conditions to simulate the effects of external particles, enhancing the realism of the modelings.

For our detailed analysis, we primarily utilize the entire chain assumption for the body force method modelings, ensuring clarity in observing the direct impacts of internal magnetic forces. Additionally, we conduct supplementary modelings that explore the magnetic boundary effects, confirming the influence and ensuring a comprehensive understanding of the magnetic response across different chain configurations.

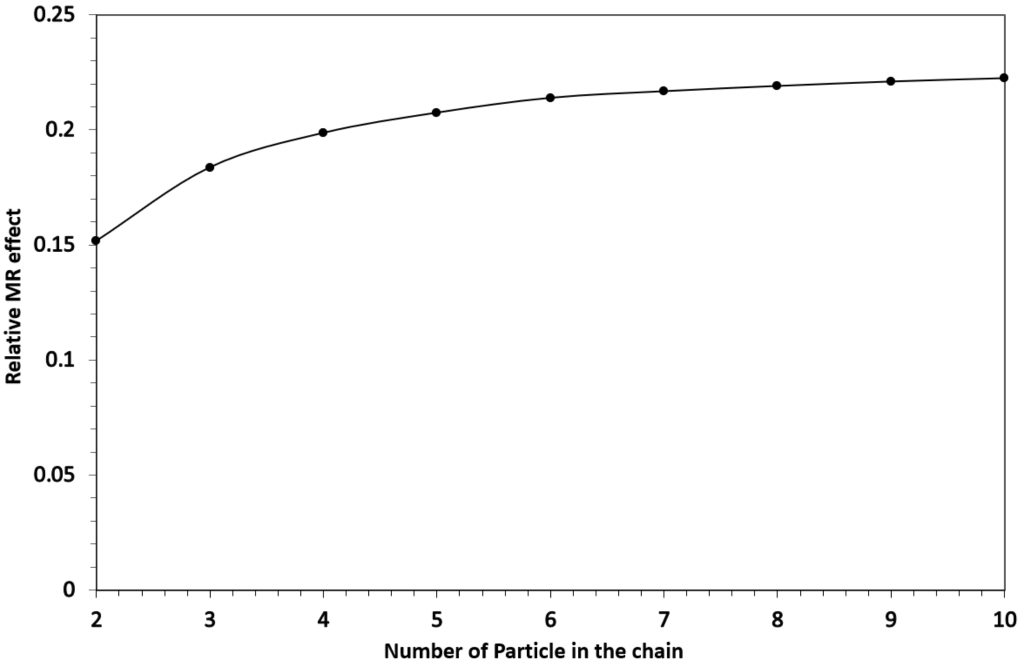

Figure 4.4 Relative MR effect for straight chain RVEs with varying particle numbers.

We begin with an RVE containing two particles forming a straight chain and incrementally increase the number of particles up to ten while keeping the volume fraction constant. The relative MR effects for these configurations are calculated and shown in Figure 4.4. The results indicate that the relative MR effect increases significantly when the number of particles in the chain is small. Specifically, the MR effect exhibits a steep rise as the chain lengthens from two to four particles. However, as the number of particles increases beyond four, the rate of change in the MR effect diminishes, and the curve tends to flatten. This suggests that beyond a certain number of particles, the additional length of the chain has a reduced impact on the MR effect. Based on these observations, we select a chain model with at least four particles for subsequent modeling and simulations. This ensures that the model includes enough particles to accurately represent the real situation in MREs while maintaining computational efficiency.

Besides, we explore the MR effect using a two-particle interaction model under shear deformation. This model allows us to examine the differences in MR effect between straight and wavy chains and how the MR effect changes with increasing shear deformation. Additionally, we consider the impact of chain-to-chain interactions. We build a two-particle interaction model as shown in Figure 4.5. Similar to the previous setup, we initially place two particles vertically aligned. Instead of rotating the second particle, we move it horizontally to the right to simulate wavy chains or changes in position under shear deformation. Under affine shear deformation in the x-direction, the MR effect is primarily influenced by the x-component of the magnetic interaction force Fmx. By taking the derivative of Fmx, we can estimate how the MR effect changes with the relative distance between the particles.

The results of these simulations are shown in Figures 4.6. The x-values are normalized according to the maximum positive value, and the y-axis represents the distance ratio q, where $q = \frac{r_x}{r_y}$. Positive x-values indicate attraction, while negative x-values indicate repulsion.

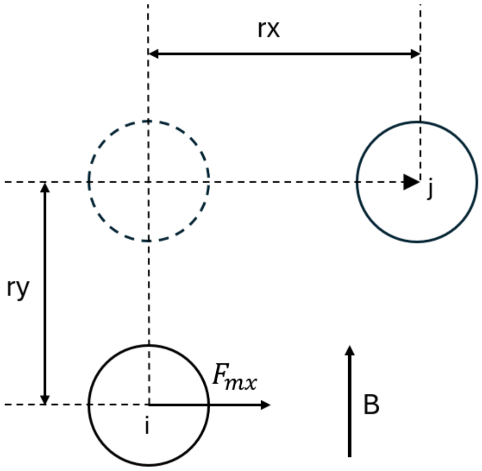

Figure 4.5 A sketch of the 2 particle interaction model under shear deformation.

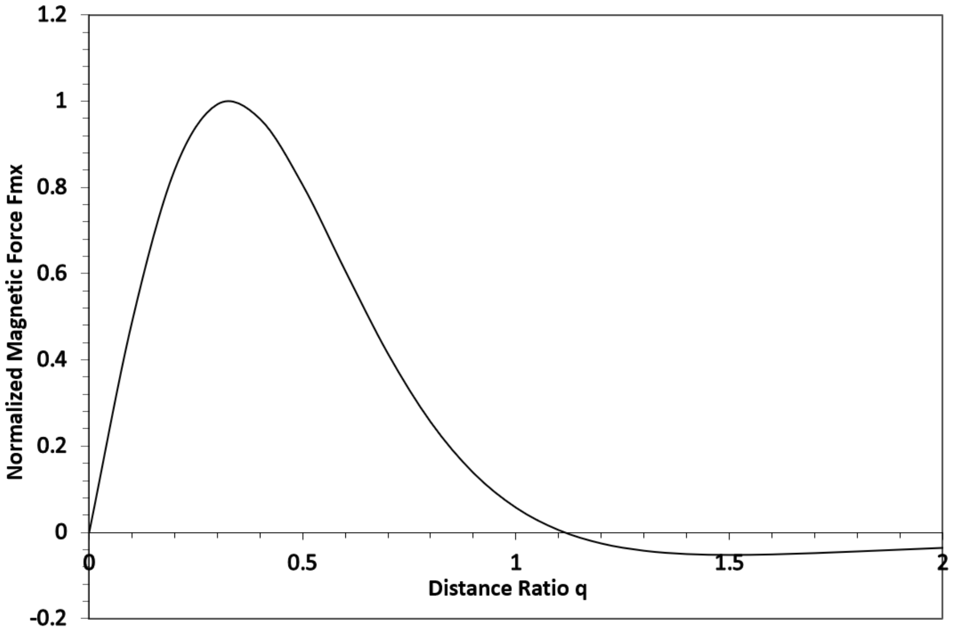

Figure 4.6 Normalized magnetic force Fmx vs. distance ratio q.

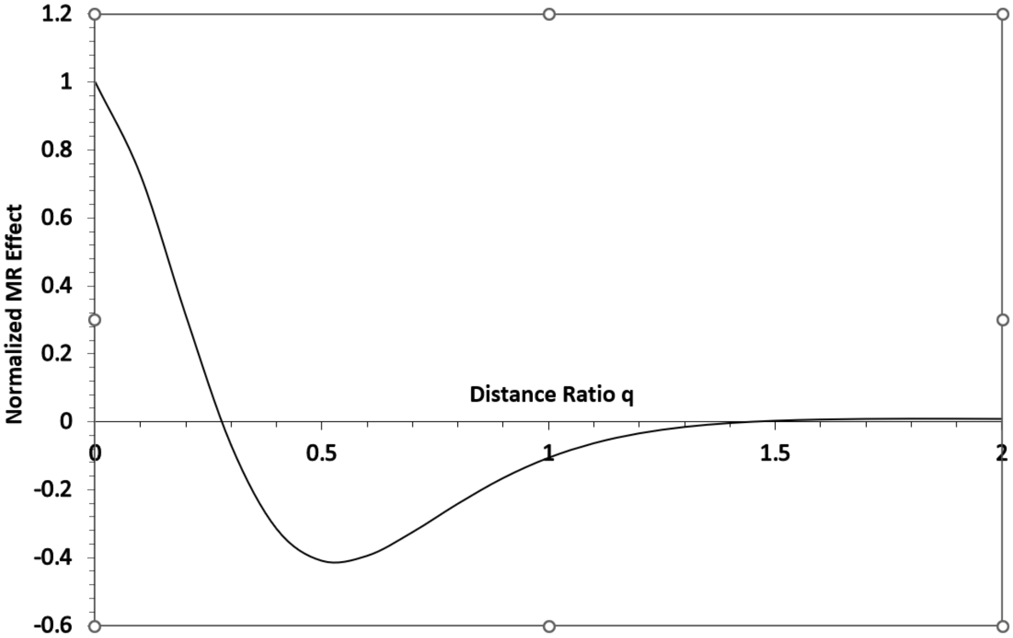

Figure 4.7 Normalized MR effect vs. distance ratio q.

Based on the results, the MR effect is largest when the particles are vertically aligned ($q = 0$). This suggests that straight chains provide the strongest MR effect, as the magnetic interactions are maximized in this configuration. As the particles move horizontally, simulating wavy chains or changes due to shear deformation, the MR effect changes. At $q = 0.28$, there is a critical transition point where the MR effect shifts from positive to negative, indicating a change from positive to negative MR effect.

As the distance ratio qqq increases further, the Negative MR effect decreases until reaches its peak at 0.53. When q is greater than 1.4, the MR effect approaches zero. In such cases, since this pair of particles does not significantly influence the MR effect, it suggests that if q is greater than 1.4 for all particles on separate chains, these chains will not influence each other's MR effect. This finding provides an important guideline for future simulations of chain structures. When considering a single isolated chain, the RVE size should be adjusted based on this result to avoid any interference from neighboring chains, which ensures that the MR effect observed is solely due to the chain being studied.

4.5 Conclusions

Chapter 4 provided a comprehensive examination of various simulation methods for MREs under quasi-static conditions, focusing on both 2D and 3D models to determine their efficacy in depicting accurate material behavior. Initial sanity checks validated the homogenization processes and ensured the integrity of the RVE setups. Detailed comparisons between the Magnetic Body Force Method and Magnetic Potential Energy Method were conducted, highlighting their respective capabilities and limitations in capturing the nuanced interactions between mechanical and magnetic forces. This analysis also explored the impact of particle arrangements and chain structures on the MR effect, revealing significant insights into how microstructural variations influence the overall performance of MREs.

Chapter 5 Viscoelasticity Analysis of Magnetorheological Elastomers (MREs)

5.1 Introduction

In this chapter, we delve into the hysteresis behavior of MREs by incorporating a linear viscoelastic matrix into our simulations. Understanding the viscoelastic behavior is crucial for MRE applications, as it significantly influences the material's damping properties and energy dissipation capabilities. Hysteresis simulations provide insights into the dynamic response of MREs, particularly under cyclic loading conditions, which are common in practical applications such as vibration isolation, damping systems, and adaptive stiffness devices. Our focus in this chapter is on the interactions between particles and the matrix, and the resulting MR effect under the influence of a viscoelastic matrix. By examining these interactions, we aim to provide a comprehensive understanding of the factors that govern the hysteresis behavior in MREs and how they can be optimized for specific applications.

5.2 Linear Viscoelastic Model

The linear viscoelastic behavior is characterized by time-dependent stress-strain relationships, which are essential for capturing the material's response under cyclic loading. We employ the generalized Maxwell model in combination with the Prony series to represent the viscoelastic properties of the matrix in our finite element simulations. The generalized Maxwell model consists of a series of Maxwell elements, each composed of a spring and a dashpot in series as shown in Figure 5.1.

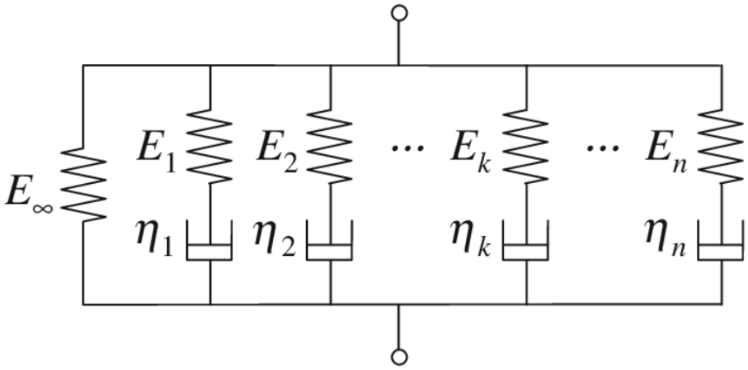

Figure 5.1 Sketch of the generalized Maxwell viscoelastic model.

The stress in each Maxwell element is governed by the Prony series, which describes the relaxation behavior of the viscoelastic material. The Prony series for the relaxation modulus is given by:

$$E(t) = E_\infty + \sum_{i=1}^{n} E_i \, exp(-\frac{t}{\tau_i}) \, , \tag{5-1}$$

where E_∞ is the long-term modulus, E_i are the moduli of the individual Prony series terms, τ_i are the corresponding relaxation times, and n is the number of terms in the series. In the context of FEM simulations, the generalized Maxwell model parameters E_i and τ_i are input into the material model to capture the time-dependent viscoelastic behavior of the matrix.

Since our focus is not to precisely capture the viscous behavior of a specific type of rubber based on experimental data, it is unnecessary to use an extensive number of terms in the Prony series. Instead, we aim to have a viscoelastic model that demonstrates suitable viscous behavior to effectively study the hysteresis effects in MREs. Therefore, we employ a three-term Prony series in conjunction with the generalized Maxwell model. The model parameters are shown in the following table, where $\mathbf{E_0}$ is the initial shear modulus:

Table 5.1 Parameters for the Prony series model.

$\mathbf{E_1/E_0}$	$\mathbf{E_2/E_0}$	$\mathbf{E_3/E_0}$	$\boldsymbol{\tau_1}$	$\boldsymbol{\tau_2}$	$\boldsymbol{\tau_3}$
0.233	0.233	0.233	0.1	0.01	0.001

After determining the viscoelastic model parameters, we proceed to discuss the FEM model setup and the homogenization process. The FEM model is subjected to a sinusoidal cyclic shear loading defined by the following equation:

$$\gamma(t) = \gamma_0 \, sin(2\pi f t) \, , \tag{5-2}$$

Where γ_0 is the amplitude of shear strain and f is the frequency. For each period of the cyclic loading, we use 80 time steps. These time steps are uniformly divided over the period to ensure more points are concentrated around the turning points of the sine wave, facilitating better convergence. To eliminate the transient effects that occur at the beginning of the simulation (at time t = 0), each simulation runs for at least three periods. To obtain the hysteresis curve, the stress and strain data at every node of the model are calculated and stored at each time step. The homogenization procedure is also performed at each time step. As previously discussed, we use the traction method for homogenization, which accounts for the time-dependent effects of the viscoelastic material.

5.3 Comparison of 2D and 3D Models Under Sinusoidal Loading

To further investigate the viscoelastic behavior of MREs, we constructed two models: one in 2D and the other in 3D. Both models feature a straight chain containing five particles, with the same particle radius, particle distance, and matrix size in the x-y plane. These models were subjected to a sinusoidal cyclic loading with an amplitude of 0.1 shear strain amplitude and a frequency of 10 Hz. No magnetic field was applied in this simulation. Periodic boundary conditions were applied to both models. However, due to the difference in geometry, the 2D model inherently has a higher volume fraction compared to the 3D model.

The sinusoidal cyclic loading is applied uniformly, with both models undergoing multiple loading cycles to reach a steady-state response and eliminate transient effects from the initial conditions. The stress and strain data at every node are calculated and stored at each time step, and the homogenization procedure is performed to capture the overall material response accurately.

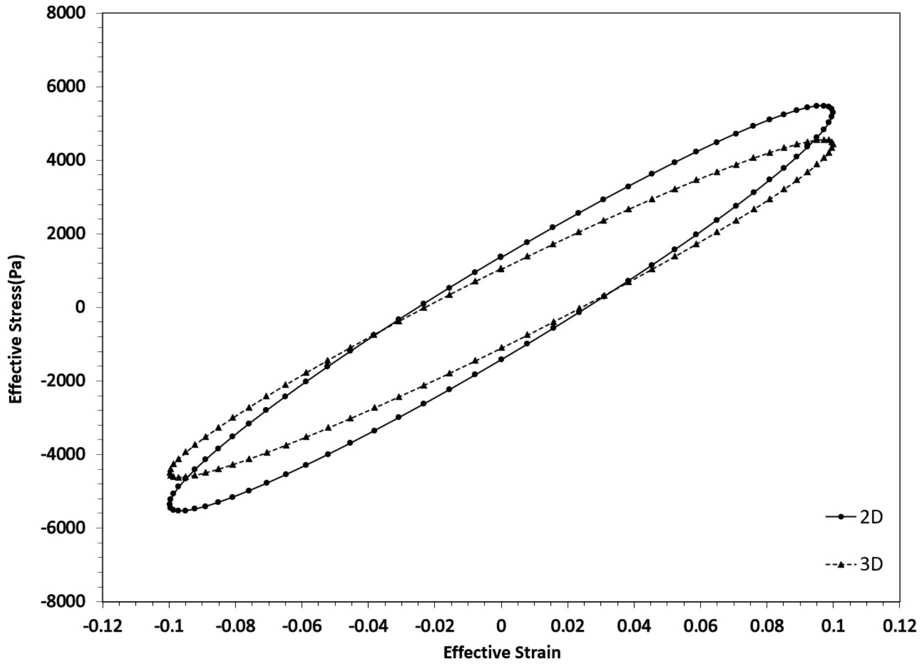

Figure 5.2 The comparison of 2D and 3D models.

The results, shown in the following Figure 5.2, highlight the differences in hysteresis behavior between the 2D and 3D models. By comparing these loops, we can observe the influence of dimensionality and volume fraction on the viscoelastic response. While the absolute values may differ due to the differences in volume fraction and geometry, the overall trends and viscous behavior are expected to be consistent between the 2D and 3D models. The findings support the use of 2D models in later simulations, providing a practical balance between computational efficiency and the ability to capture essential viscous behavior.

5.4 Dynamic Modulus

The dynamic modulus characterizes the material's response to oscillatory loading, providing insights into its stiffness and damping properties. The dynamic modulus E^* is a complex quantity comprising the storage modulus E' (elastic behavior) and the loss modulus E'' (viscous behavior):

$$E^*(\omega) = E'(\omega) + iE''(\omega)\,, \tag{5-3}$$

by applying a sinusoidal strain $\gamma(t) = \gamma_0\, sin(\,\omega t)$ to the model and measure the resulting stress $\sigma(t) = \sigma_0\, sin(\,\omega t + \delta)$, where δ is the phase angle, the storage modulus and loss modulus can be obtained using the following equation:

$$E'(\omega) = \frac{\sigma_0}{\gamma_0} cos(\,\delta)\,, \tag{5-4}$$

$$E''(\omega) = \frac{\sigma_0}{\gamma_0} sin(\,\delta)\,, \tag{5-5}$$

the magnitude of the dynamic modulus and the loss factor are given by:

$$|E^*(\omega)| = \sqrt{E'(\omega)^2 + E''(\omega)^2}\,, \tag{5-6}$$

$$tan(\,\delta) = \frac{E''(\omega)}{E'(\omega)}\,. \tag{5-7}$$

Another method to calculate the dynamic modulus involves using the stress-strain data from the hysteresis curve. When materials exhibit strong nonlinear behavior, their response to cyclic loading is not a perfect sine wave. This nonlinearity makes it challenging to accurately measure the energy dissipation using traditional methods that assume a sinusoidal response. To better capture the precise energy loss per cycle, we can utilize the area within the hysteresis loop of the stress-strain plot. The area enclosed by the hysteresis loop directly represents the energy dissipated by the material during each loading cycle. By analyzing this area, we can determine the loss modulus, which provides insight into the material's damping characteristics.

5.5 Analysis of Factors Influencing the Viscoelastic Behavior of MREs

As noted in the literature review, the behavior of MREs is influenced by various factors both during fabrication and under loading conditions. In this section, we focus on discussing how the viscoelastic behavior of MREs is affected by magnetic field dependence, strain amplitude, and frequency. These factors play crucial roles in determining the dynamic properties of MREs, making it essential to understand their individual and combined effects to optimize MRE performance for specific applications.

5.5.1 Magnetic Field Dependent Behavior

The application of magnetic fields to MREs influences their mechanical behavior by aligning the magnetic particles within the matrix, thereby affecting the overall stiffness and energy dissipation characteristics. The chain-like microstructure of an anisotropic MRE in a magnetic field is in a stable energy state. Altering this structure requires additional energy to overcome the magnetic forces between particles, which explains the increased storage modulus. However, the effect of the magnetic field on damping is less clear. To further investigate the influence of magnetic field strength on the hysteresis behavior of MREs and verify the capability of our current model, we apply varying magnetic flux densities and calculate the material response.

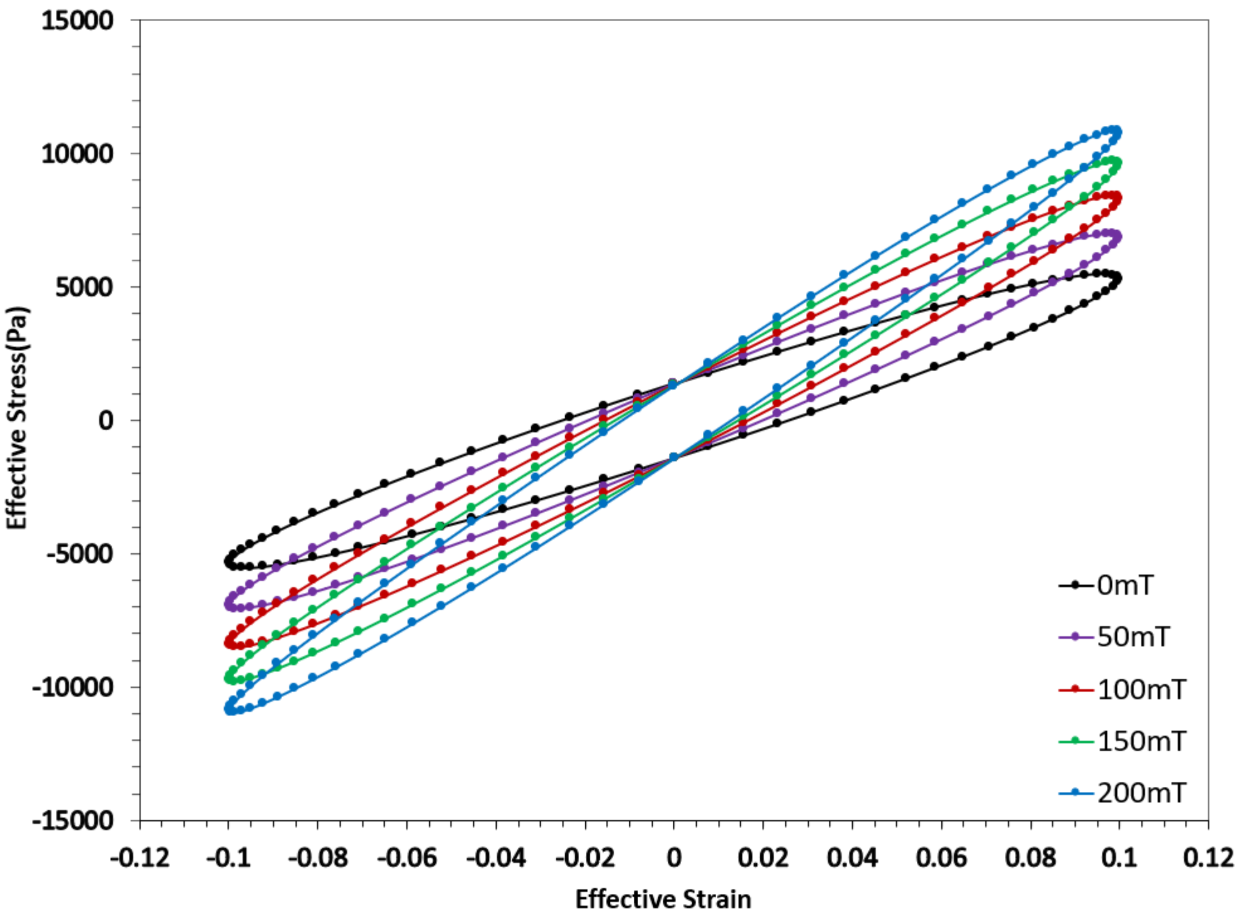

Figure 5.3 Hysteresis loop with magnetic flux densities B = 0 mT, 50 mT, 100 mT, 150 mT, and 200 mT.

Figure 5.3 presents the stress-strain hysteresis curves under various magnetic field strengths, and Figure 5.4 details the corresponding changes in storage modulus, loss modulus, and loss tangent as the magnetic field strength varies. The results depicted in Figure 5.3 align closely with experimental observations at lower magnetic flux densities, but significant discrepancies emerge as the magnetic field strength increases. Notably, the simulation shows that hysteresis curves for different magnetic flux densities converge at a single point when the strain is zero. This contrasts with experimental findings where larger magnetic flux densities cause the hysteresis curves at zero strain to broaden, increasing the area enclosed by these curves. This variance could be attributed to the model's simplification that, at zero shear strain, the magnetic force in the x-direction is consistently zero for all particles within the RVE. This assumption overlooks the complexities of particle interactions under varying magnetic fields, leading to a failure in capturing the shape changes of the hysteresis curves observed experimentally, suggesting a need for model enhancement to account for these dynamics.

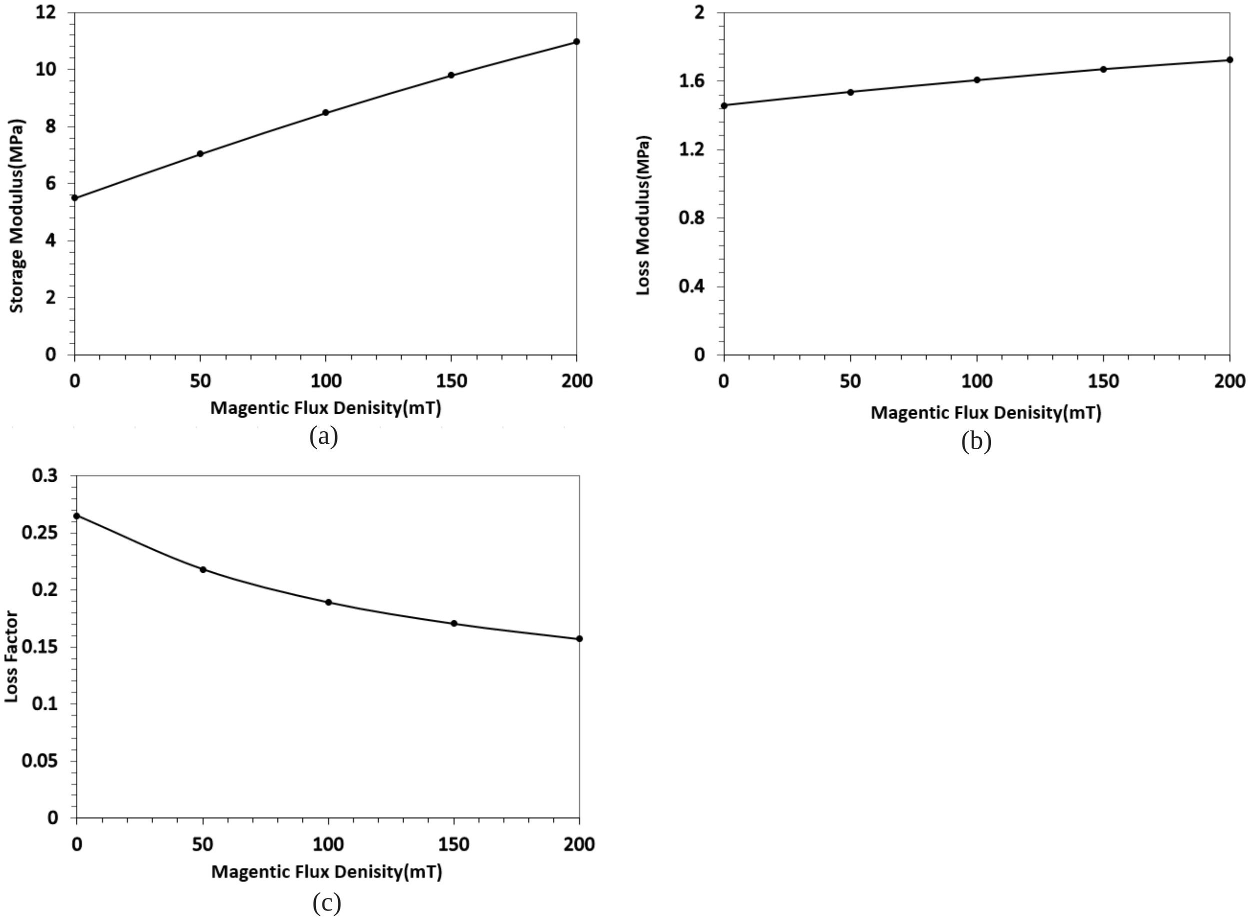

(a)

(b)

(c)

Figure 5.4 Dynamic modulus for different magnetic flux densities: (a) storage modulus, (b) loss modulus, (c) loss factor.

According to Figure 5.4, the storage modulus shows a linear increase with the magnetic flux density, aligning with expectations and corroborating previous experimental results. This trend indicates that the material's stiffness enhances as the magnetic field strength increases, likely due to improved alignment and interaction among the magnetic particles within the matrix. On the other hand, the loss factor decreases with increasing magnetic field strength. While this observation matches the findings of some studies, it contrasts with others that report an initial increase in the loss factor as the magnetic field strength rises, followed by a subsequent decrease.

To further evaluate the simulation capabilities of our current model, we selected two sets of experimental data from different studies focused on the magnetic dependency of MREs. These datasets were chosen because they were tested under varying conditions of frequency, magnetic field strength, and material properties, providing a robust basis for comparison. We constructed separate FEM models to align with the specific conditions described in each experiment. These simulations incorporated a matrix modeled as linear viscoelastic, applying a small affine deformation assumption for simplicity. To closely replicate the experimental setups, the RVE in each simulation was configured based on the specified particle distributions and volume fractions used in the studies. Material properties of the matrix, particularly Young's modulus, were carefully adjusted to match those used in the experimental conditions.

The first experimental dataset, described by Norouzi et al. [100], involved testing an MRE at a frequency of 0.1 Hz and a shear strain of 4%. The material composition consisted of 70% carbonyl iron particles, 20% silicone rubber, and 10% silicone oil. The magnetic fields tested were 0 mT and 272 mT. The second set of experiments, conducted by Dargahi et al. [101], tested an MRE at a higher frequency of 10 Hz and a shear strain of 5%. This material mix included 40% carbonyl iron particles, 40% silicone rubber, 10% tackifier, and 10% silicone thinner. The differences in stiffness and damping properties of the MREs used in these two sets of experiments are attributable to variations in material and volume fractions. Consequently, we developed two sets of model parameters for them, as presented in Table 5.2.

Table 5.2 Material properties of the FEM model for comparison with experimental data.

	$\mathbf{E_0}$(Mpa)	$\mathbf{E_1/E_0}$	$\mathbf{E_2/E_0}$	$\mathbf{E_3/E_0}$	$\boldsymbol{\tau_1}$	$\boldsymbol{\tau_2}$	$\boldsymbol{\tau_3}$
Set 1	0.213	0.176	0.176	0.176	1	10	100
Set 2	0.256	0.314	0.314	0.314	0.1	0.01	0.001

The results are plotted in Figure 5.5 and Figure 5.6. For both experiments, the hysteresis loops without a magnetic field were simulated accurately by our model. It managed to replicate most behaviors of the loops effectively, indicating that the basic dynamic properties of the MREs were well-captured. However, despite using a linear viscoelastic model, some minor nonlinear effects observed in the experimental results could not be fully simulated. This discrepancy suggests that while the model is robust in handling standard viscoelastic behavior, it may fall short in capturing more complex nonlinear interactions.

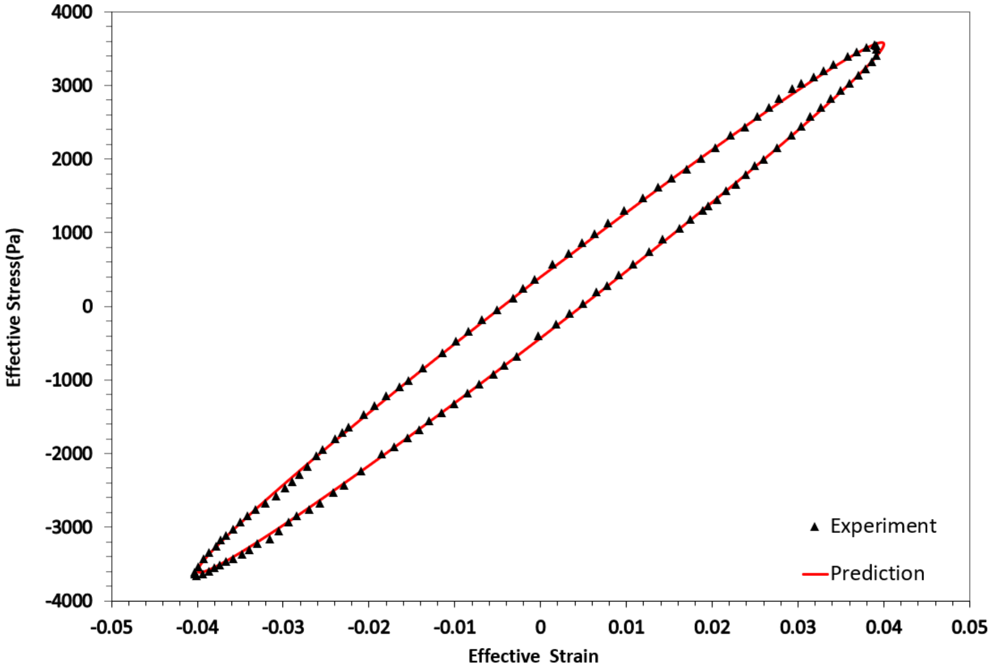

(a)

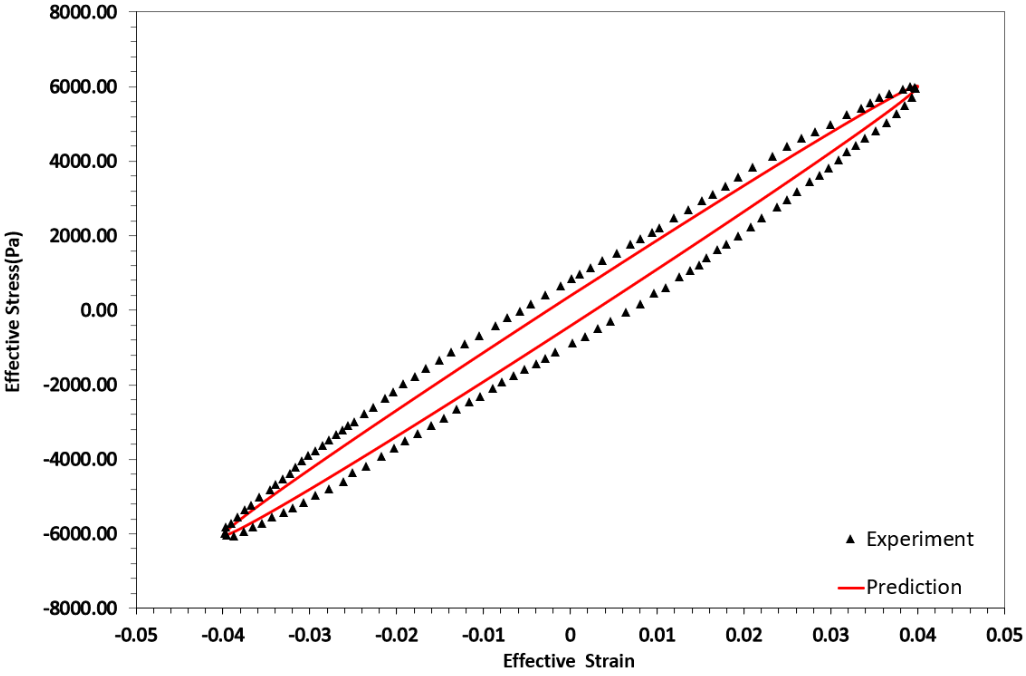

(b)

Figure 5.5 Comparison of the hysteresis loop in Norouzi’s experiment with simulation results: (a) B = 0 mT, (b) B = 272mT.

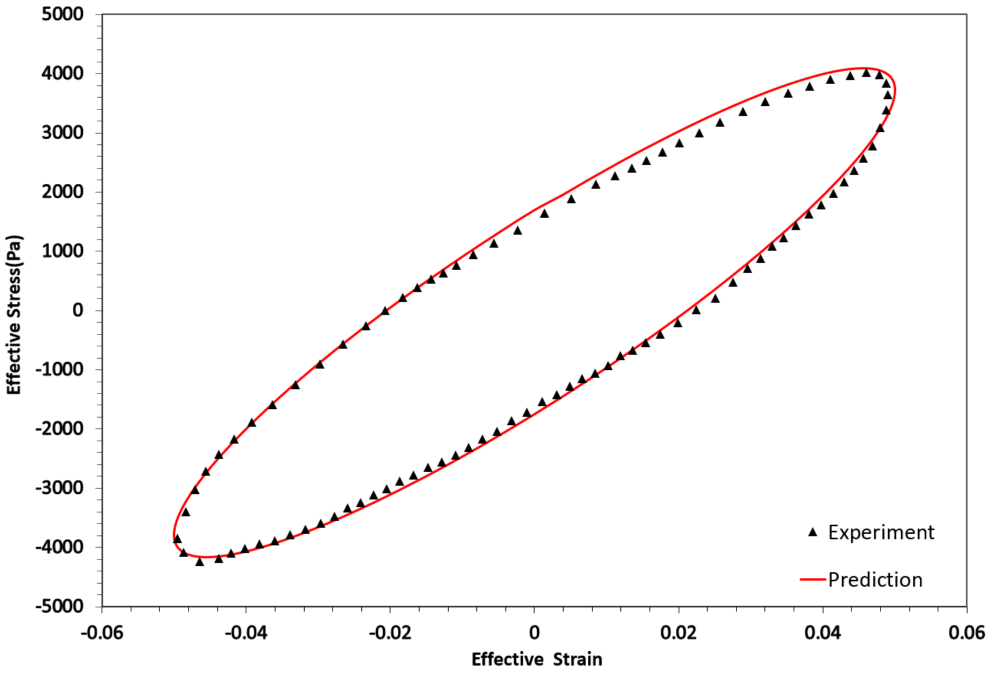

(a)

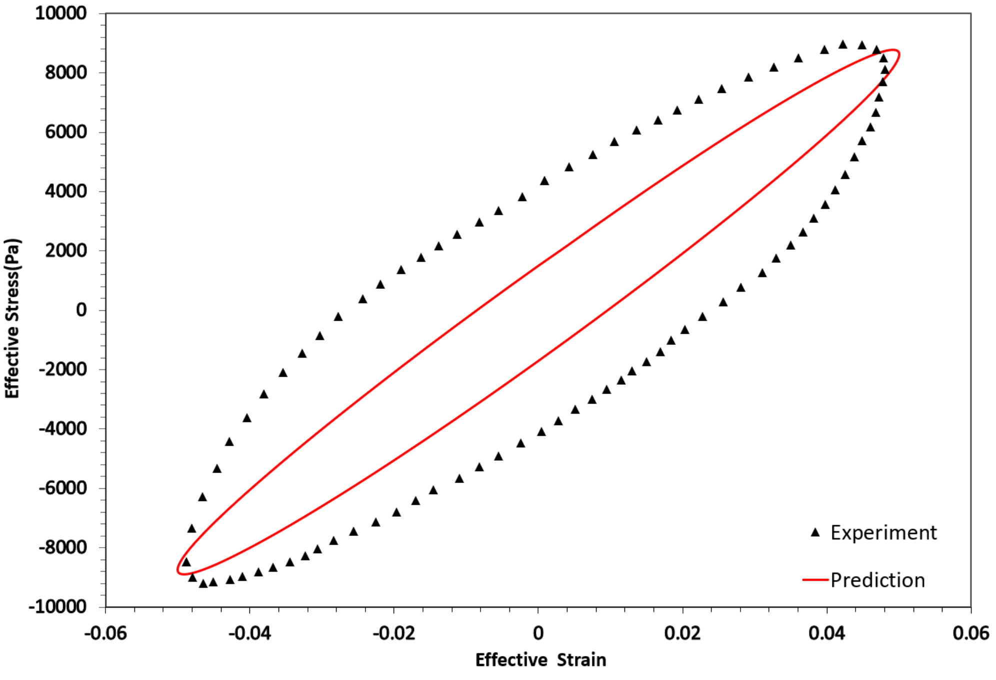

(b)

Figure 5.6 Comparison of the hysteresis loop in Dargahi's experiment with simulation results: (a) B = 0 mT, (b) B = 150 mT.

For both experiments, the hysteresis loops without a magnetic field were simulated accurately by our model. It managed to replicate most behaviors of the loops effectively, indicating that the basic dynamic properties of the MREs were well-captured. However, despite using a linear viscoelastic model, some minor nonlinear effects observed in the experimental results could not be fully simulated. This discrepancy suggests that while the model is robust in handling standard viscoelastic behavior, it may fall short in capturing more complex nonlinear interactions.

When a magnetic field was applied, our model successfully captured the MR effect associated with changes in the storage modulus. However, significant differences were noted in the area enclosed by the hysteresis loops. Our simulated loops had a smaller area compared to those in the experimental results. This difference indicates that our model has a reduced energy dissipation capability, which is primarily associated with the loss modulus and loss factor. Additionally, the application of the magnetic field altered the shape of the curves at the extremes of the loops, demonstrating stress-stiffening behavior that our linear viscoelastic model, forming elliptical-shaped loops, failed to replicate.

These findings lead us to conclude that although our model effectively predicts the hysteresis curves without magnetic fields and accurately captures the MR effect, it does not adequately predict changes in damping due to the magnetic field. The observed discrepancies, particularly in energy dissipation and stress-stiffening behavior under magnetic influence, highlight the need for a more sophisticated modeling approach. In subsequent chapters, we will explore the development of a new model that incorporates these nonlinear behaviors and better accounts for the dynamic changes induced by magnetic fields.

5.5.2 Strain Dependent Behavior

Strain amplitude, which refers to the maximum extent of deformation an MRE undergoes during cyclic loading, is a crucial factor that influences these smart materials' mechanical properties and energy dissipation characteristics. By systematically adjusting the strain amplitude in our simulations, we aim to uncover the underlying mechanics that dictate how MREs respond under varying operational stresses.

To investigate the influence of strain amplitude on the hysteresis behavior of MREs, we first conducted the hysteresis curves without the magnetic field for different shear strain amplitudes: 2.5%, 5%, 10%, and 20% using the FEM model, and compared with Dargahi's experiment as shown in Figure 5.6. In our examination of the hysteresis behavior of MREs at a zero magnetic field, both the experimental and simulated models initially exhibit similar responses under small strain amplitudes. However, significant discrepancies between the experimental results and simulation predictions become apparent as the strain amplitude increases. The experimental data reveal a notable decrease in the slope of the hysteresis loops with increasing strain amplitude. This trend indicates a reduction in the storage modulus of the MREs, which decreases substantially as the strain amplitude increases. This behavior suggests that the material's ability to store energy diminishes under more significant deformations, reflecting a nonlinear viscoelastic response. Notably, the shape of the hysteresis loops evolves from nearly elliptical at low strain amplitudes to distinctly non-elliptical under higher strain conditions. This transformation underscores the MRE's nonlinear characteristics, particularly under high strain amplitudes, where the viscoelastic properties become more pronounced.

Contrary to the nuanced behavior captured in the experimental data, our simulation models, which are based on linear viscoelastic assumptions, did not show any variation in the slope of the hysteresis curves across different strain amplitudes. The simulated curves maintained a uniform elliptical shape regardless of the amplitude, indicating a consistent predicted storage modulus even at higher strains. This discrepancy highlights the limitations of the linear viscoelastic model employed in our simulations, which fails to account for the material's nonlinear response as observed experimentally.

The inability of our current simulation model to replicate the nonlinear viscoelastic behavior observed in experiments, especially at higher strain amplitudes, points to a critical gap in our modeling approach. The linear viscoelastic model's assumption leads to predictions of elliptical hysteresis loops, which significantly diverge from the non-elliptical shapes seen under actual material testing. This discrepancy suggests that the model's assumptions are overly simplistic and do not capture MREs' complex interactions and mechanical responses under varied loading conditions. To address these discrepancies and improve the accuracy of our predictions, it is imperative to integrate nonlinear viscoelastic modeling approaches into our simulations.

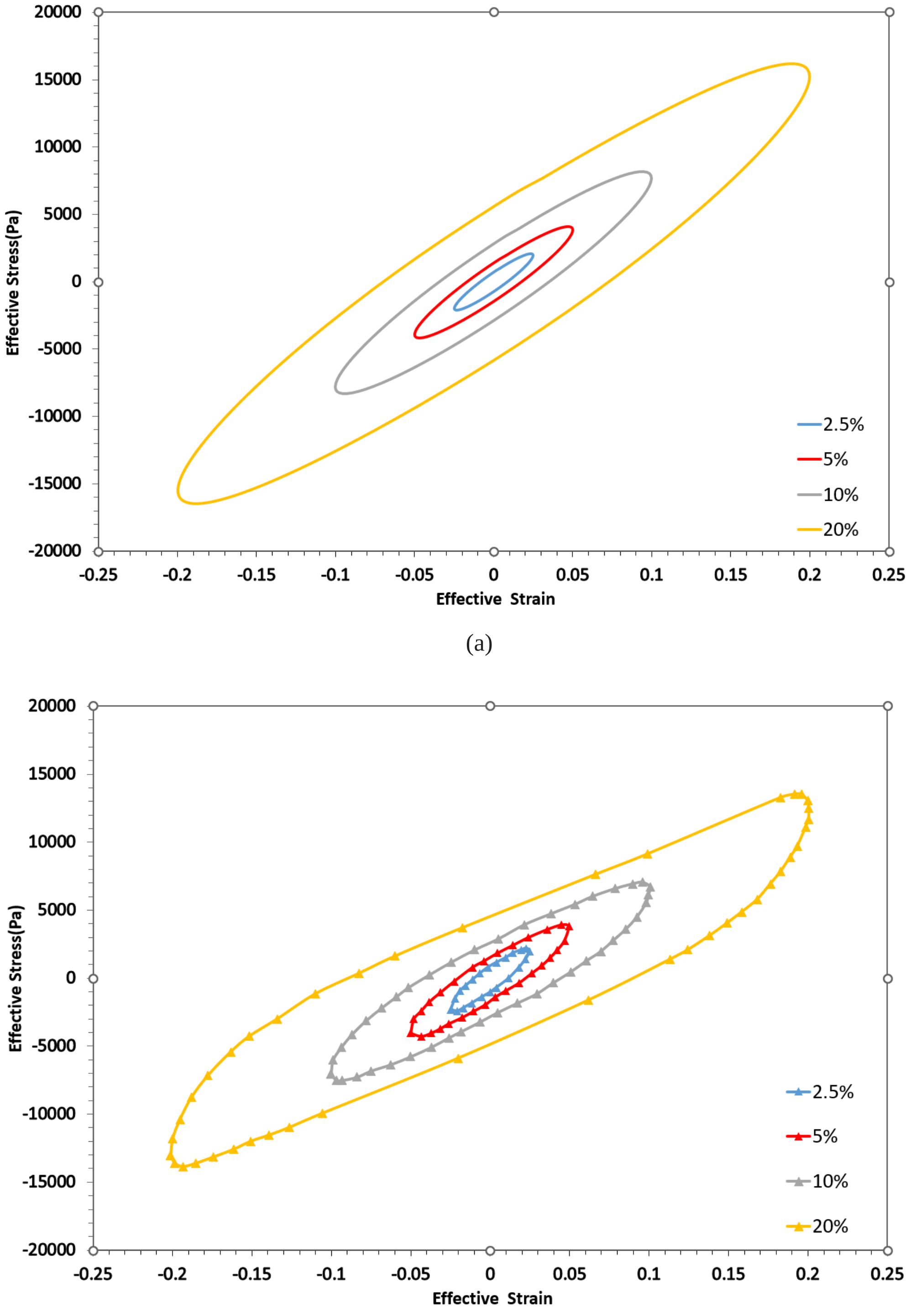

(a)

(b)

Figure 5.7 Hysteresis loop subjected to different strain amplitudes at B = 0 mT: (a) model prediction, (b) Dargahi’s experiment.

5.5.3 Frequency Dependent Behavior

Frequency dependence in MREs primarily manifests through changes in their viscoelastic properties under different loading rates, which can alter the material's response under cyclic loading, affecting the overall energy dissipation and storage capabilities. The matrix's properties, such as variable stiffness and damping, are highly responsive to changes in frequency, leading to different hysteresis behaviors under varied operational conditions. However, the magnetic particles and their interactions within the matrix are relatively invariant with respect to the frequency of the external stimuli. The core of our research is based on the premise that the magnetic effects—induced by the field-aligned interactions of particles—are critical to the functionality of MREs and do not strongly depend on the frequency.

Given the focus on particle-matrix interactions, we assume that any influence of frequency on the hysteresis behavior of MREs primarily affects the matrix, while the interactions between the particles and the matrix remain consistent across the frequency spectrum. This approach simplifies the complexity involved in dissecting the independent effects of frequency on the viscoelastic matrix from the magneto-mechanical interactions that are central to our study.

While this focused approach limits the scope of frequency investigation, it sharpens our analysis of the magnetic interaction dynamics, providing targeted insights that are vital for optimizing the design and application of MREs in various technological fields. Future studies could expand on this foundational work by integrating a comprehensive examination of frequency effects, especially to assess scenarios where the matrix properties significantly influence the performance outcomes in dynamic environments.

5.6 Conclusions

In this chapter, we delve into the significant differences observed between the experimental results and the predictions from our current simulation model concerning the hysteresis behavior of magnetorheological elastomers under various conditions. We explore the underlying causes of these discrepancies and propose strategies to enhance the accuracy of our modeling approach. Experimental results indicate that with an increase in strain amplitude, the storage modulus decreases, accompanied by a change in the curve shape to a more nonlinear and strain-softening behavior at both ends of the hysteresis loops. This decrease in storage modulus is largely attributed to the Payne effect, where the presence of filler particles within the matrix contributes to a reduction in modulus with increasing strain amplitude. The change in curve shape is influenced by multiple factors, including the material properties and dynamic interactions between the matrix and the particles. Additionally, as the magnetic field strength increases, the experimental hysteresis loops become substantially larger, suggesting an enhancement in the damping properties of the MREs. This increase in damping is often linked not just to the viscoelastic behavior of the matrix but also to increased friction at the interface between the particles and the matrix, which intensifies as magnetic forces bring the particles closer together. To better replicate these behaviors in our simulations, we propose transitioning from a purely viscoelastic model to a visco-hyperelastic model that can capture the nonlinear behaviors observed under higher strain amplitudes.

Chapter 6 Modeling of Visco-hyperelastic Behavior of Magnetorheological Elastomers (MREs)

6.1 Introduction

In Chapter 6, we address critical issues identified in previous analyses concerning the simulation of hysteresis curves under varying strain amplitudes. The existing models have revealed certain limitations, particularly in accurately reflecting the nonlinear responses observed in experimental studies of MREs. To resolve these discrepancies and enhance the fidelity of our simulations, we have adopted a visco-hyperelastic modeling approach. This model effectively captures the complex interactions within the MRE matrix, accounting for factors such as the dynamic curve shapes, magnetic-mechanical coupling, and the Payne effect, which are critical for understanding the material's response under practical operational conditions.

6.2 Hyperelastic Model

Hyperelastic materials are characterized by their ability to undergo large elastic deformations reversibly. In the context of MREs, incorporating hyperelastic behavior is crucial as it allows the simulation to more accurately reflect the real-world mechanical properties of the matrix under large deformations. Hyperelastic models are particularly adept at handling the finite strain behaviors where traditional linear elastic models fail, making them invaluable for simulating the complex interactions within MREs. For our simulations, we adopt the three-parameter Mooney-Rivlin model combined with the general Maxwell viscoelastic model to form a comprehensive hyper-viscoelastic model. The three-parameter Mooney-Rivlin model is a phenomenological model that extends the capabilities of the Neo-Hookean model by adding an additional term to better accommodate the mechanical response at larger deformations. The model is defined by the following strain energy function W:

$$W = c_{10}\left(\overline{I_1} - 3\right) + c_{01}\left(\overline{I_2} - 3\right) + c_{11}(\overline{I_1} - 3)(\overline{I_2} - 3) + \frac{1}{d}(J - 1)^2 \,, \tag{6-1}$$

where c_{10} and c_{01} are material constants characterizing the deviatoric deformation of the material; $\overline{I_1}$ and $\overline{I_2}$ are the first and second invariant of the isochoric left or right Cauchy-Green deformation tensor; d is the material incompressibility parameter; J is the determinant of the elastic deformation gradient F.

The initial shear modulus μ is defined by:

$$\mu = 2(c_{10} + c_{01})\,, \tag{6-2}$$

$$K = \frac{2}{d}, \tag{6-3}$$

where K is the initial bulk modulus. To account for the time-dependent behavior of MREs, the Mooney-Rivlin hyperelastic model is coupled with the viscoelastic component based on the generalized Maxwell model we proposed in Chapter 5. The choice to combine the Mooney-Rivlin model with viscoelastic elements is driven by the need to accurately represent both the immediate and long-term behaviors of MREs under dynamic loading conditions. The choice of the Mooney-Rivlin model over simpler models like the Neo-Hookean model is motivated by its superior capability to handle complex loading conditions and provide a more realistic representation of the nonlinear stress-strain relationships. While more complex and highly nonlinear models exist, employing them may obscure the specific effects of matrix-particle interactions that are central to our study. By using a moderately complex model like Mooney-Rivlin, we strike a balance between accurately modeling the matrix properties and maintaining focus on the interactions between the matrix and embedded magnetic particles.

6.3 Strain Amplitude Dependent Behavior

After updating our simulation model to incorporate visco-hyperelastic properties of the matrix, we conducted a series of tests to compare its predictions with the experimental data from Dargahi's study. The results, presented in Figure 6.1, span strain amplitudes of 2.5%, 5%, 10%, and 20%. The integration of hyperelastic properties into our model has introduced a level of nonlinearity to the predicted hysteresis curves, enhancing the accuracy of our simulations. At strain amplitudes of 2.5% and 5%, our model shows a strong alignment with the experimental results, suggesting that the visco-hyperelastic model effectively captures the material behavior under mild deformation conditions.

However, as the strain amplitude increases to 10% and 20%, discrepancies between our model predictions and the experimental observations become more pronounced. Notably, the experimental hysteresis curves exhibit a less sharp slope at these higher strain levels, indicating a significant decrease in the storage modulus. This behavior, which is indicative of the material's nonlinear stress-strain response, is not as clearly replicated in our simulation. In our model, this decrease in storage modulus under higher strain amplitudes is not as apparent, suggesting that while the visco-hyperelastic model enhances our simulation's responsiveness to strain changes, it may still be insufficiently sensitive to the more extreme nonlinear behaviors exhibited by the MREs at higher deformations.

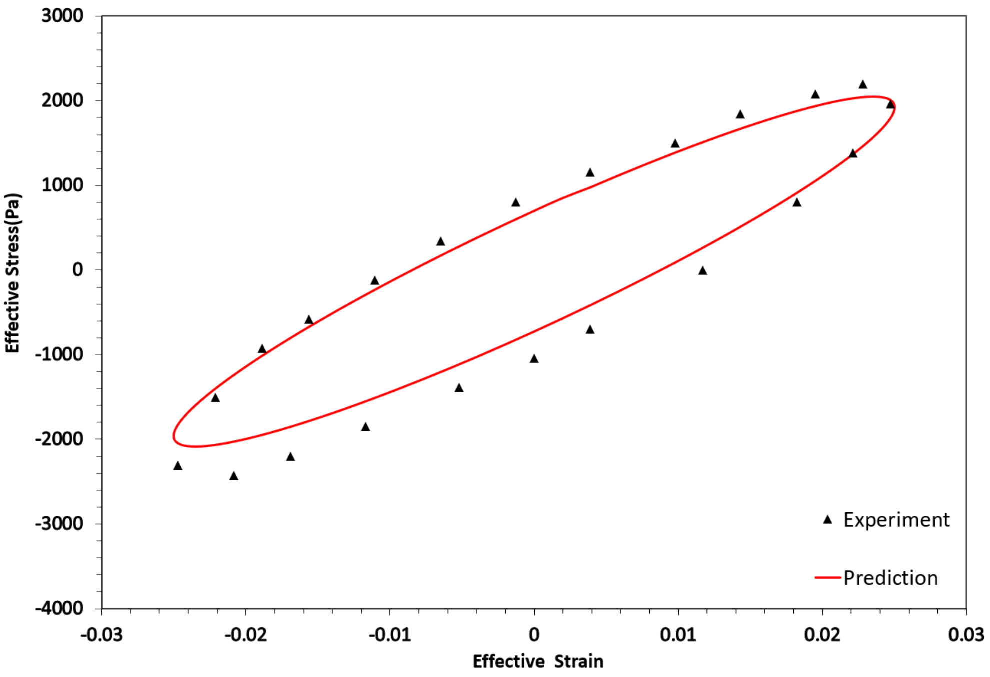

3000
2000
1000
0
-1000
-2000
-3000
-4000
Effective Stress(Pa)
-0.03
-0.02
-0.01
0
0.01
0.02
0.03
Effective Strain
▲ Experiment
Prediction

(a)

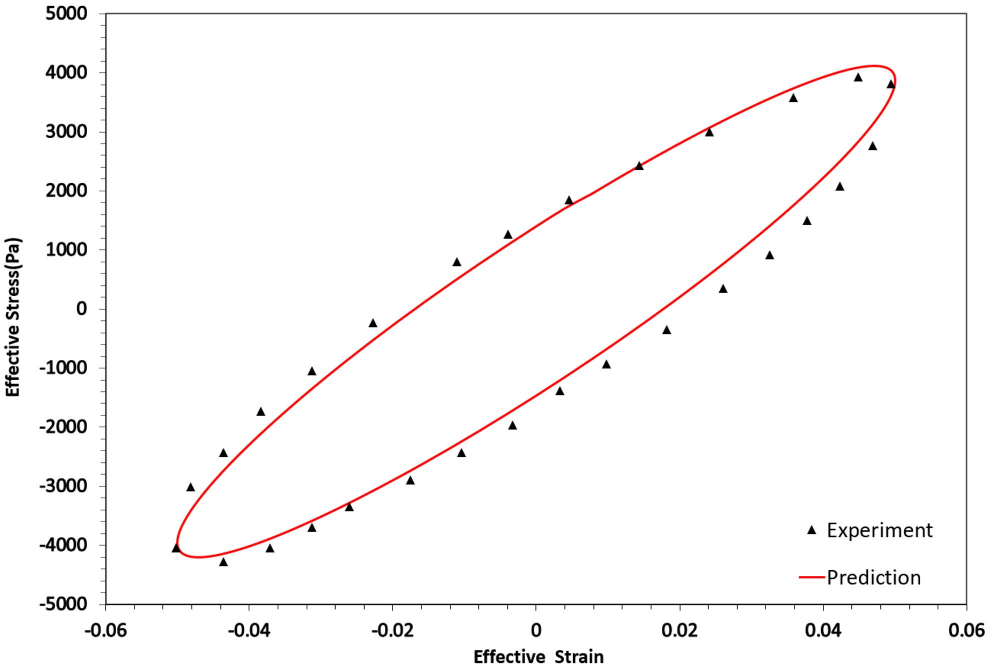

5000
4000
3000
2000
1000
0
-1000
-2000
-3000
-4000
-5000
Effective Stress(Pa)
-0.06
-0.04
-0.02
0
0.02
0.04
0.06
Effective Strain
▲ Experiment
Prediction

(b)

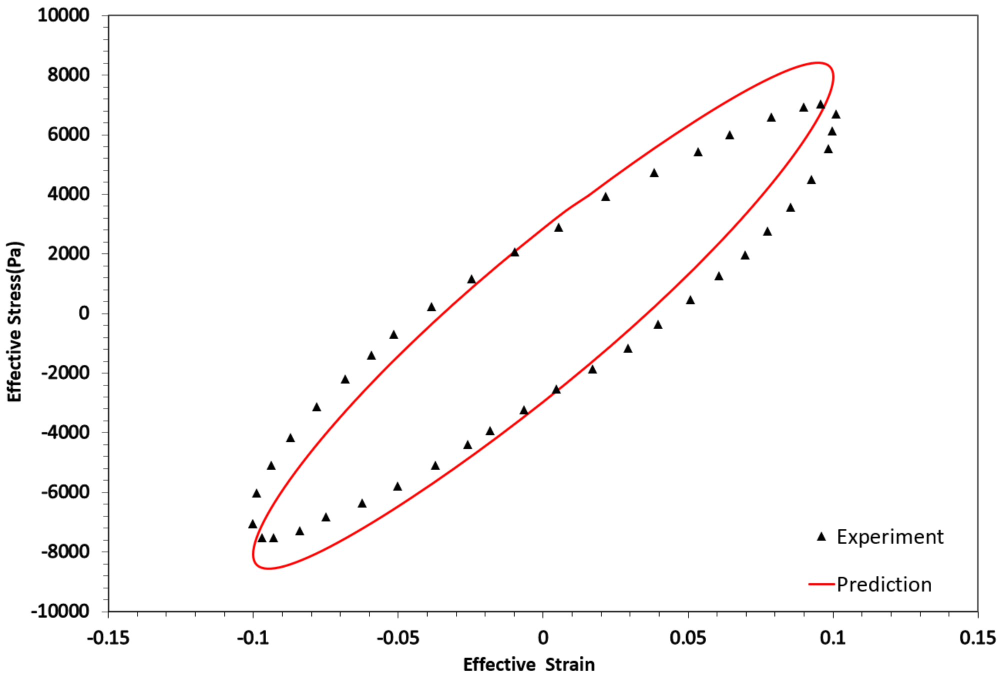

(c)

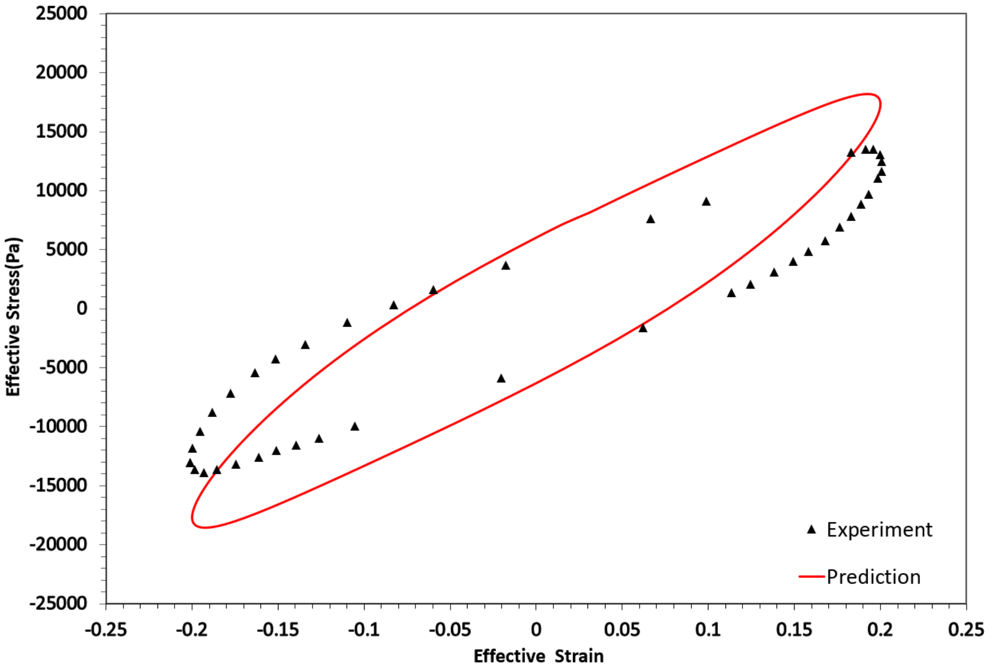

(d)

Figure 6.1 Comparison of hysteresis loops from Norouzi's experiment with model prediction at different strain amplitudes, B = 0 mT: (a) 2.5% strain, (b) 5% strain, (c) 10% strain, (d) 20% strain.

6.4 Modeling the Payne Effect

Numerous studies have delved into the Payne effect within MREs, providing various explanations and phenomenological models. These models generally attribute the effect to changes in the microstructure of composites, particularly the breakdown and subsequent reagglomeration of particle clusters during deformation [102-104]. However, in the context of this research, our focus narrows specifically to the impact of the Payne effect on the matrix only. For our purposes, the Payne effect is primarily observed as a degradation of the matrix's filler network under cyclic loading. This degradation leads to a pronounced decrease in the storage modulus as the strain amplitude increases. By isolating this aspect, we aim to examine the direct implications of the matrix's response to cyclic strain without the confounding influence of particle aggregation dynamics typically seen in more complex composite materials. To effectively model the Payne effect and its impact on the matrix, we use empirical models that directly relate the storage modulus (G') to the strain amplitude (γ) as shown below:

$$G^{'}(\gamma) = G_0^{'} - \frac{\Delta G^{'}}{1+(\frac{\gamma}{\gamma_c})^n}, \tag{6-3}$$

where $G'(\gamma)$ is the storage modulus at strain amplitude γ ; G_0' is the initial storage modulus; $\Delta G'$ is the maximum decrease in storage modulus due to the Payne effect; γ_c is a characteristic strain amplitude at which the modulus drops to half of $\Delta G'$; n is a fitting parameter that describes the sharpness of the modulus drop. With these adjustments, we conducted simulations at a 20% strain amplitude again to compare with experimental results. The empirical modeling of the Payne effect allowed for a much more accurate prediction. The revised simulations show that the storage modulus values now align closely with those observed experimentally, and the shape of the loading curves matches perfectly with the experimental data.

However, at the turning points of the unloading curves, a small discrepancy persists, exhibiting more pronounced strain-softening behavior than observed experimentally. This difference may stem from the limitations of the hyperelastic model used in our simulations. The parameters of the hyper model might not be optimally configured for capturing highly nonlinear behaviors, suggesting that a more complex nonlinear model could be required. Additionally, other factors inherent to the matrix's behavior under high strain conditions could also be contributing to this observed discrepancy.

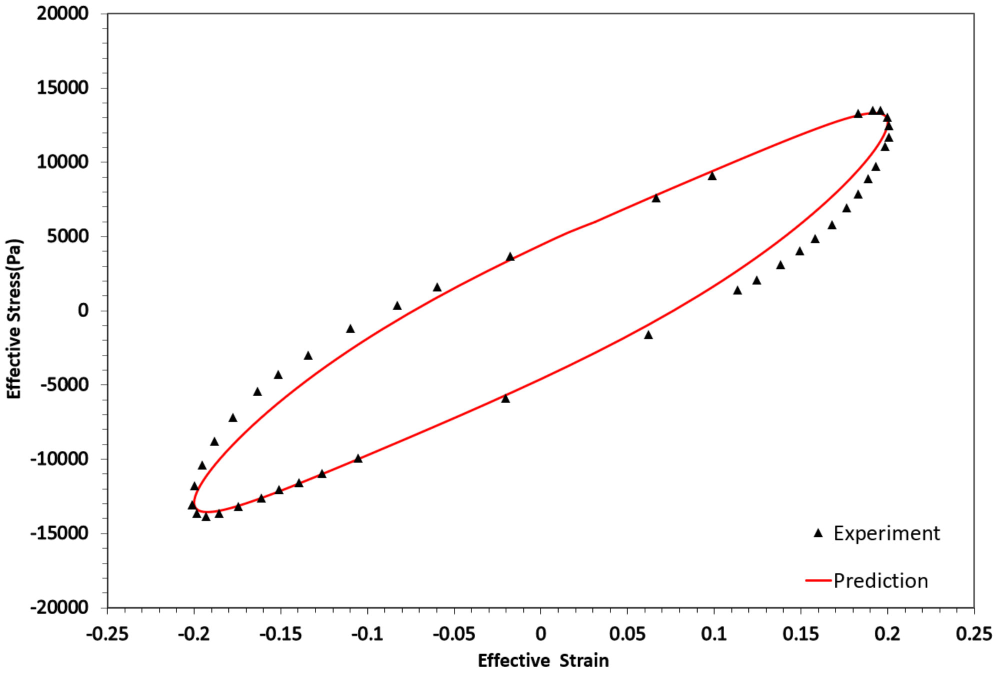

Figure 6.2 Comparison of the hysteresis loop from Norouzi’s experiment with model prediction at 20% strain amplitude considering the Payne effect.

While our modifications to incorporate the Payne effect within the matrix have significantly improved the fit of our model, particularly in terms of capturing the stiffness changes under varying strain amplitudes, it's important to acknowledge the simplifications made in this approach. In our model, we have isolated the Payne effect to the matrix component of MREs, effectively disregarding the potentially more significant Payne effects stemming from particle-matrix interactions. In real MRE systems, these interactions can introduce additional nonlinear behaviors that are more pronounced than those observed in the matrix alone.

This simplification may lead to a form of overfitting where our model, while accurately predicting certain behaviors, might not fully account for all the complexities involved in MRE dynamics. The interaction between the magnetic particles and the matrix likely contributes to a more complex Payne effect, which could significantly influence the material's overall properties. Ignoring this aspect might limit the applicability of our findings, particularly under conditions where particle-matrix dynamics play a critical role. To address this limitation and build a more comprehensive understanding of MRE behavior, future research should focus on developing new models that explicitly simulate the Payne effect arising from particle-matrix interactions.

6.5: Strain-Dependent Behavior of the Model with Magnetic Field

In this section, we explore the strain-dependent behavior of MREs when subjected to a magnetic field. Specifically, we examine how the model performs under a consistent magnetic field of 75 mT across varying strain amplitudes: 2.5%, 5%, 10%, and 20%. The strain-dependent curves obtained from these simulations are illustrated in Figure 6.3. For this series of tests, we deliberately chose not to include the Payne effect in order to simplify the variables and focus solely on the influence of the hyperelastic properties and the magnetic field.

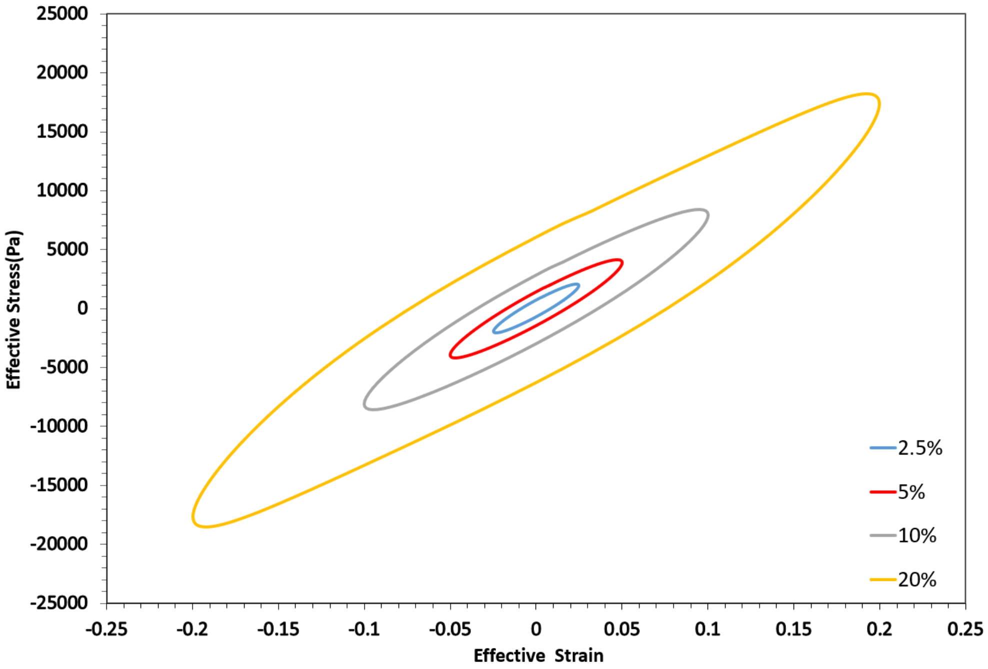

Figure 6.3 Model prediction of hysteresis loop at different strain amplitudes with B = 75 mT.

From the simulations, it is evident that the introduction of hyperelastic properties into the model allows us to capture some of the nonlinear changes that occur in response to both the applied strains and the magnetic field. These nonlinearities become more pronounced as the strain amplitude increases, reflecting the hyperelastic model's capacity to handle large deformations more realistically. Despite these improvements, the analysis of the loop area under different strain conditions reveals no significant changes. This observation suggests that while the hyperelastic properties of the model do contribute to capturing the nonlinear behavior of the MREs, they are not the primary drivers of increased damping observed in experimental setups when a magnetic field is applied. The lack of clear changes in the loop area indicates that other factors, likely related to the microstructural interactions between the magnetic particles and the matrix, play a more crucial role in influencing the damping characteristics.

6.6 Comparative Analysis of Full Coupling and Partial Coupling Models

In this section, we delve into additional nonlinearities that may arise not just from material properties or the Payne effect, but also from the complex interactions between magnetic forces and mechanical deformations. As previously discussed, under conditions of small magnetic fields and deformations, our models typically rely on the affine deformation assumption, which presupposes that particle positions remain unaffected by magnetic influences. However, this assumption does not hold under scenarios involving larger deformations and magnetic fields, where particle rearrangement during the cyclic loading process is significant and influences the material's behavior.

To better understand and simulate these complex interactions, we compare two different coupling methods: full coupling and partial coupling. We simulated the hysteresis curves at strain levels of 2.5%, 5%, 10%, and 20%, with a consistent magnetic field strength of 75 mT. The results of these simulations are illustrated in Figure 6.4.

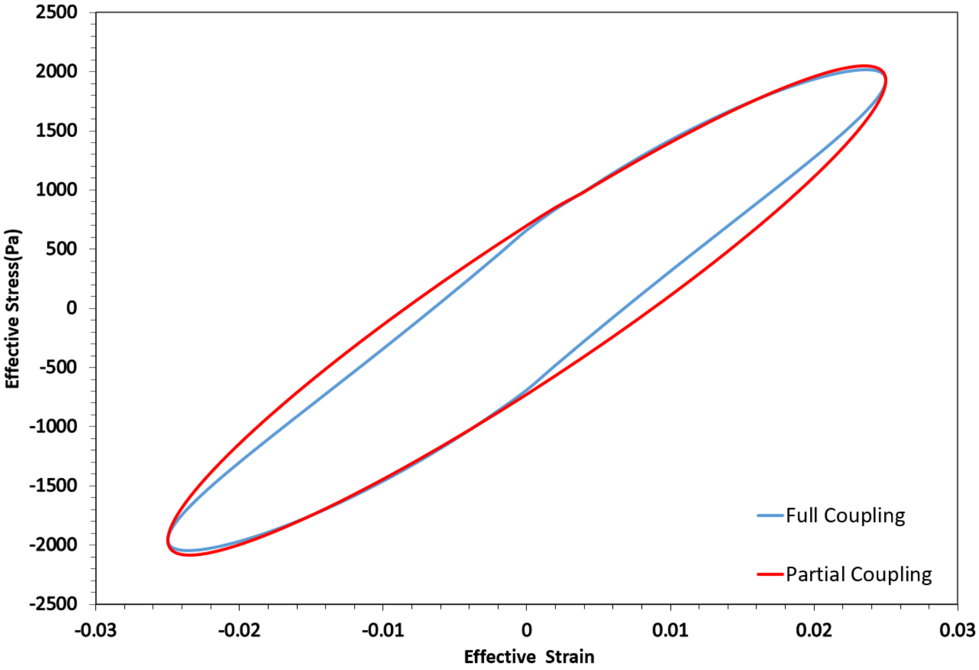
2500
2000
1500
1000
500
0
-500
-1000
-1500
-2000
-2500
Effective Stress(Pa)
-0.03
-0.02
-0.01
0
0.01
0.02
0.03
Effective Strain
Full Coupling
Partial Coupling

(a)

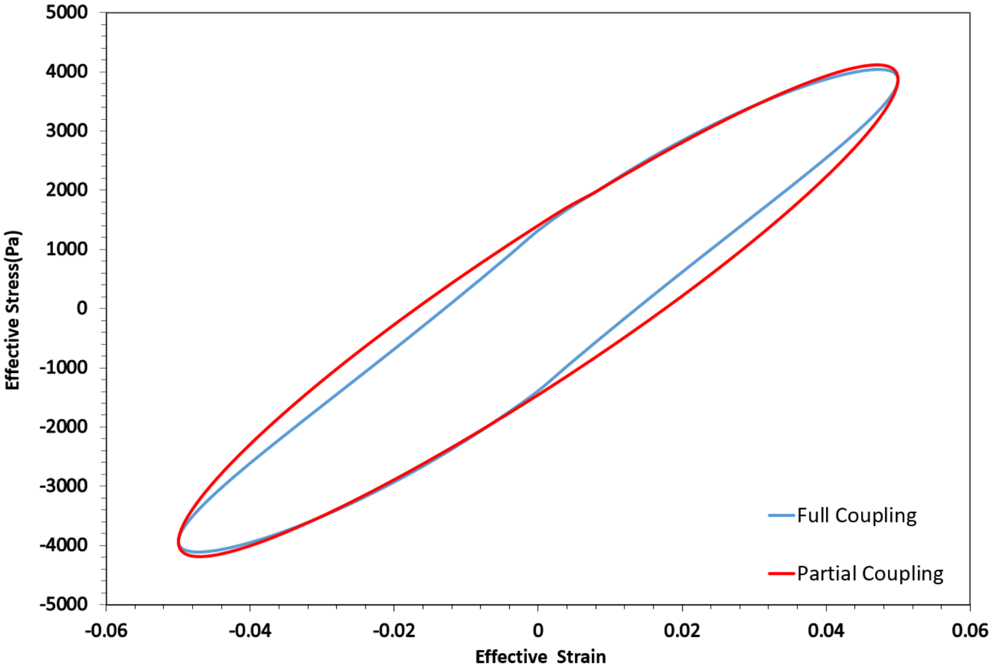
5000
4000
3000
2000
1000
0
-1000
-2000
-3000
-4000
-5000
Effective Stress(Pa)
-0.06
-0.04
-0.02
0
0.02
0.04
0.06
Effective Strain
Full Coupling
Partial Coupling

(b)

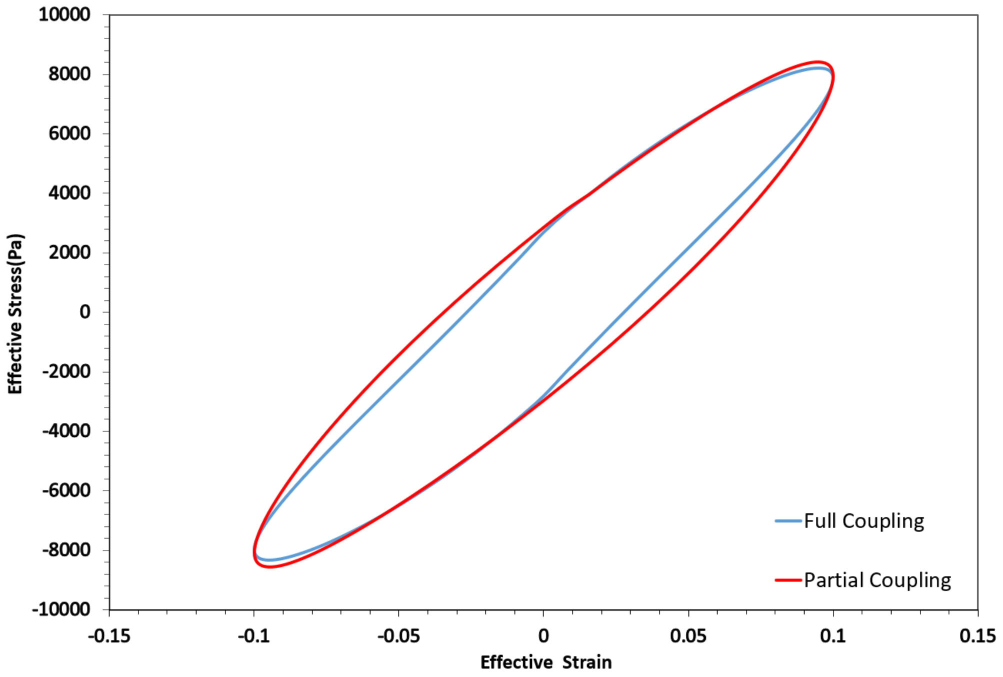

(c)

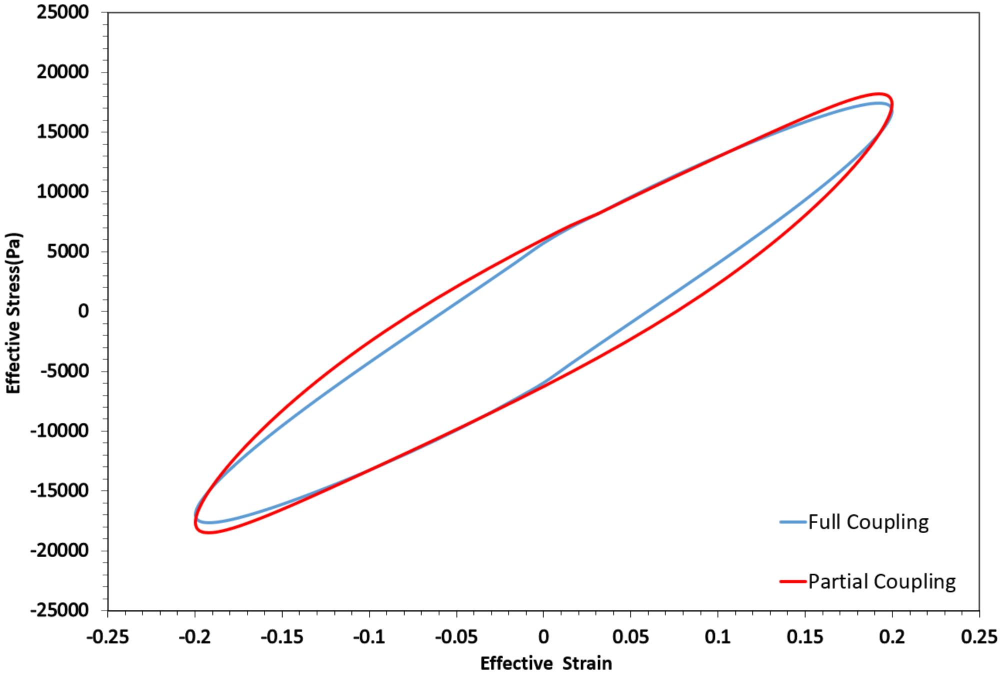

(d)

Figure 6.4 Comparison of hysteresis loops simulated using full coupling and partial coupling methods at different strain amplitudes, B = 75 mT: (a) 2.5%, (b) 5%, (c) 10%, (d) 20%.

While the general fit of the model remains satisfactory across both methods, a detailed examination of the hysteresis curves reveals key differences that underscore the impact of more complex modeling. With the full coupling approach, the hysteresis curves consistently exhibit smaller loop areas during the unloading phases across all tested strain levels. This characteristic points to a more pronounced nonlinearity in the material's response when both magnetic and mechanical effects are fully integrated. Notably, at higher strains (10% and 20%), the full coupling method shows lower peak values at the maximum strain points, indicating a subtle decrease in storage modulus. This behavior is particularly evident in the higher strain simulations and may be attributed to the interaction between magnetic forces and the hyperelastic properties of the matrix. The observed decrease in storage modulus and MR effect at higher strains could be explained by the dynamics of particle reallocation influenced by magnetic attraction. As the matrix becomes stiffer at larger strains, the responsiveness of particles to magnetic forces diminishes slightly, leading to larger inter-particle distances and consequently, reduced magnetic force. This phenomenon results in a minor decrease in the MR effect, which is primarily noticeable at higher strains.

6.7 Conclusions

In this chapter, we have systematically explored the hysteresis behavior of MREs under various conditions, focusing on the integration of visco-hyperelastic properties into our modeling framework. Our investigations revealed that while the visco-hyperelastic model provides a robust simulation of MRE behavior under mechanical loading alone, it falls short when magnetic fields are applied. The model accurately predicts the changes in storage modulus and the shape of hysteresis curves under non-magnetic conditions, demonstrating enhanced fidelity in capturing the nonlinear elastic responses of the matrix. However, the critical challenge remains in adequately simulating the increased damping effects—manifested as larger loop areas in hysteresis curves—when magnetic fields are introduced. This increase in damping, a key characteristic observed experimentally, is not sufficiently predicted by the current model. To address these shortcomings, there is a crucial need to develop our simulation approach further to include detailed modeling of the interface effects.

Chapter 7 Modeling of Interface Behaviors of Magnetorheological Elastomers (MREs)

7.1 Introduction

In this chapter, we explore the critical aspects of interface behavior in MREs , focusing particularly on debonding behavior, the dynamics of particle and matrix interaction during cyclic loading, and the influence of interface-related parameters on the material's performance. These elements are pivotal in determining the hysteresis curves and the inherent nonlinearity of MREs under operational conditions. We will examine the mechanisms of debonding at the particle-matrix interface, which can significantly impact the durability and functionality of MREs, especially under repeated mechanical stress. Additionally, the chapter will address how relative movements between the particles and the matrix during cyclic loading affect the material's mechanical integrity and damping capabilities.

7.2 Debonding Analysis with Cohesive Zone Models (CZM)

In our exploration of the interface behavior of MREs, understanding particle debonding under various loading conditions is crucial. While we anticipate minimal debonding during low shear amplitude loading, compressive and magnetic forces can significantly contribute to particle debonding. To analyze these phenomena, we utilize the Cohesive Zone Model (CZM), particularly focusing on its application within the context of MREs.

The interfacial separation in the CZM is defined by the displacement jump δ, which quantifies the difference in displacement between adjacent surfaces of the interface. This separation is considered in two primary orientations: normal separation δ_n, represented by the local direction n, and tangential δ_t , denoted by the local direction t. For the purposes of this study, we employ the Bilinear Cohesive Zone Model, which is articulated through three main variants. The Mode I dominated bilinear CZM posits that the separation of material interfaces is primarily influenced by the displacement jump perpendicular to the interface. The Mode II dominated bilinear CZM suggests that the separation is chiefly governed by the displacement jump parallel, or tangent, to the interface. Meanwhile, the mixed-mode bilinear cohesive zone material model considers both behaviors, accounting for interface separations influenced by displacement jumps that are both normal and tangent to the interface. The equations for these behaviors can be written as:

$$P = Ku(1 - d)\,, \tag{7-1}$$

$$d = \left(\frac{u-\bar{u}}{u}\right)\left(\frac{u^c}{u^c-\bar{u}}\right), \tag{7-2}$$

where P is the contact stress, K is the contact stiffness, u is the contact gap, $\bar{u}$ is the contact gap at the maximum contact stress, u^c is the contact gap at the completion of debonding and d is the debonding parameter.

To delve deeper into the dominant debonding mechanisms under compressive strain, we conducted finite element simulations applying the three modes of CZM. In these simulations, MRE models were subjected to a compression up to a strain of 0.25, using specific CZM elements tailored to each mode. After the initial compression, a very small shear strain was introduced to measure the effective shear modulus. The results, illustrated in Figure 7.1, show different behaviors between the CZM modes: Both Mode I and the Mixed Mode exhibited identical patterns, where the shear modulus experienced a sharp drop at a shear strain of 0.04 and complete debonding occurred at 0.05, indicating a sudden reduction in load-bearing capacity. Contrarily, Mode II begin to debond at the same initial point but displayed a more gradual decrease in shear modulus, extending to a strain of 0.14 with a smoother and less steep curve.

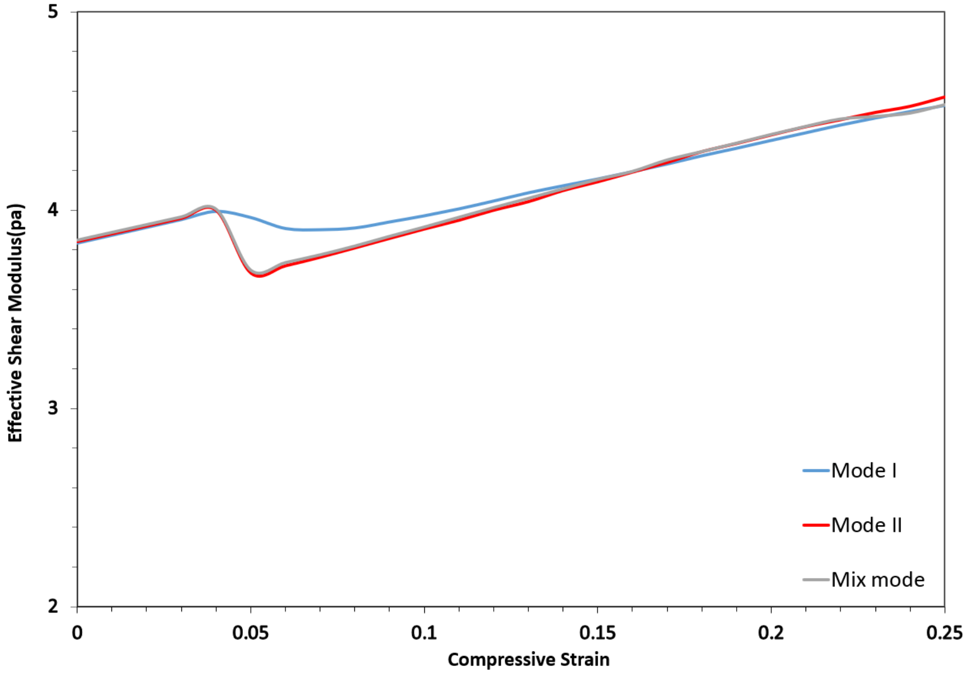

Figure 7.1 Analysis of Dominant CZM Modes in Debonding Behavior of MREs through Effective Shear Modulus Curves under Increasing Compressive Strain.

The distinct debonding behavior observed with Mode II suggests that tangential interactions, represented by Mode II, play a significant role in the debonding process under compressive and subsequent shear forces. Post-debonding behavior was similar across all modes, confirming uniform material properties once the interfaces had fully deboned. Given these findings, and to simplify further calculations, we will use Mode II CZM model in subsequent simulations.

Exploring the impact of interface stiffness on the debonding is crucial for optimizing their performance in dynamic environments. This section investigates how different levels of interface stiffness influence the debonding process under mechanical stress. We utilize four distinct CZMs, each designed to represent varying degrees of interface stiffness. These models range from relatively flexible to nearly rigid, mirroring conditions from loosely bonded particle interfaces to almost fully bonded scenarios. We assign the parameters with CZM1 establishing the base level of stiffness. Subsequent models increase in stiffness, with CZM2 having double, CZM3 four times, and CZM4 fifty times the stiffness of CZM1. CZM4 essentially simulates a nearly bonded interface, serving as a comparative benchmark for maximum interface rigidity. Each model is subjected to a predefined compression up to a strain of 0.25, followed by a minor shear strain to measure the effective shear modulus.

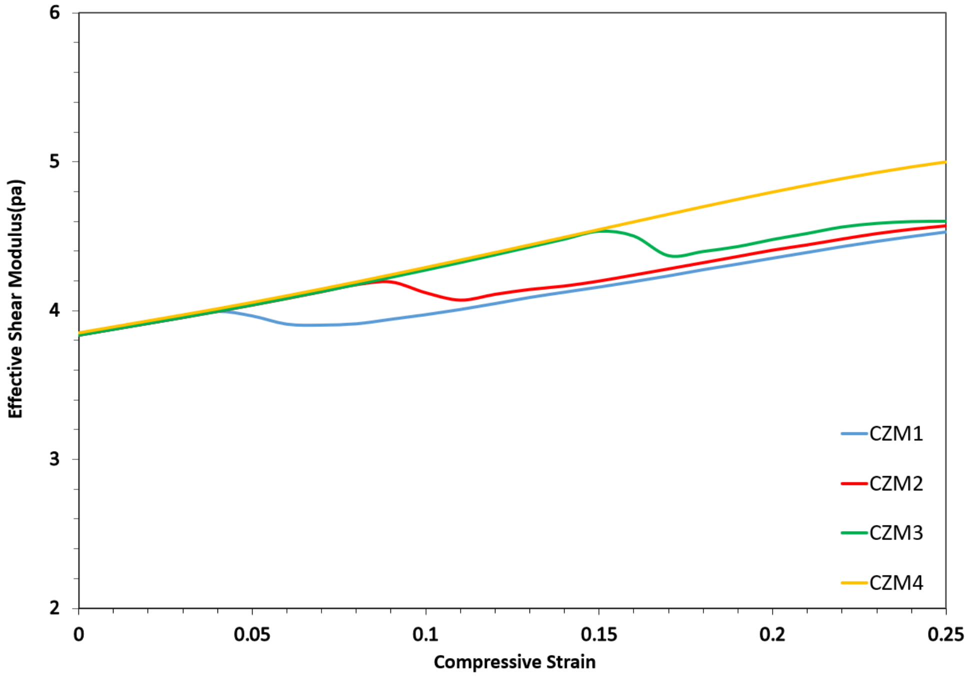

Figure 7.2 Debonding behavior with CZMs of different stiffness under compression.

The simulation results, illustrated through Figure 7.2, depict the debonding process across different stiffness settings. With increasing stiffness, there is a noticeable delay in the onset of debonding, corroborated by higher strain thresholds required to initiate interface failure. Moreover, stiffer interfaces exhibit a more rapid progression to complete debonding, characterized by sharper drops in shear modulus, indicating a sudden release of stored energy. Post-debonding analysis reveals that although the general pattern of the shear modulus curves remains consistent, the absolute values vary. Models with stiffer interfaces show higher residual shear modulus values post-debonding, suggesting that these interfaces retain more of their structural integrity and load-bearing capacity even after failure.

Besides compression, we have extended the analysis to include the effects of magnetically induced forces on debonding patterns, particularly focusing on straight chain models. Similarities between debonding behaviors under magnetic fields and those observed under compressive strains highlight the significant role of mechanical and magnetic forces at the particle interfaces. FEM simulations of a single particle model reveal typical particle interface statuses before and after debonding as shown in Figure 7.3. These visualizations show that debonding predominantly initiates at the left and right tips of the particle interface, where stress concentrations are most likely exacerbated by both compressive and magnetic forces. This pattern suggests a uniform stress distribution that progressively extends to the upper and lower regions of the particle, leading to full interface failure.

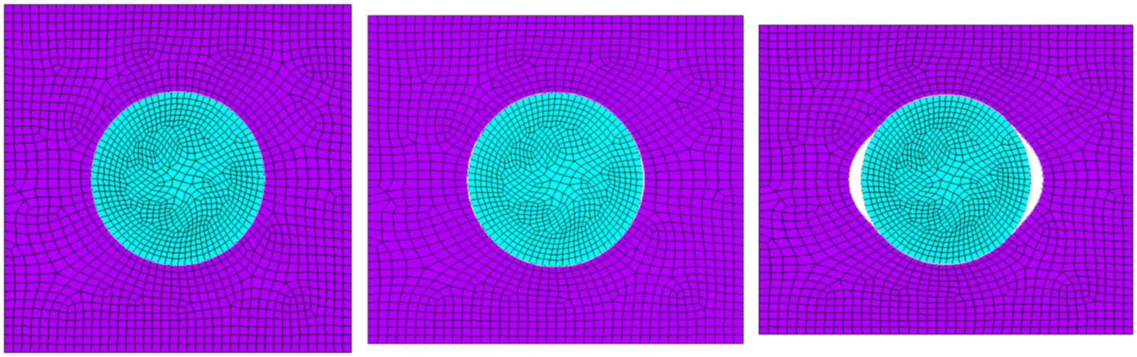

Figure 7.3 Illustration of interface debonding process using FEM model.

While the simulation results offer valuable preliminary insights, the real-world behavior of interfaces in MREs is considerably more complex. Several factors can influence and potentially exacerbate debonding, including initial material defects, the effects of temperature fluctuations, and creep under prolonged stresses. These elements can initiate debonding in areas that simulations predict to be stable and can cause debonding to propagate in unpredictable ways, complicating the prediction of material behavior under operational conditions. The use of the CZM in our simulations, while invaluable for detailed analysis of interface mechanics, brings significant computational challenges. The accuracy of CZM heavily depends on the quality of the mesh used in FEM simulations. Which results in a longer computation time. Furthermore, when CZM is integrated with other modeling approaches to capture different aspects of material behavior, it often complicates the FEM models, leading to difficulties in achieving convergence. Therefore, there's a need for building new models that account for these challenges.

7.3 Modeling of MREs with Various Initial Debonding States

Predicting the real interface conditions in MREs is inherently challenging due to the diverse material combinations and varying manufacturing conditions. To better simulate the range of possible interface behaviors and account for uncertainties, we have developed three distinct types of interface models that reflect different degrees of bonding between the particles and the matrix. The fully bonded (FB) model assumes an ideal bonded surface where the interface between the particle and matrix is very strong, representing conditions where no debonding occurs due to optimal adhesion achieved through superior material choice or manufacturing processes. Conversely, the fully debonded (FDB) or weakly bonded interface model considers a scenario where the particles and matrix have completely separated prior to the simulation, assuming interactions are purely frictional—a situation that might arise from poor processing or inherent material weaknesses. Additionally, we introduce two partially bonded (PB) interface models to capture more complex and realistic scenarios. The first of these models reflects debonding occurring only at the left and right sides of the particle, informed by stress concentration points identified in previous simulations using the CZM. The second partially bonded model incorporates initial defects, allowing debonding to potentially occur at any point around the particle, and is suitable for materials with known imperfections affecting interface integrity.

To effectively simulate the two debonding behaviors described, we employ a schematic model as illustrated in Figure 7.4. The model depicts a particle sectioned into four distinct regions through cuts along the top, bottom, left, and right sides. These divisions are designed to isolate sections of the particle interface, allowing for differential treatment of each segment. The perpendicular distances from the cut lines to the particle's center, denoted as a_t, a_b, a_l, and a_r, serve as crucial parameters in defining the interface conditions. Each region is equipped with contact elements that can be either bonded or debonded, with debonded regions incorporating interface friction to simulate physical interactions.

To manage the interface conditions, the parameters as a_t, a_b, a_l, and a_r are adjusted. For models simulating debonding solely on the left and right sides, a_t and a_b are set equal to the particle radius, effectively keeping the top and bottom regions bonded. Conversely, a_l, and a_r are adjusted to represent the debonding status along the sides of the particle. In the scenario where debonding is randomized, a total debonding ratio, d_r, is employed. This ratio is calculated as $d_r = cos(a_t) + cos(a_b) + cos(a_l) + cos(a_r)$, distributing the debonding status across each particle interface region based on this cumulative measure. This method allows for the simulation of varied debonding patterns, reflecting more complex, real-world conditions where debonding might not uniformly affect all sides of a particle. By controlling these parameters, we can finely tune the interface model to reflect different levels and patterns of debonding.

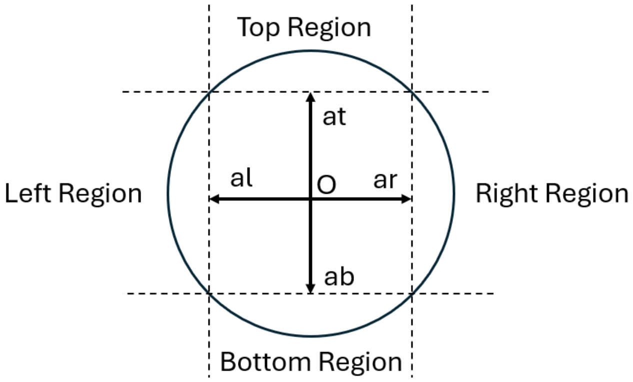

Figure 7.4 A sketch of the interface debonding status model with four regions.

We conducted detailed simulations to examine hysteresis loops under different interface conditions: fully bonded, weakly bonded, and partially bonded interfaces, specifically at the left and right sides with parameters $a_l = a_l = 0.5r$. Each model was subjected to a consistent testing protocol of a 5% shear strain amplitude at a frequency of 10Hz and an interface friction coefficient of 0.4. To investigate the effects of magnetic influences, these simulations were initially performed without a magnetic field and subsequently with a small magnetic field of B=10mT.

The fully bonded interface model demonstrated a robust hysteresis loop, indicative of high energy storage and dissipation capabilities. This suggests that strong bonding at the interface effectively transmits mechanical loads across the MRE, enhancing its functional properties under cyclic loading. In contrast, the weakly bonded interface exhibited a much thinner loop, reflecting a significant reduction in both the storage and loss modulus. The curve was notably more nonlinear, highlighting how complete loss of bonding can degrade the material's response to mechanical stresses. The partially bonded model showed a hysteresis loop that was slightly thinner and shorter than the fully bonded case but maintained a shape with reduced nonlinearity. This observation suggests that partial debonding, specifically at the sides of the particle, minimally impacts the overall mechanical behavior compared to complete debonding, preserving much of the material's inherent properties.

When a magnetic field of 10mT was introduced, the fully bonded model did not exhibit any significant change in damping behavior, typically evident at zero strain. However, the weakly bonded model displayed slight changes. The loop became more linear on the loading curve, possibly indicating that the friction behavior, which predominantly occurs at the top and bottom regions of the particle in fully bonded cases, is not a significant factor in our debonding setup where these regions remain fixed. This aligns with some experimental findings and supports the hypothesis that in debonding conditions where friction is absent, the magnetic field does not enhance damping as expected.

We also explored the effects of random initial defects on the interface through a series of simulations. These simulations employed varying debonding ratios and statuses to mimic the unpredictable nature of material defects. The results from these simulations were notably inconsistent, displaying a wide array of values for the hysteresis curves. This variability underscores the complex influence that random defects have on the mechanical behavior of MREs. Despite the unpredictability, the resultant curve values consistently fell within the range observed between fully and weakly bonded cases. This observation suggests that while the debonding status at different regions of the interface significantly impacts the overall response of the MREs, the extreme cases of fully bonded and weakly bonded provide boundaries for the possible behaviors. Given the high variability and the extensive computational resources required to accurately simulate each possible defect scenario, we have decided not to focus in detail on this aspect of the study. Instead, to achieve more consistent results and understand the maximum potential for damping behavior changes, we are opting to use the weakly bonded model in subsequent simulations.

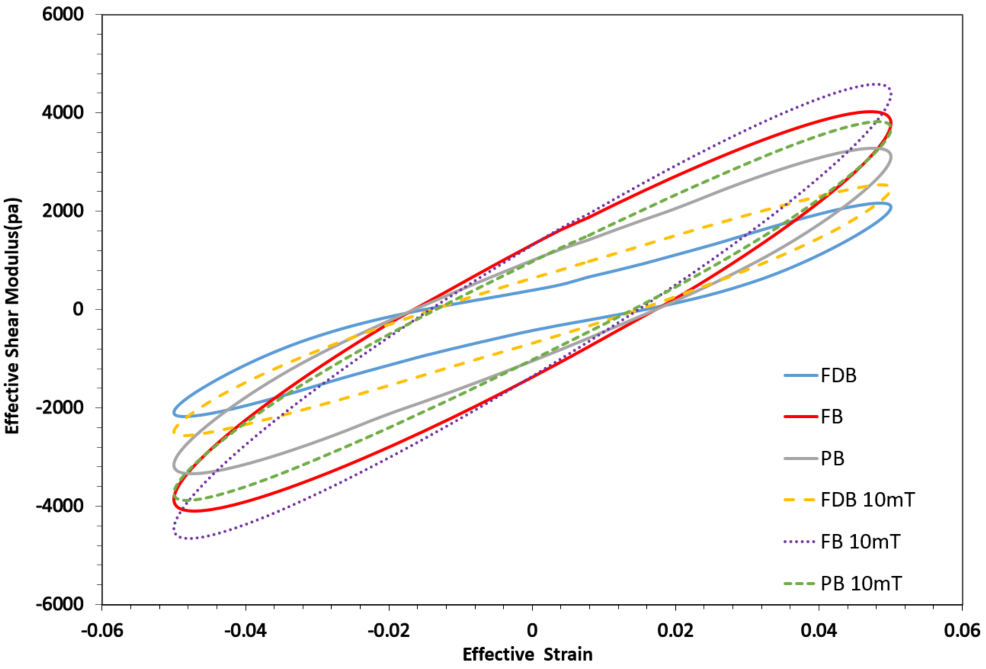

Figure 7.5 The influence of magnetic field on the hysteresis behavior of models with different debonding conditions.

7.4 Interface Analysis

Our prior simulations have revealed that interface friction significantly impacts the hysteresis curves, leading to unusual loss modulus characteristics and greater nonlinearities. To delve deeper into the origins of these phenomena, we are now focusing on how interface behaviors are influenced by magnetic fields and cyclic loading, particularly observing how magnetic forces affect particle alignment and interface status within a vertically oriented chain. Building on the foundational work of previous researchers who considered simple interface conditions [105,106], we aim to develop and integrate more detailed interface models into our simulations.

7.4.1 Modeling of Interface Condition Under Magnetic Field

For this detailed examination, we have constructed a model with five particles arranged in a straight chain, serving as an illustrative tool to demonstrate the interaction dynamics under magnetic influences without any applied shear strain. As depicted in the figure(, different particles within the chain exhibit varied interface statuses when subjected to a magnetic field. The outside particles, numbers 1 and 5, are attracted towards the center of the chain by the magnetic field, resulting in only one part of each particle—facing towards the center—remaining in contact with the matrix, a scenario we refer to as "Interface 1." The third and fifth particles experience a combination of magnetic attraction and mechanical compression from the chain, ensuring that both the top and bottom regions of these particles are in contact with the matrix, a condition labeled as "Interface 2." The middle particle, number 3, experiences no direct magnetic force due to its symmetrical position within the chain but the compressive forces exerted by its neighboring particles cause both of its vertical sides to touch the matrix, and we call it "Interface 3."

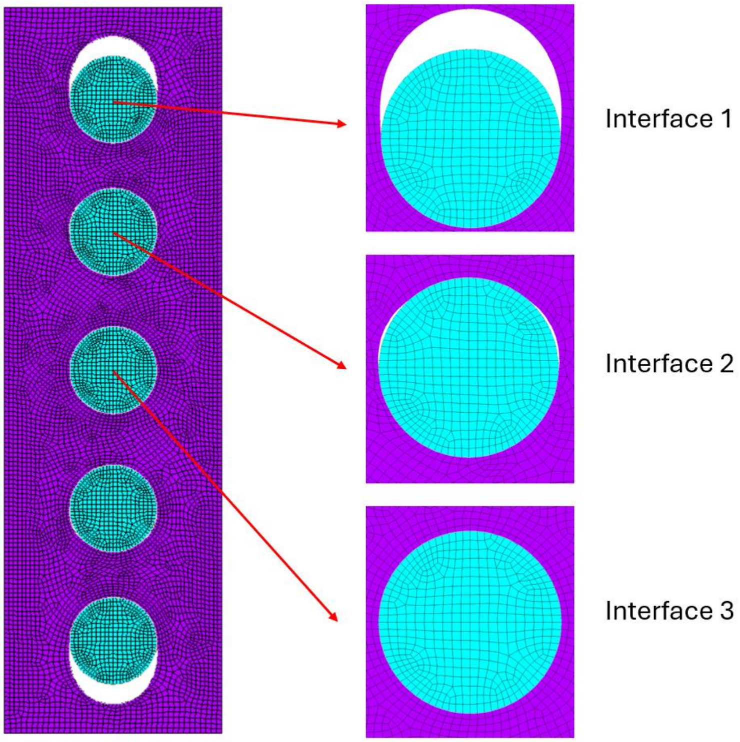

Figure 7.6 FE model illustration of different interface conditions within a chain under the magnetic field.

The potential for these interface conditions to change or transition between each other during the loading process depends on the strength of the magnetic field and the interface friction coefficient.

To systematically describe the evolving interface behavior under cyclic loading within MREs, we have identified a progression through several distinct stages:

1. **Initial Sliding Stage**: At low magnetic fields, most parts of the particle surface experience relative sliding due to cyclic loading. This initial stage is marked by substantial nonlinear energy dissipation as the particles are less constrained, allowing for significant movement at the interfaces, which increases the system's overall energy loss.

2. **Partial Bonding Stage**: As the magnetic field strength increases, the energy dissipation capability of the MRE also rises, albeit at a varying rate. When the magnetic field reaches a certain threshold, a portion of the particles becomes bonded to the matrix due to magnetic forces, effectively eliminating relative movement at that interface. The particles are then considered partially bonded. Energy loss during this stage primarily results from friction between the unbonded surfaces and the matrix. Despite further increases in magnetic field strength, the rate of energy dissipation begins to plateau, and the damping behavior becomes more linear.
3. **Increased Bonding Stage**: At higher magnetic field strengths, the chain length compresses due to the force exerted by the side particles in the chain, causing more than one region of the particles to bond with the matrix through increased friction. This stage resembles previously simulated conditions where particles with both top and bottom regions fixed exhibit partial bonding, resulting in a stable damping behavior. Further increases in magnetic field strength primarily enhance the storage modulus, with diminishing effects on damping properties due to reduced areas available for energy-dissipating interface slippage.

To verify our assumptions and gain a deeper understanding of the described stages, we constructed a model similar to that depicted in the earlier figure() to track the friction energy of each particle during the cyclic process. This measurement serves as an indicator of the energy dissipation capability and interface behavior within the system. To accurately measure the friction energy, we coupled each interface node with its closest matrix node, calculating both the tangential and vertical relative displacements and reaction forces at every timestep. The friction energy U at one node at the end of time step $n+1$can be estimated using the formula $U = F_n(d_{n+1} - d_n)$, where F_n is the tangential reaction force at timestep n, and d represents the tangential relative displacement at certain time steps. The total friction energy for one particle at a given time point is then calculated by summing the energy contributions from each node on that particle.

The results of this simulation are depicted in Figure 7.7. We considered three types of initial interface conditions—Interface 1 (a), Interface 2 (b), and Interface 3 (c)—which correspond to particles 1, 2, and 3, respectively.

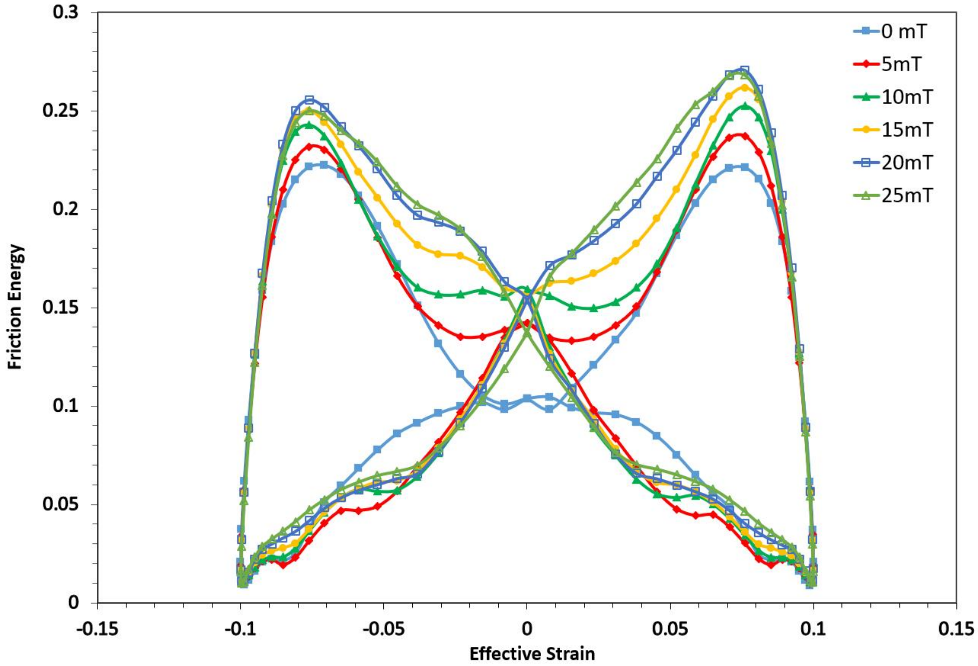

(a)

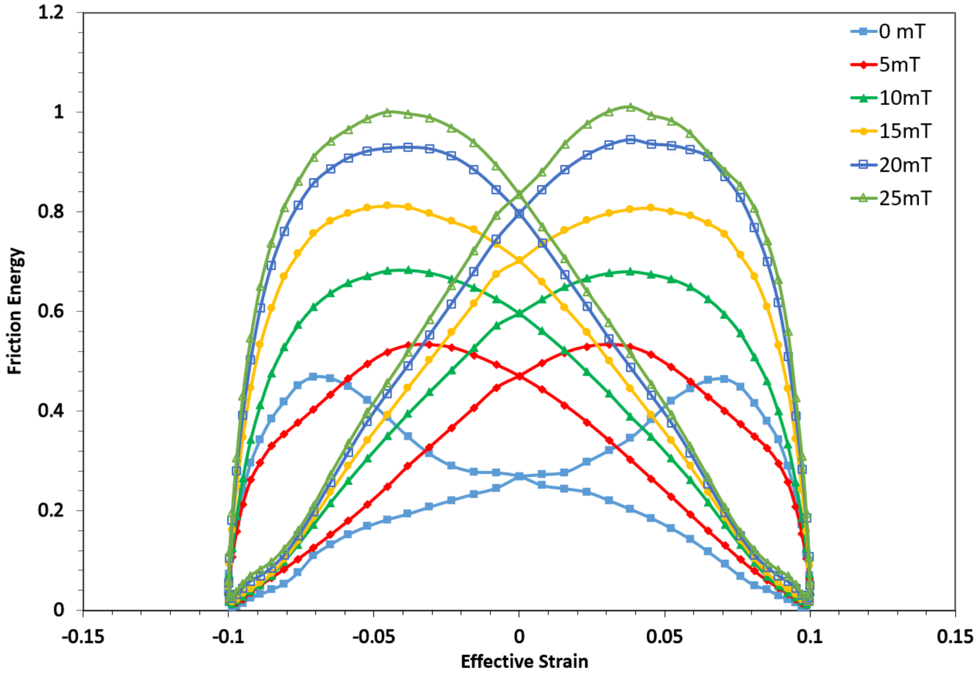

(b)

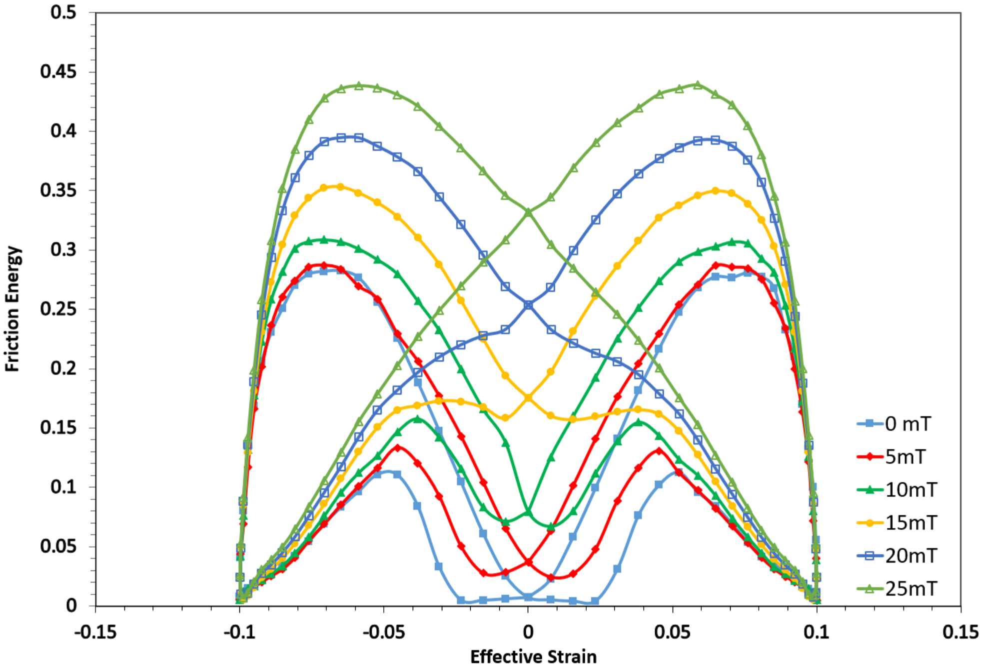

(c)

Figure 7.7 Friction energy of different interface conditions: (a) interface 1, (b) interface 2, (c) interface 3.

For all the interface conditions analyzed, the friction energy versus shear strain hysteresis curves exhibit a generally similar "butterfly" shape, indicative of distinct friction behaviors at each stage of cyclic loading and highlighting the highly nonlinear nature of these interactions. A key observation is that during the loading phase from zero to maximum shear amplitude, the friction energy is higher than during the unloading stage, resulting in the characteristic hysteresis behavior. Upon closer examination, the curves for different interface conditions reveal notable variations.

For Particle 1, with the application of a small magnetic field, there's an overall increase in friction energy, alongside noticeable changes in the curve shape at strain=0, there's a significant increase in value. However, as the magnetic field strength is further increased, the trend of change diminishes, and the zero-strain point shows little alteration, suggesting that during loading, when a magnetic field is applied, the particle adheres to the matrix at the bottom due to the magnetic force, hence the marked change at zero strain. However, further increasing the magnetic field doesn't affect the already bonded bottom part but only increases friction around it, hence the minimal change with higher magnetic fields.

Particle 2 appears to go through the three stages we previously hypothesized at low magnetic fields, the curve is highly nonlinear, indicating a complex interface behavior transitioning between static and dynamic friction. As the magnetic field increases, the curve begins to exhibit partially linear behavior, and further increases in the magnetic field result in value changes but no significant shape alterations, suggesting that the interface behavior has settled into Stage 2. At high magnetic fields, the increase in friction energy with magnetic field strength diminishes, indicating that the particles are nearing a partially fixed state where further increases in magnetic field have little effect on energy loss.

Particle 3, being symmetrically loaded, as the magnetic field increases, the increase in friction energy appears linear and does not diminish with further increases in the magnetic field. This unique behavior could be indicative of the symmetrical load distribution, allowing continuous linear increases in friction energy without the reductions observed in other particles. In Figure 7.8. we plot the total friction energy per cycle for these three cases by adding up the value at each time step.

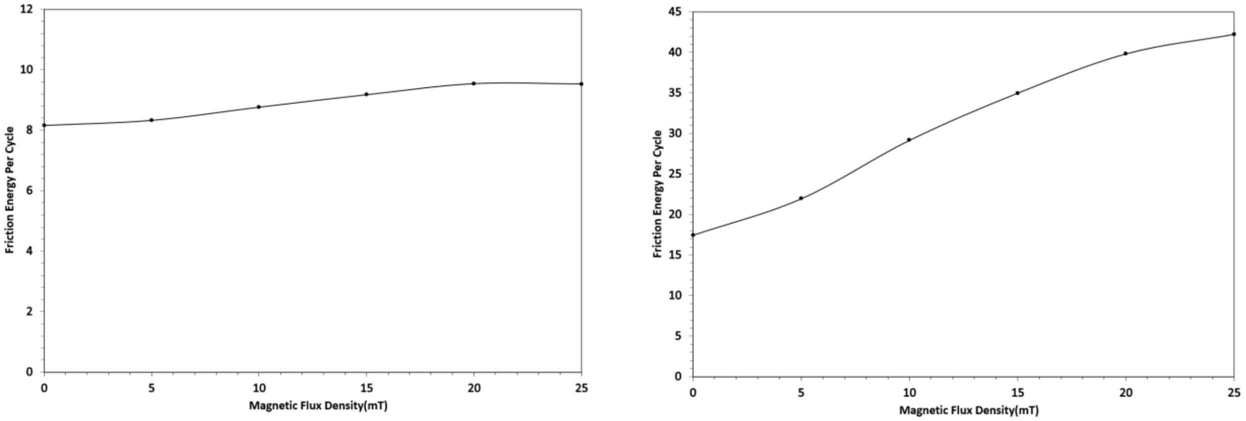

(a)

(b)

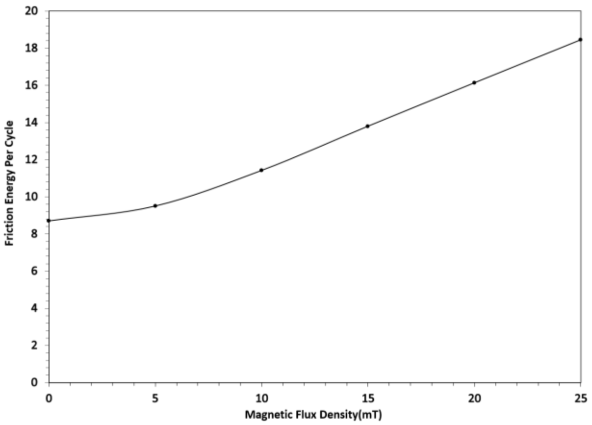

(c)

Figure 7.8 Friction energy per cycle of different interface conditions: (a) interface 1, (b) interface 2, (c) interface 3.

Figure 7.8 provides a comprehensive overview of the energy dissipation capabilities associated with particles exhibiting different interface behaviors under magnetic field influence. Particle 1 shows a minimal increase in friction energy with the application of a magnetic field and quickly reaches a plateau at a relatively low magnetic field strength. This indicates that Particle 1 has a limited ability to lose energy, suggesting that its interface condition does not significantly contribute to the overall damping properties of the MRE.

Particle 3 presents an interesting case; although it starts with a low initial friction energy value, it demonstrates a linear increase in friction energy relative to the magnetic field strength, continuing even at higher field strengths. However, this behavior is specific to the symmetrically loaded position of Particle 3 within the chain, making it a rare occurrence in practical scenarios. Consequently, while interesting, Particle 3's behavior does not typically represent common conditions in real-world applications of MREs, and thus does not require extensive focus in our modeling efforts.

Particle 2, on the other hand, is critical to our analysis. It is a common occurrence in chains and exhibits the highest friction energy among the particles. The friction energy for Particle 2 initially increases linearly with the application of a magnetic field but shows a reduction at higher strains. This behavior indicates that Particle 2's interface condition plays a significant role in influencing the damping properties of the MRE, particularly in how the MRE behaves under various magnetic field strengths and mechanical strains.

7.4.2 Modeling of Particle Rotation

We further extended our investigation by constructing a model to analyze particle rotation during the loading process, specifically focusing on Particle 2. We monitored the position of the middle node and the boundary nodes of Particle 2, calculating the rotation angle at every time point throughout the cyclic loading process. In Figure 7.9, the simulation results are displayed without a magnetic field, and different friction coefficients are considered. It's evident that while the curves are linear near the ends of the particle, there is a distinct loop curve in the middle region close to zero strain. This loop indicates the transition between static and dynamic friction experienced by the particle during the loading cycle. As the friction coefficient increases, this behavior intensifies, resulting in a larger and flatter loop in the middle region. Additionally, higher friction coefficients correlate with a decrease in the maximum rotation angle of the particle.

Figure 7.10 compares the rotation angle results with and without the application of a magnetic field at a 0.3 friction coefficient. The results demonstrate that the application of a magnetic field reduces the particle's rotation angle and introduces more nonlinearity in the curve's shape. However, the magnetic field restricts the transition between different friction behaviors during loading, resulting in less abrupt changes compared to scenarios with no magnetic field.

These findings indicate that particle rotation occurs only at very small values during the loading process. Moreover, with the increase of both magnetic field strength and friction coefficient, the particle becomes increasingly difficult to rotate, exhibiting even smaller rotation angles. In previous chapters, we noted that during simulations using the dipole method, the dipole moment is assumed to be perpendicular to the magnetic field, thus producing no torque. In this chapter, considering interface rotation necessitated a reevaluation of this behavior. However, our simulation results confirm that the rotation induced by shear loading is minimal, suggesting it does not significantly influence our overall simulation outcomes. Therefore, we conclude that it is unnecessary to consider this minor rotation in our broader analysis of MRE behavior under typical operational conditions.

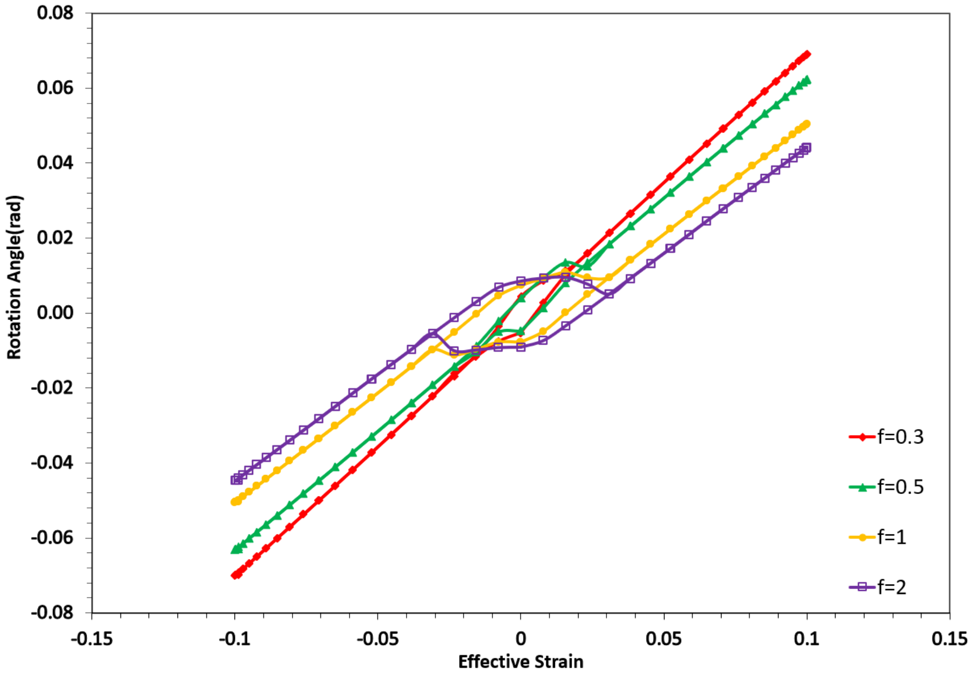

Figure 7.9 Rotation angle of particle 2 with different interface friction coefficients under cyclic loading.

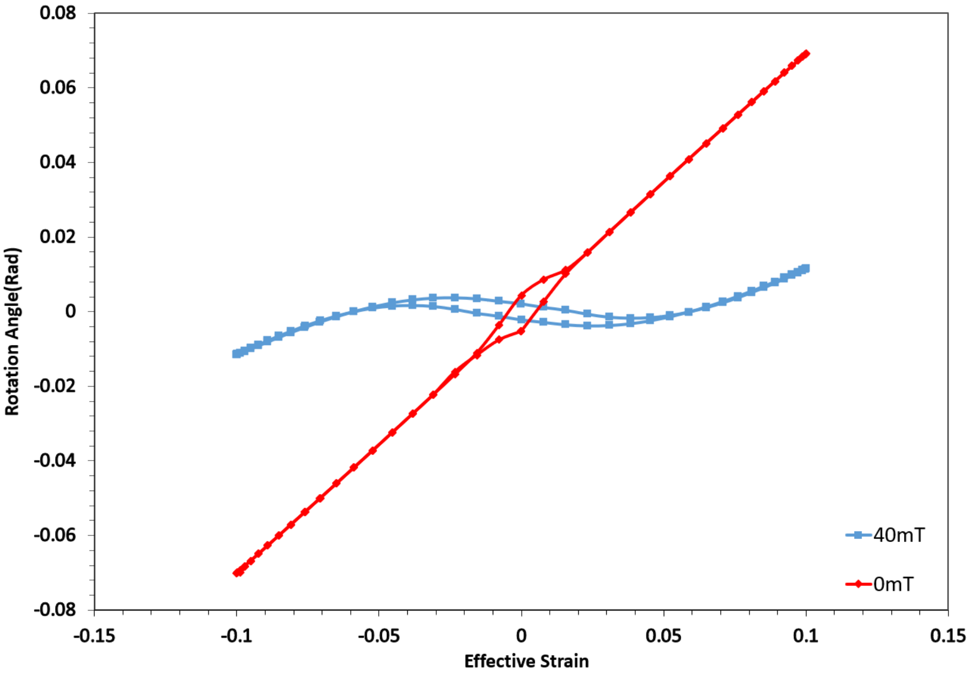

Figure 7.10 Rotation angle of particle 2 (f = 0.4) with and without magnetic field under cyclic loading.

7.5 Impact of Interface-Related Parameters on the Dynamic Behavior of MREs

In this section, we examine the impact of interface behavior on the dynamic modulus of MREs and explore how adjustments to model parameters can effectively control the predicted outcomes. We begin by analyzing how magnetic flux density and friction coefficient influence the dynamic modulus of MREs. Simulations are conducted with magnetic fields ranging from 0 mT to 70 mT, and friction coefficients set at 0, 0.1, 0.2, 0.4, and 0.8. The resulting data on storage modulus, loss modulus, and loss factor are presented in Figure 7.11 (a), (b), and (c), respectively.

In Figure 7.11 (a), the storage modulus for all friction coefficients displays a consistent linear increase as the magnetic field strength increases. Notably, a higher friction coefficient corresponds to a higher storage modulus, suggesting that the interface becomes stiffer with increased friction. This behavior is expected as the interface's resistance to shear deformation enhances the overall stiffness of the MRE.

Figure 7.11 (b) shows trends similar to those of the storage modulus but with notable distinctions at higher magnetic field strengths. For lower friction coefficients (0.1 and 0.2), the loss modulus curve flattens earlier, around 50 mT, and then maintains a linear behavior. In contrast, for higher friction coefficients (0.4 and 0.8), the loss modulus continues to increase even beyond 70 mT. This indicates that higher friction coefficients enhance the MRE's ability to dissipate energy, and this capacity continues to grow with increasing magnetic field strength, reaching saturation at higher levels.

Figure 7.11 (c) reveals a unique pattern for the loss factor. Unlike scenarios with fully bonded particles, the curve initially increases, reaches a maximum at a certain magnetic flux density, and then exhibits a linear decrease as the magnetic field continues to grow. This pattern reflects the cumulative effect of all interface types. As the magnetic field increases, the interfaces initially exhibit higher damping due to the magnetic force. However, at a certain point, the interface behavior transitions, leading to a smaller increase in loss modulus and a subsequent reduction in damping.

Furthermore, with increasing friction factor, the peak of the loss factor curve occurs at higher magnetic fields. The slope after reaching the peak also varies; higher friction coefficients result in a slower rate of decline. This behavior likely stems from the differential contributions and sensitivities of various interface types. While Interface 2 predominantly influences damping at lower magnetic fields, Interface 3 becomes more significant at higher fields because its energy loss capacity does not saturate with increasing magnetic field strength. Additionally, the energy loss ability of Interface 3 is linearly related to the friction coefficient, contributing to the trends observed in Figure 7.11 (c).

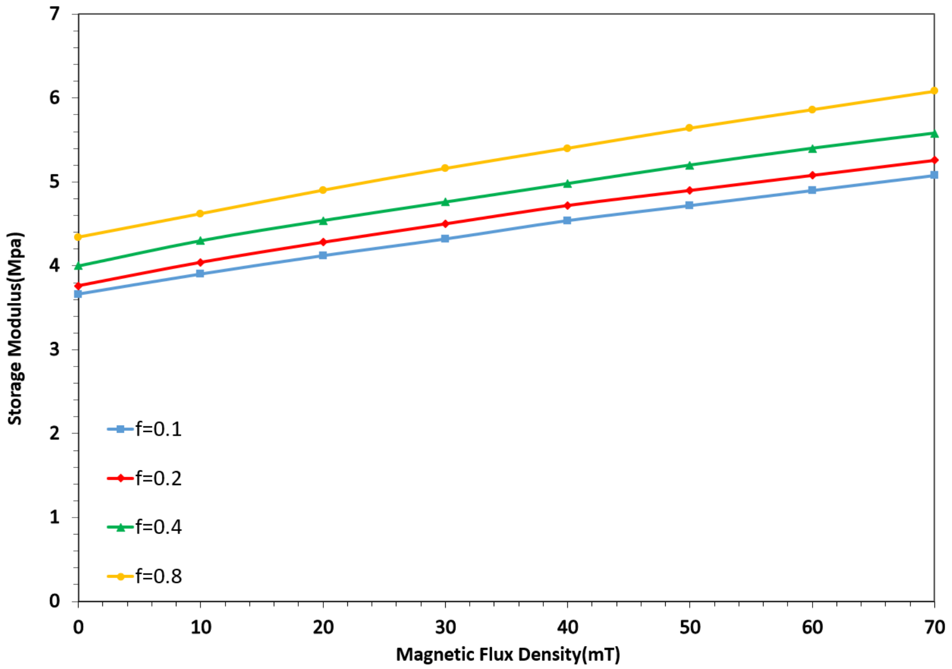
7
6
5
4
3
2
1
0
Storage Modulus(Mpa)
f=0.1
f=0.2
f=0.4
f=0.8
0
10
20
30
40
50
60
70
Magnetic Flux Density(mT)

(a)

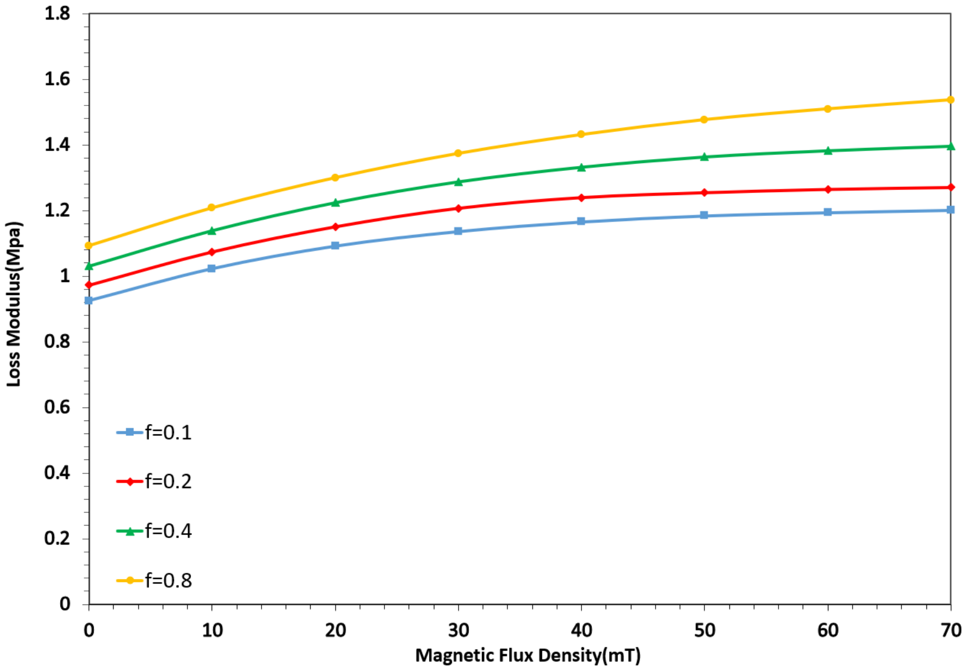
1.8
1.6
1.4
1.2
1
0.8
0.6
0.4
0.2
0
Loss Modulus(Mpa)
f=0.1
f=0.2
f=0.4
f=0.8
0
10
20
30
40
50
60
70
Magnetic Flux Density(mT)

(b)

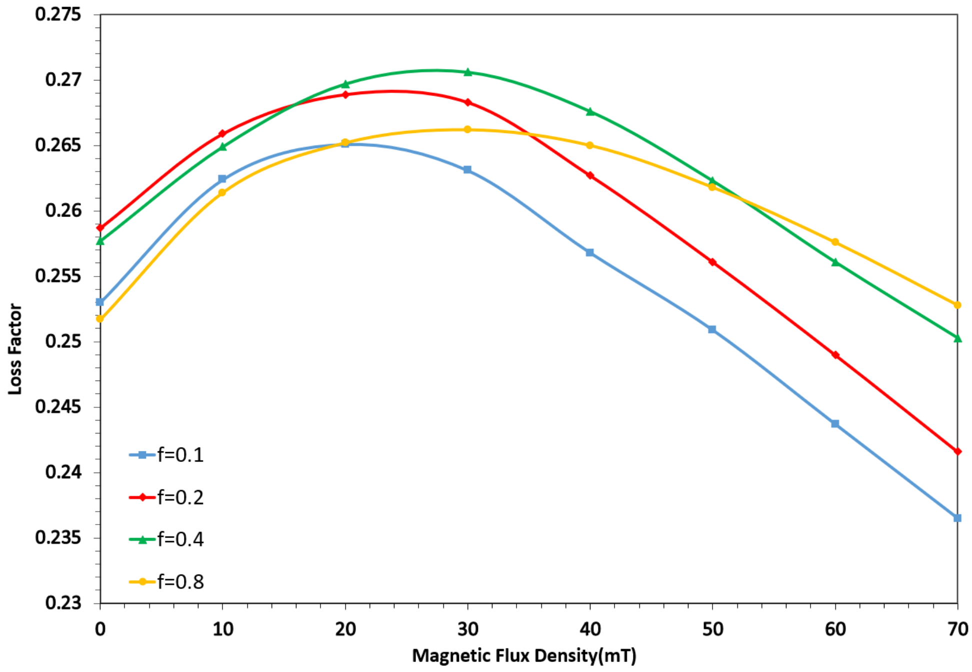

(c)

Figure 7.11 The influence of interface friction coefficient and magnetic flux density on (a) storage modulus, (b) loss modulus, (c) loss factor.

Based on the current results, while our models effectively capture the overall behavior, they exhibit certain limitations. Notably, the total increase in damping capacity is relatively modest, and the enhancement in damping tends to saturate at lower magnetic fields than desired. To enhance our model's ability to simulate higher energy loss over a broader operational range, several adjustments are considered. Increasing the friction coefficient has shown that it does not significantly enhance damping capacity, though it may contribute marginally to overall energy loss. Expanding the number of particles in the model increases the interface area, inherently boosting the potential for energy dissipation. We can further optimize the model by adjusting the ratio of particles with different interface conditions, specifically increasing particles with Interface 2 and reducing those with Interface 1. Additionally, reducing the size of each particle decreases the magnetic force exerted on individual particles, thereby delaying the saturation of the damping curve at higher magnetic fields.

To implement these strategies, new models that include more particles arranged in parallel chains while maintaining the same volume fraction are being developed. This setup not only increases interface areas but also moderates the magnetic force exerted on each particle due to the reduced size. Adjusting the number of particles allows for fine-tuning the proportion of different interface conditions, which optimizes the overall simulation results. To evaluate the efficacy of this new model, we simulated a scenario using two chains of five particles each and compared the loss factors with a single chain of the same volume fraction. The results shown in Figure 7.12 indicate that with two chains, the peak of the curve occurs at a significantly higher magnetic field. Moreover, the relative increase in loss factor from no magnetic field to the peak changes from 5% (single chain) to 10% (two chains), demonstrating a notable improvement in the model's ability to modulate the curve. These findings affirm our model's enhanced capability to adjust parameters effectively, giving us confidence in fine-tuning our simulations to better replicate experimental observations and achieve more accurate predictions of MRE behavior under varied conditions. This adaptable approach ensures our models remain robust and relevant, providing valuable insights for developing and optimizing MRE applications.

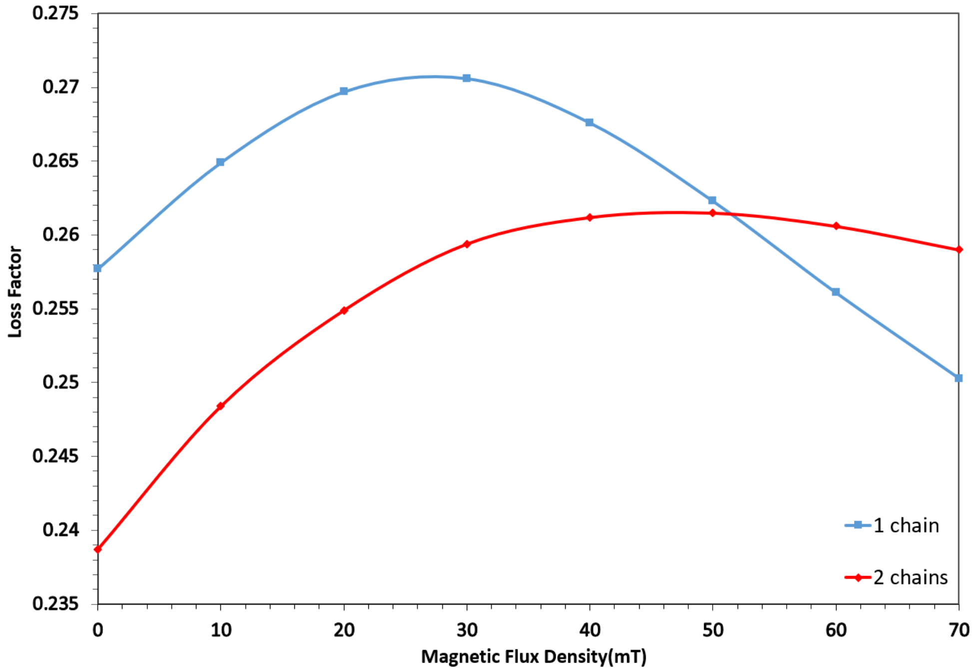

Figure 7.12 Impact of microsture on the loss factor in MREs.

7.6 Comparison of Model Predictions with Experimental Data

In this section, we utilize our previously developed model to compare with experimental findings. Our model is unique in its ability to capture the variation in damping ratio as magnetic field strength increases, exhibiting a peak in damping effectiveness. However, this peak is not commonly observed in most experimental studies. We find corroboration in the work of Li Jian-feng and Gong Xing-long [106], who also observed this behavior in their experiments. Their work is shown in Figure 7.13.

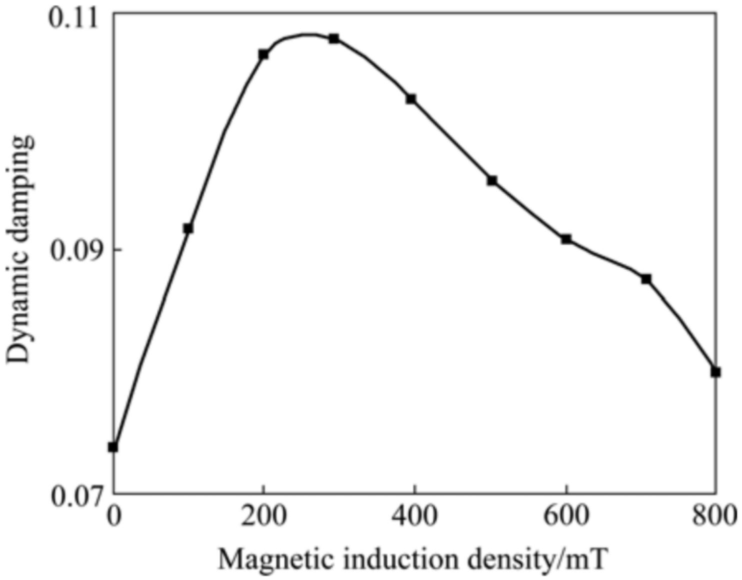

Figure 7.13 Variation of dynamic damping in MREs with applied magnetic field: Data from Li's experiment.

Their findings indicate that the dynamic damping of MREs significantly responds to the magnetic field strength, increasing up to a magnetic field of 200 mT and then decreasing beyond this point, creating a peak in damping at about 200 mT. This behavior is mainly attributed to the friction between iron particles and the rubber matrix, with larger test strain amplitudes leading to greater dynamic damping enhancements.

Further supporting our model's assumptions, experiments by Miao Yu et al. [107] with two types of MREs, one composed of pure carbonyl iron particles (CIPs) and the other using polyaniline-modified carbonyl iron particles (PANI-MRE) with enhanced interface bonding, provide additional insights. The results, shown in Figure 7.14, particularly in how the damping behavior varies with magnetic flux density, align with our predictions. In their experiments, while the loss factor for both types of MRE decreases with increasing magnetic flux, the PANI-MRE consistently shows a lower loss factor than the PURE-MRE. Notably, the PURE-MRE displays a small initial increase and peak in loss factor before dropping, a pattern absent in the PANI-MRE, where the curve directly decreases from the start.

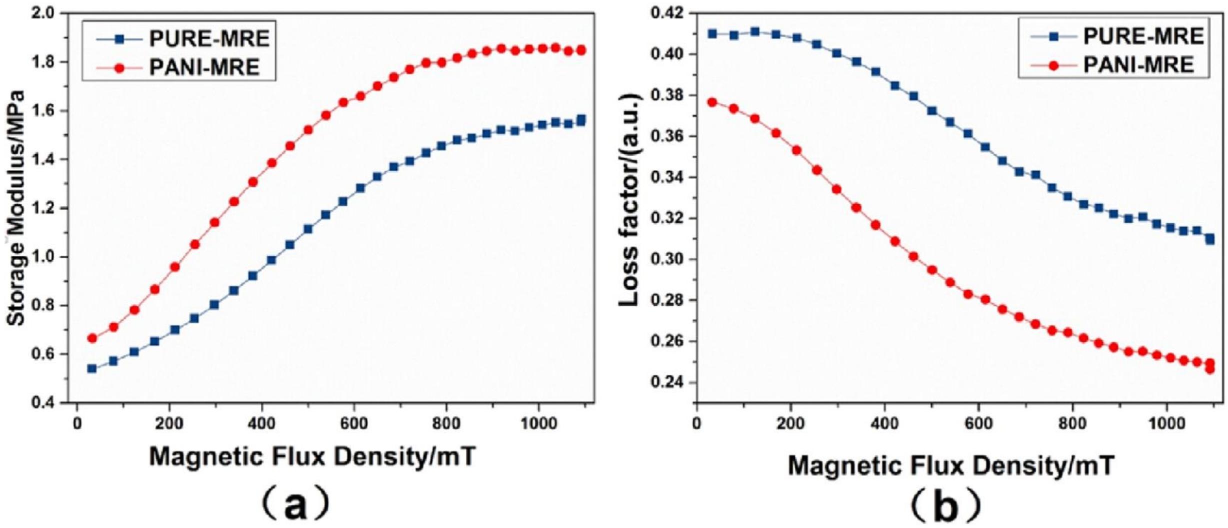

Figure 7.14 Dependence of the shear storage modulus (a) and loss factor (b) on the applied magnetic flux density: Data from Yu’s experiment.

This differential behavior between the two MRE types can be explained by our simulation, which suggests that an increase in damping ratio primarily occurs in situations with poor interface conditions. Well-bonded particle interfaces, such as those in PANI-MRE, do not exhibit this peak behavior, likely due to a lack of significant interface behavior change.

Combining insights from both experiments raises important questions about material and structural differences in MREs. The first experiment, likely using an orthotropic MRE where the magnetic field is applied during the curing process, shows more pronounced changes in damping behavior compared to the isotropic MRE used in the second experiment. Isotropic MREs are less likely to form long straight chains and hence tend to have more of what we've classified as Interface 1 conditions, which contribute minimally to peak damping behavior. Additionally, orthotropic structures, with initially applied strong magnetic fields and a stronger magnetorheological effect, are more prone to interface defects. Using our model, we postulate that the major differences in experimental outcomes can also be attributed to the alignment and structure of the MREs, with isotropic MREs displaying different interface dynamics compared to orthotropically aligned MREs.

We adjust our model parameters to align our predictions closely with the experimental results obtained from the studies we mentioned earlier. The results of these adjustments are displayed in Figure 7.15 (a) and (b), where we have carefully controlled the magnetic flux density not to exceed 500 mT to avoid effects from magnetic saturation. This parameter tuning has enabled both curves from the model to align well with the experimental data, demonstrating a good fit across the range tested.

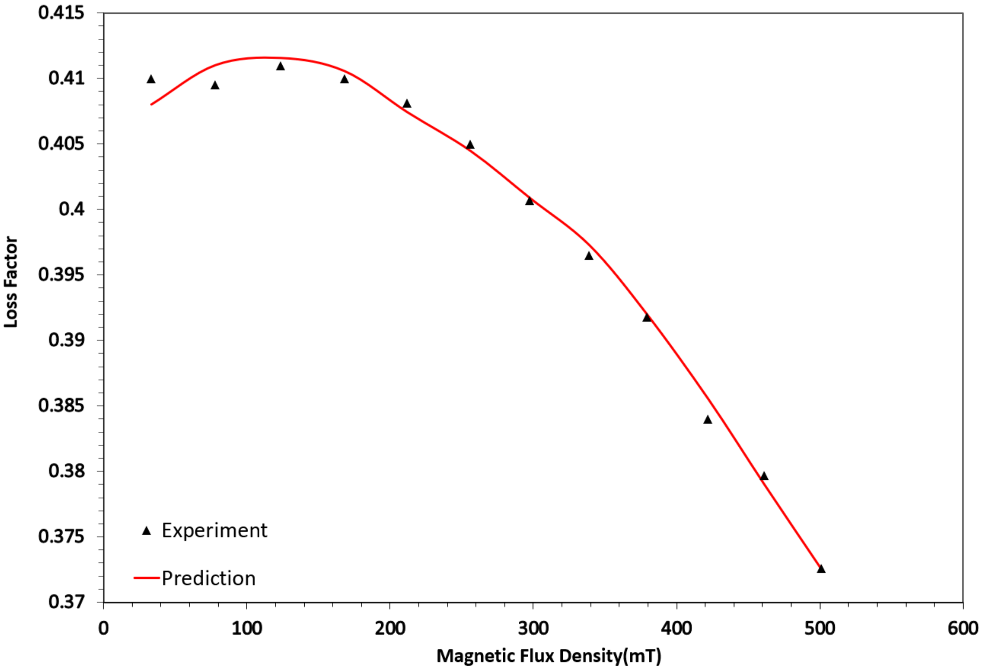

(a)

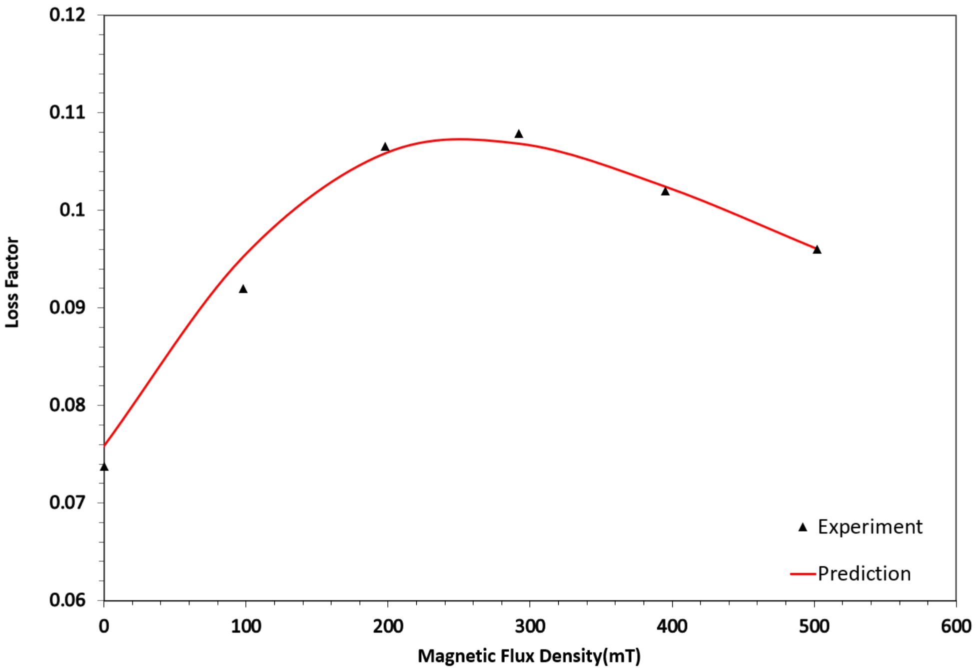

(a)

Figure 7.15 Comparison of model predictions with experimental results on loss factor: (a) Li’s experiment, (b) Yu’s experiment.

The behavior of the curves before reaching the peak is primarily influenced by interface-related parameters such as friction coefficient, type of interface, and the extent of interface areas. These factors play a crucial role in shaping the initial increase in damping characteristics as they directly impact how the particles interact with the matrix and each other under varying magnetic field strengths. After the peak, the loss modulus tends to stabilize, and the slope of the curve becomes more dependent on material properties rather than interface dynamics. This transition indicates that beyond a certain point, the intrinsic properties of the materials—such as their elastic and viscoelastic characteristics—become more significant in determining the overall dynamic response of the MRE. This change underscores the dual influence of interface mechanics and material properties in MRE behavior, highlighting the need for a nuanced understanding of both to accurately predict and control the performance of MRE systems in various applications.

7.7 Conclusions

In Chapter 7, a comprehensive analysis was conducted on the interface behaviors of MREs using various simulation strategies. Several algorithms were employed, like the Cohesive Zone Model for simulating debonding dynamics and a detailed friction energy model that captured distinct friction behaviors of particles at different locations within a chain structure. By categorizing particles into three specific interface conditions, the study effectively elucidated the damping behavior changes observed at low magnetic fields—a phenomenon not thoroughly explained by prior research. Furthermore, the simulations were able to mirror experimental results closely, offering a robust model replete with physically based parameters that can be fine-tuned. This model not only clarifies underlying physical mechanisms but also holds significant potential to refine and enhance existing phenomenological models, providing a solid foundation for future explorations aimed at optimizing MRE technology in practical applications.

Chapter 8 Instability Analysis of Magnetorheological Elastomers (MREs)

8.1 Introduction

In this chapter, we focus on the instability analysis of MREs, particularly under compression, as they are commonly used as isolators in various applications. While previous chapters have primarily addressed MRE behavior under cyclic shear loading, it is crucial to understand how these materials perform under compressive loads due to their heterogeneous nature, which can lead to various types of instability. We categorize the potential instabilities into three types: macroscopic, microscopic, and interface instabilities.

8.2 Modeling of Macroscopic Instability

Macroscopic instabilities, often referred to as long-wave instabilities, are typically examined through the lens of the effective behavior resulting from various homogenization schemes. These instabilities are particularly significant in nonlinear fiber composites, where the mechanics of nonlinear composites have demonstrated that macroscopic instabilities arise when the homogenized properties lose strong ellipticity. A general criterion for the onset of macroscopic instability of the MREs was proposed by Rudykh and Bertoldi [108] based on the general criterion of the theory of bifurcation and stability. We employ a sextic polynomial equation to analyze such instabilities[109], as shown below.

$$\mathit{\Gamma}_6\xi^6 + \mathit{\Gamma}_5\xi^5 + \mathit{\Gamma}_4\xi^4 + \mathit{\Gamma}_3\xi^3 + \mathit{\Gamma}_2\xi^2 + \mathit{\Gamma}_1\xi + \mathit{\Gamma}_0 = 0\,, \tag{8-1}$$

The onset of macroscopic instability along a magneto-mechanical loading path is indicated by the existence of a non-trivial real solution to this polynomial equation. The factors $\mathit{\Gamma}_i$ can be obtained using the following equations:

$$\mathit{\Gamma}_0 = \mathcal{M}_{121}^2 - \mathcal{M}_{2121}\xi_{11} \,, \tag{8-2}$$

$$\mathit{\Gamma}_1 = 2\big(-\mathcal{M}_{2121}\xi_{12} + (\mathcal{M}_{1121} - \mathcal{M}_{2122})\xi_{11} + \mathcal{M}_{121}(\mathcal{M}_{221} + \mathcal{M}_{122} - \mathcal{M}_{111})\big) \,, \tag{8-3}$$

$$\begin{aligned} \mathit{\Gamma}_2 = {} & -\mathcal{M}_{2121}\xi_{22} + 4(\mathcal{M}_{1121} - \mathcal{M}_{2122})\xi_{12} - \\ & (\mathcal{M}_{1111} - 2\mathcal{M}_{1122} - 2\mathcal{M}_{1221} + \mathcal{M}_{2222})\xi_{11} \\ & -2\mathcal{M}_{121}(\mathcal{M}_{112} + \mathcal{M}_{121} - \mathcal{M}_{222}) + (\mathcal{M}_{122} + \mathcal{M}_{221} - \mathcal{M}_{111})^2 \,, \end{aligned} \tag{8-4}$$

$$\begin{aligned} \mathit{\Gamma}_3 = {} & -2(\mathcal{M}_{1112} - \mathcal{M}_{1222})\xi_{11} + (\mathcal{M}_{1111} - 2\mathcal{M}_{1122} - 2\mathcal{M}_{1221} + \mathcal{M}_{2222})\xi_{12} \\ & +(\mathcal{M}_{2122} - \mathcal{M}_{1121})\xi_{22}n + \big(\mathcal{M}_{121}\mathcal{M}_{122} - \mathcal{M}_{221}(\mathcal{M}_{112} + \mathcal{M}_{121} - \mathcal{M}_{222})\big) \,, \end{aligned} \tag{8-5}$$

$$\begin{aligned} \mathit{\Gamma}_4 = {} & -(\mathcal{M}_{1111} - 2\mathcal{M}_{1122} - 2\mathcal{M}_{1221} + \mathcal{M}_{2222})\xi_{22} - 4(\mathcal{M}_{1112} - \mathcal{M}_{1222})\xi_{12} \\ & -\mathcal{M}_{1212}\xi_{11} + (\mathcal{M}_{112} + \mathcal{M}_{121} - \mathcal{M}_{222})^2 + 2\mathcal{M}_{122}(\mathcal{M}_{111} - \mathcal{M}_{122} - \mathcal{M}_{221}) \,, \end{aligned} \tag{8-6}$$

$$\mathit{\Gamma}_5 = 2\big((\mathcal{M}_{1222} - \mathcal{M}_{1112})\xi_{22} - \mathcal{M}_{1212}\xi_{12} + \mathcal{M}_{122}(\mathcal{M}_{112} + \mathcal{M}_{121} - \mathcal{M}_{222})\big) \,, \tag{8-7}$$

$$\mathit{\Gamma}_6 = \mathcal{M}_{122}^2 - \mathcal{M}_{1212}\xi_{22} \,. \tag{8-8}$$

To obtain all necessary parameters for these equations, we implement specific mechanical and magnetic boundary conditions in our model, detailed as follows:

$$\bar{\boldsymbol{F}}^{[1]} = \bar{\lambda}e_1 \otimes e_1 + \delta\bar{\gamma}e_1 \otimes e_2 + \bar{\lambda}^{-1}e_2 \otimes e_2 + e_3 \otimes e_3 \,, \tag{8-9}$$

$$\bar{\boldsymbol{F}}^{[2]} = \bar{\lambda}e_1 \otimes e_1 + \bar{\lambda}^{-1}e_2 \otimes e_2 + \delta\bar{\gamma}e_2 \otimes e_1 + e_3 \otimes e_3 \,, \tag{8-10}$$

$$\bar{\boldsymbol{F}}^{[3]} = (\bar{\lambda} + \delta\bar{\lambda})e_1 \otimes e_1 + (\bar{\lambda} + \delta\bar{\lambda})^{-1}e_2 \otimes e_2 + e_3 \otimes e_3 \,, \tag{8-11}$$

$$\bar{\boldsymbol{H}}^{[1]} = (\bar{H}_1 + \delta\bar{H})e_1 + \bar{H}_2e_2 \,, \tag{8-12}$$

$$\bar{\boldsymbol{H}}^{[2]} = \bar{H}_1e_1 + (\bar{H}_2 + \delta\bar{H})e_2 \,, \tag{8-13}$$

where $\bar{\lambda}$ is the average stretch in the x direction, $\bar{\boldsymbol{H}}$ is the average magnetic field intensity. And $\delta\bar{\gamma}$, $\delta\bar{\lambda}$ and $\delta\bar{H}$ are the unit increments. By applying these incremental changes to the boundary conditions, we can obtain the homogenized response of the MRE models and determine the following magnetoelastic moduli:

$$\mathcal{M}_{ijkl} = \bar{F}_{jj}^{[0]}\bar{F}_{ll}^{[0]}\frac{\bar{P}_{ij}(F^{[m]},H^{[0]})-\bar{P}_{ij}(F^{[0]},H^{[0]})}{\delta\gamma},\ k \neq l,\ m = 1,2\ ; \tag{8-14}$$

$$\mathscr{M}_{ijk} = \frac{\bar{T}_{ij}(\bar{F}^{[0]},\bar{H}^{[n]})-\bar{T}_{ij}(\bar{F}^{[0]},\bar{H}^{[0]})}{\delta\bar{H}},\ n = 1,2\ ; \tag{8-15}$$

$$\mathscr{M}_{ij} = \frac{\bar{B}_{i}(\bar{F}^{[0]},\bar{H}^{[n]})-\bar{B}_{i}(\bar{F}^{[0]},\bar{H}^{[0]})}{\delta\bar{H}},\ n = 1,2\ ; \tag{8-16}$$

By utilizing Eqs. (8-14) through (8-16), we can determine all the components of the magneto-elastic tensors necessary for calculating the coefficients Γ_i. We utilize our previously developed straight-chain models for the instability simulation, which consists of six particles. To induce instability behaviors, we adjust the model to have larger inter-particle distances and smaller particle radii. A unit cell of this configuration is depicted in the accompanying Figure 8.1. In this model, m represents the height of the unit cell, n its length, and r the particle radius. We have selected a height-to-length ratio (m/n) of 0.5 and a radius-to-height ratio (r/m) of 0.333.

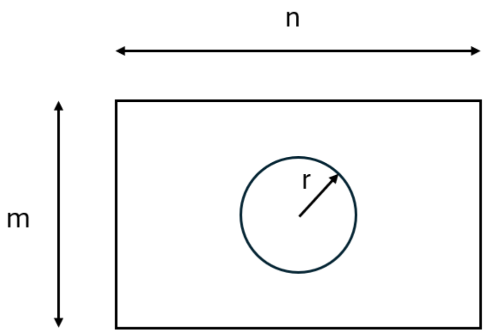

Figure 8.1 Sketch of a unit cell.

We conducted an examination of our model's response under various conditions. The following analysis, shown in Figure 8.2, explores the relationship between the critical compressive strain—which indicates the onset of macroscopic instability—and the applied magnetic field strength. We intentionally limited the magnetic field strength to a lower range of 0-400 mT to minimize the effects of magnetic saturation and to simplify the analysis of nonlinear behaviors.

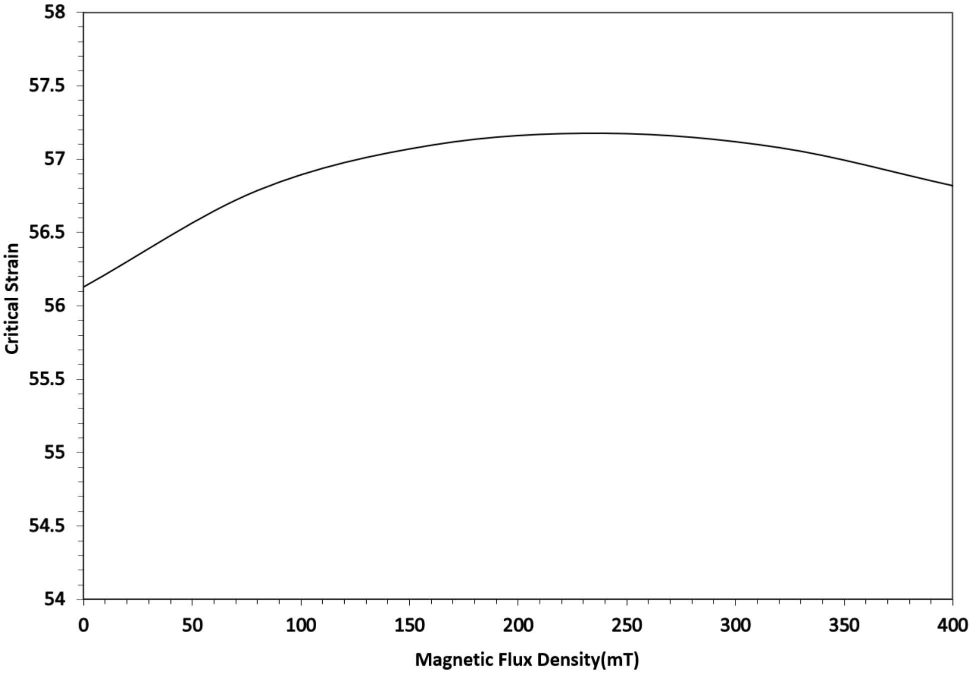

Figure 8.2 Critical compressive strain vs. applied magnetic field strength.

Our findings reveal that within this controlled range of magnetic field intensity, the magnetic field's impact on instability behavior is relatively subtle yet significant. Initially, the magnetic field acts to stabilize the MRE system by slightly increasing the critical strain threshold. This suggests that the presence of the magnetic field reinforces the material's structure, making it more resistant to deformation and instability at low magnetic flux densities. However, as the magnetic field strength approaches the middle of our testing range, a reversal in behavior occurs.

The MRE begins to show signs of destabilization, with a reduction in the critical strain required for the onset of instability. This pivotal behavior, where the magnetic field transitions from a stabilizing to a destabilizing factor, aligns with observations from other research, particularly in studies that extend the magnetic field strength beyond our tested range. These studies indicate that at very high intensities, the magnetic field significantly contributes to destabilizing the MRE, underscoring the dual role of magnetic fields depending on their intensity.

8.3 Modeling of Microscopic Instability

In this section, we delve into microscopic instability. While macroscopic analyses can predict critical values based on homogenized properties, instabilities can also manifest at smaller scales comparable to the microstructure's characteristic lengths. To explore these local instabilities and potential post-buckling behaviors, we conduct simulations that focus on the positional changes of particles within the structure.

To induce post-buckling patterns, we introduced small amplitude geometrical imperfections by perturbing the initial geometry, specifically the locations of the inclusion central points. These initial displacement amplitudes were implemented randomly to prevent the induction of predetermined buckling patterns. For each particle in the chain, we calculate their relative horizontal displacement to the center of the chain during the deformation process. Monitoring these displacement changes allows us to identify the onset of instabilities and determine the corresponding critical strain values.

Figure 8.3 illustrates the results for the top three particles within an RVE characterized by a ratio of m/n=0.5 and r/m=0, specifically identifying (a) particle 1, (b) particle 2, and (c) particle 3. The horizontal central displacement of the particles is normalized by dividing the radius r to obtain the displacement ratio q. It can be observed that for all particles, the displacement initially grows linearly with the strain with tiny changes, then at a critical point, marked by a sudden change in the rate of displacement around 0.33, instability sets in, as indicated by the red dashed line. Beyond this point, the displacement continues to change linearly but at a much steeper rate.

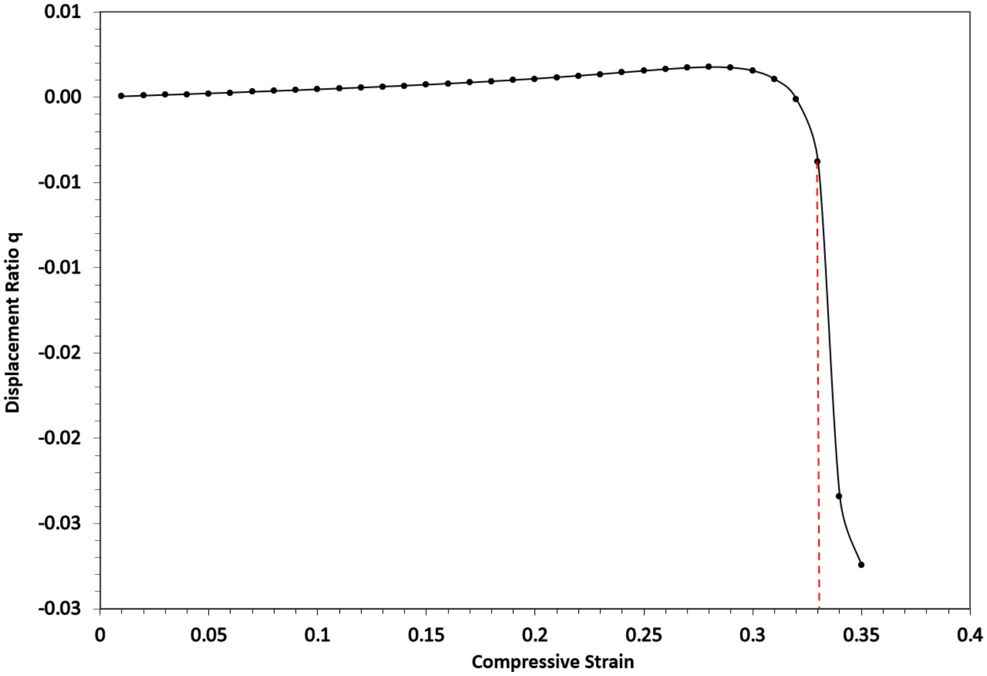

(a)

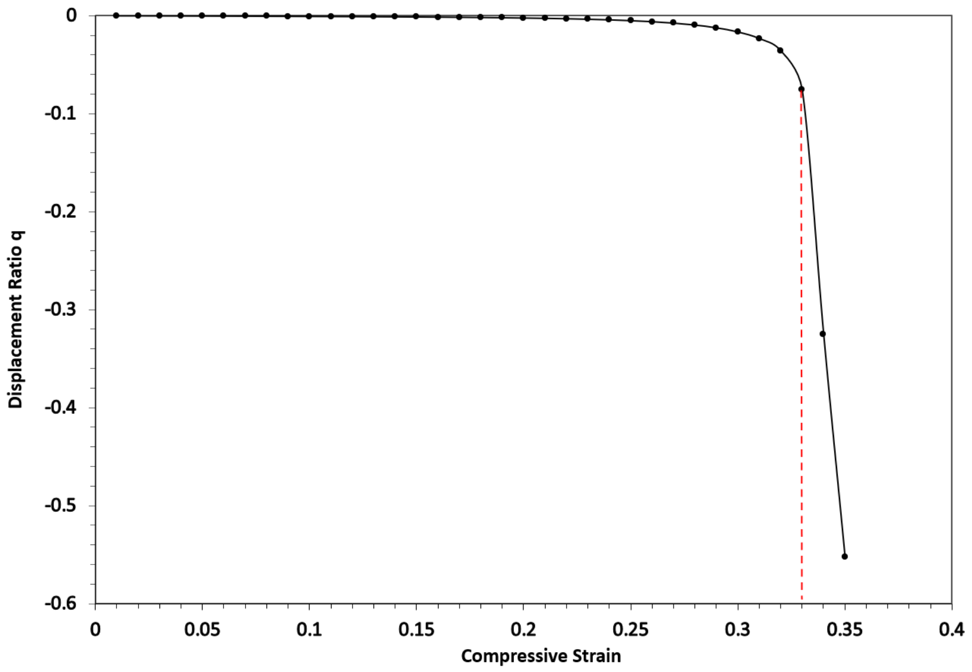

(a)

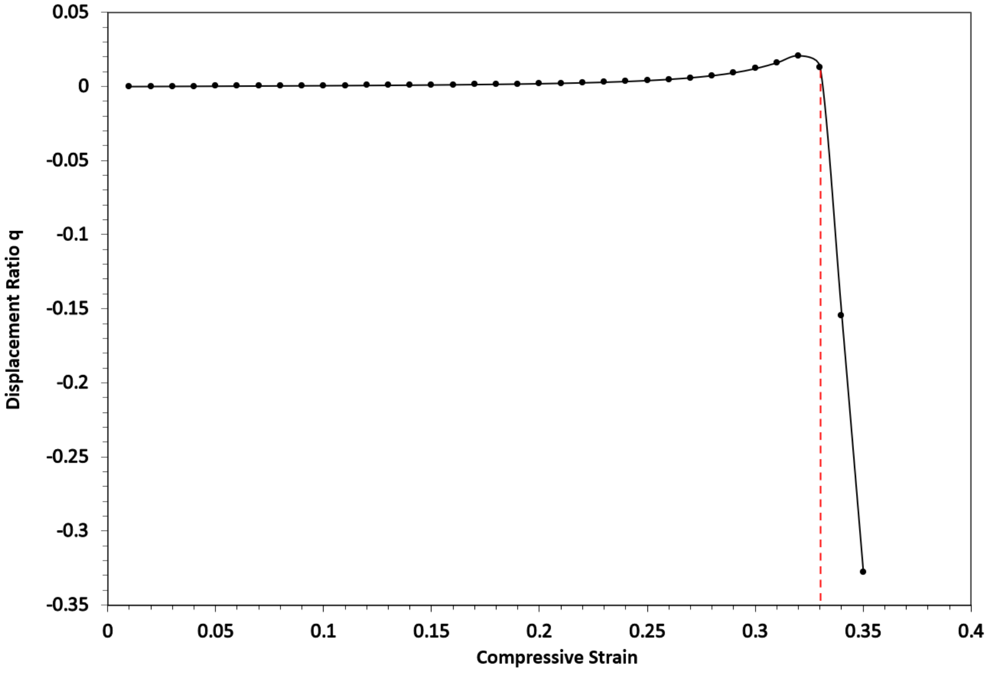

(a)

Figure 8.3 Critical strain detection using the first three particles of a six-particle chain model: (a) particle 1, (b) particle 2, (c) particle 3.

Additionally, the slight variance in critical strain values among the particles highlights the impact of local positioning and interaction within the chain. This variance suggests that the mechanical response of MREs can be highly localized, with specific regions within the material exhibiting different thresholds for instability based on their microstructural configuration. To further validate these findings, the strain distribution graph near the critical point is shown in Figure 8.4. The strain distributions at 0.32 and 0.33 are nearly symmetric, but a significant change in distribution is evident at 0.34, suggesting that the critical strain lies between 0.33 and 0.34. The dramatic shift in strain distribution at a strain of 0.34 compared to more symmetric distributions at lower strains illustrates how rapidly material behavior can change as it approaches and surpasses critical thresholds.

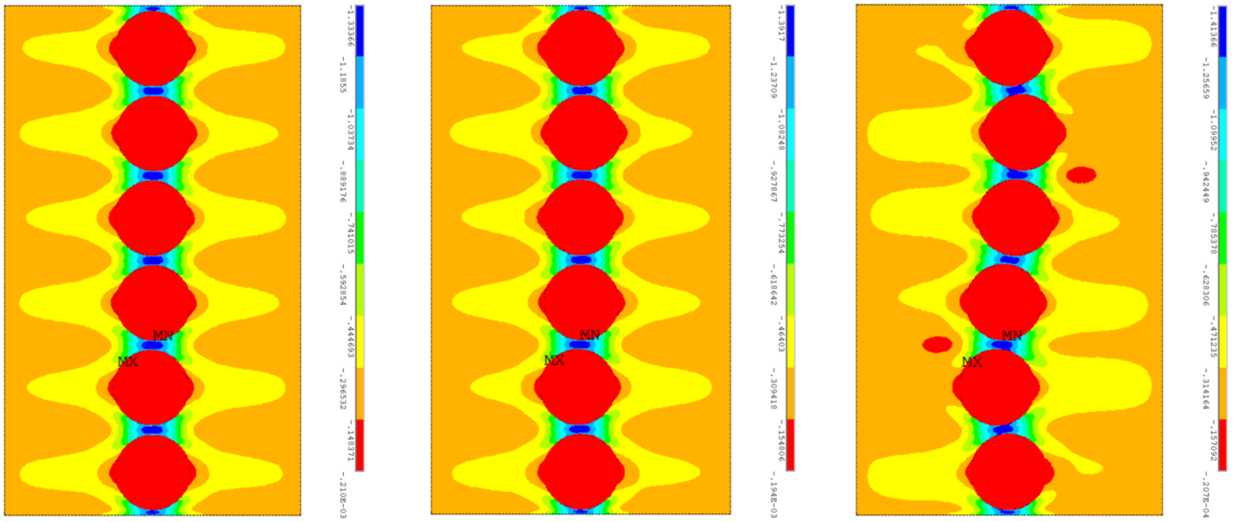

Figure 8.4 Strain distribution (ε_{yy}) in the MRE model, with compressive strain at (a) 0.32, (b) 0.33, (c) 0.34.

We further explore the relationship between particle radius and critical strain as depicted in Figure 8.5. It's important to note that to accurately determine the critical strain, analyzing the rate of change rather than displacement provides a clearer indication due to a distinct peak observed in the data. However, this method might slightly overestimate the strain since it necessitates a specific load step for accurate calculation. Therefore, we employ both methodologies to ensure the accuracy of our findings. In this simulation, we utilize the normalized radius factor r/m instead of the absolute radius r. The analysis indicates a clear correlation between particle radius and critical strain, showing that an increase in particle size leads to a decrease in the critical strain required for buckling.

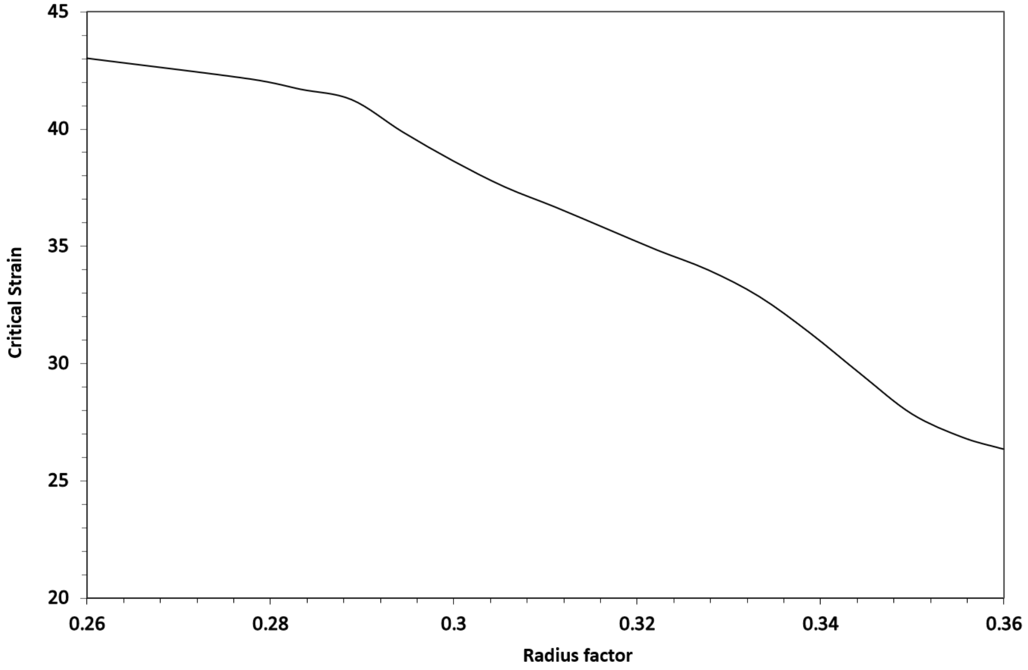

Figure 8.5 Dependence of critical strain on particle radius.

This phenomenon can be attributed to the mechanical dynamics within the matrix. As particle size increases, the matrix area between particles diminishes, resulting in higher localized strains within these narrower matrix sections under the same compression strain. This creates significant stress concentrations, which are particularly pronounced due to the hyperelastic model used in the simulations. The characteristics of the hyperelastic model employed significantly influence the susceptibility of the system to buckling. Depending on their parameter settings, different hyperelastic models can have varying impacts on the results. Models that exhibit a larger increase in stiffness at higher strains tend to contribute more to the onset of instability. Studying the critical strain alone is not comprehensive enough to understand the behavior of MREs under compressive loading. To delve deeper, we simulate the changes in shear stiffness throughout the progression of compressive loading. Initially, we simulate the compression process to capture the buckling behavior, storing all historical data. Subsequently, for each compression loading strain, treated as a timestep, we apply a unit shear deformation to the original model to obtain the effective shear modulus at the corresponding compressive strain level. To ensure that the additional shear does not prematurely trigger buckling, we verify these results by applying varying increments of shear deformation.

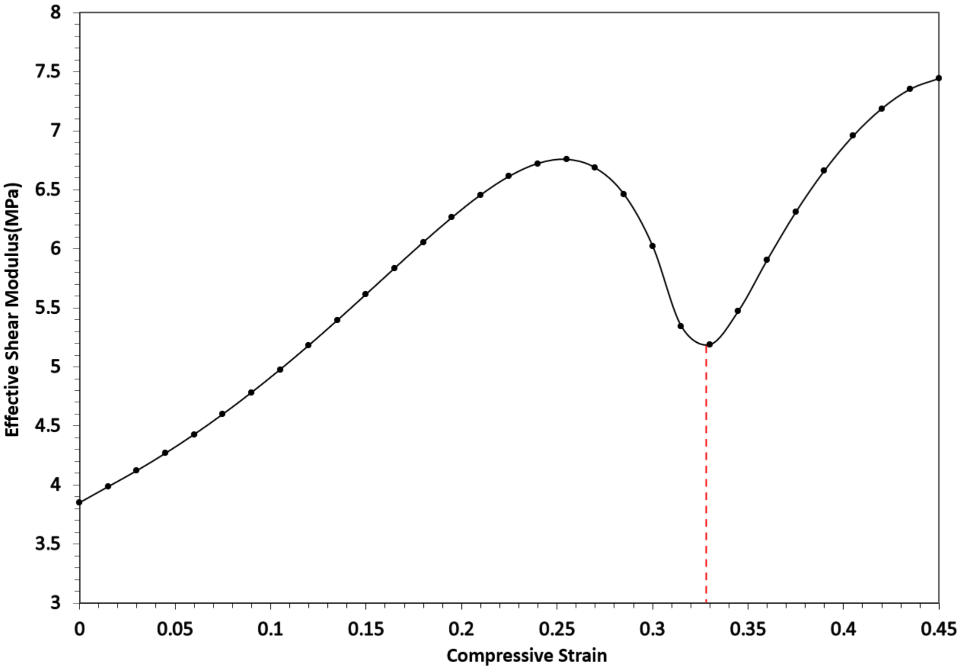

Figure 8.6 Effective shear modulus vs. compressive strain of MRE with a straight chain.

The results, illustrated in Figure 8.6, highlight a particular behavior where the effective shear modulus of the MRE initially increases with compressive strain due to the hyperelastic properties of the matrix. However, this modulus reaches a peak at approximately 0.25 strain and then begins to decrease, continuing until about 0.34 strain, where it starts to increase again. Notably, the critical strain where buckling occurs is at 0.34, as indicated by the red dashed line representing the central displacement method. This suggests that the MRE undergoes a reduction in shear stiffness prior to buckling and that stiffness begins to slightly increase at post-buckling.

Our interpretation of this phenomenon elucidates the interplay between compressive and shear strains in MREs. Initially, as particles are aligned in straight chains, applying a minor compressive strain will enhance the shear modulus due to the hyperelastic nature of the matrix. As strain levels increase, areas within these particle chains endure higher stresses compared to the surrounding matrix, leading to unbalanced stress concentrations. When a small shear strain is subsequently introduced to measure the effective shear modulus, this accumulated stress attempts to alleviate itself by extending the matrix along the shear direction. This action precipitates a new buckling behavior induced by coupling compressive and shear strains, which we call shear buckling. This buckling leads to stress relaxation and a rearrangement of particles, reducing the shear modulus. This buckling phenomenon primarily occurs after an initial shear is applied. If further compression is applied at this stage, it intensifies the stress concentration solely in compression conditions. After the unit shear application, the release of stress and subsequent particle movement becomes more pronounced, leading to an even greater reduction in shear modulus.

After buckling due to compression, stress redistribution occurs as particles rearrange and form new structural patterns. Since the stress has already been released during the initial buckling phase, subsequent shear strains will not cause further buckling in the microstructure. As a result, additional increases in compressive strain do not introduce more unbalanced stress within the matrix. This behavior indicates that shear buckling occurs earlier than compressive buckling in MREs with straight chains, which should be a focal point for further study and consideration in material design and simulation strategies.

To gain further insight into the behavior observed previously, we conducted simulations with particles arranged in wave-like chains. A diagram of this arrangement is shown in Figure 8.7, where v is the vertical distance between adjacent particles, and h is their perpendicular distance. With v fixed according to our experimental setup, we use the normalized parameter p=h/r to characterize the shape of the wavy chains. The results of these simulations are detailed in the accompanying Figure 8.8.

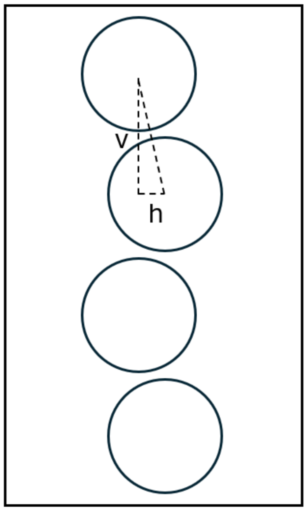

Figure 8.7 Geometry of the particle wavy chain: An illustration.

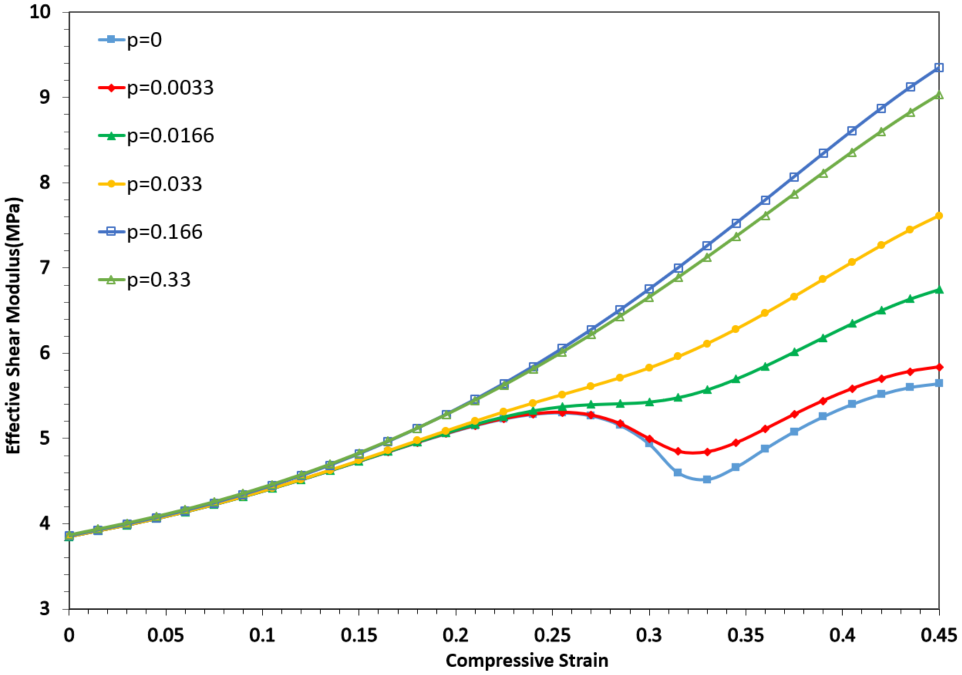

Figure 8.8 Effective shear modulus vs. compressive strain of MRE with wavy chains.

The result confirms our previous interpretations. When p is small, indicating that the chains are nearly straight, the phenomenon of shear buckling—where shear stiffness decreases with compression—can still be observed. Moreover, as the magnetic field strength increases, this behavior becomes less pronounced but remains noticeable. For configurations with higher p values, the curve exhibits a uniform increase akin to that of pure rubber, displaying no decreasing behavior. At even higher p values, differences in the curve become minimal.

This behavior is attributed to the particle distribution within the chains. When horizontal distances between particles are sufficient, under compression, the particles in the wavy chain can shift naturally without resulting in stress concentration behavior.

These findings also indicate that buckling behavior is closely linked to stress concentrations within the matrix inside the chains. Additionally, to mitigate the risk of instability, it is advisable to employ MREs with wavy chains. This configuration reduces the likelihood of stress concentrations that lead to instability, making wavy chains a more stable choice in applications where maintaining structural integrity under compression is critical.

Our next focus is on the stability of MREs under the influence of a magnetic field. Figure 8.9 illustrates how the critical strain varies in relation to the strength of the magnetic field. Observations from the graph reveal that, although microscopic instability tends to manifest earlier than macroscopic instability, both exhibit a similar trend in response to changes in magnetic field strength.

Initially, as the magnetic field strength increases, it acts to stabilize the MRE by increasing the critical strain, thereby enhancing the material's resistance to deformation. This initial stabilization phase indicates that the magnetic field effectively reinforces the structural integrity of the MRE. However, a turning point is reached at a certain magnetic field strength where the trend reverses; beyond this point, further increases in the magnetic field begin to destabilize the MRE, resulting in a decrease in the critical strain. Interestingly, the total change in critical strain over the range of magnetic field strengths tested is relatively small. This suggests that while the magnetic field has a noticeable impact on the stability of MREs, the overall susceptibility of these materials to magnetic-field-induced changes in stability is somewhat limited.

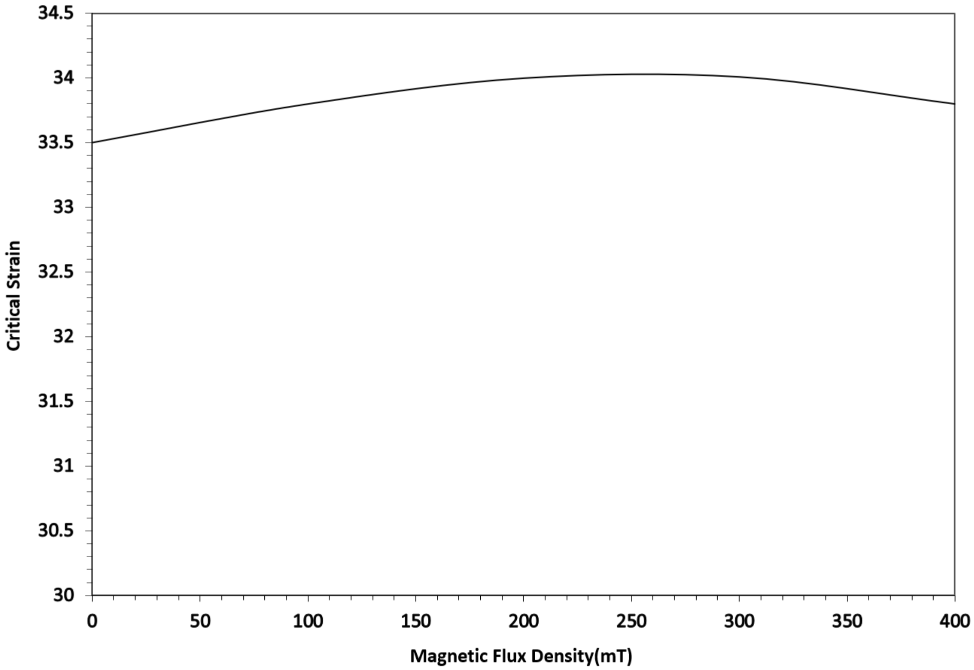

Figure 8.9 Influence of magnetic flux density on critical strain.

Figure 8.10 presents the variation in effective shear modulus during compression, comparing scenarios with and without an applied magnetic field. Notably, the curve representing the scenario with a magnetic field starts with a higher shear stiffness, attributable to the MR effect, which enhances the material's initial stiffness. Both curves generally follow the same trend; however, discrepancies become apparent at specific points. When each curve reaches its peak value, the one with the magnetic field demonstrates a more rapid decline, signaling a reduction in the absolute MR effect. This sharper drop continues until it reaches a second critical point—corresponding to the onset of buckling. Beyond this point, the curve with the magnetic field exhibits a slightly steeper increase compared to the curve without the magnetic field, indicating a marginal rise in the absolute MR effect.

This behavior suggests that while the magnetic field initially boosts the shear stiffness of the MRE, contributing positively to its structural integrity, it also leads to a faster reduction in MR effectiveness once the material's load-bearing capacity is maximized. The subsequent slight increase post-buckling could be due to the reorientation or redistribution of the magnetic particles within the matrix, possibly enhancing the interaction between the magnetic field and the material, thereby slightly increasing the MR effect under post-buckling conditions.

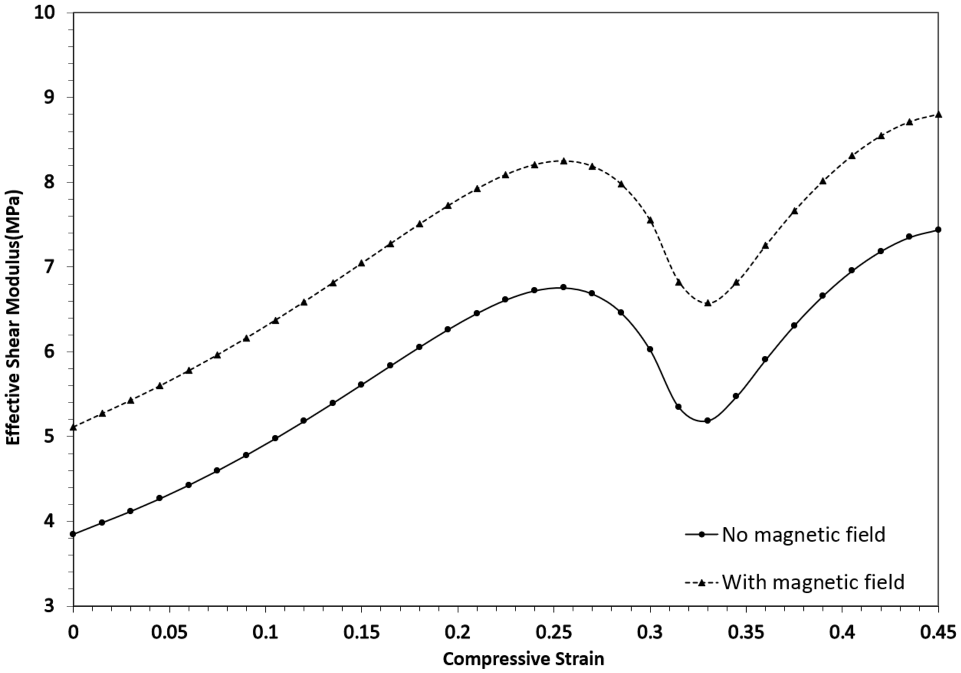

Figure 8.10 Effective shear modulus vs. compressive strain with and without the magnetic field.

To further investigate the mechanisms underlying the effects observed previously, we analyzed models with wavy chains of different p values. The absolute MR effects calculated from these models are depicted in the accompanying Figure 8.11.

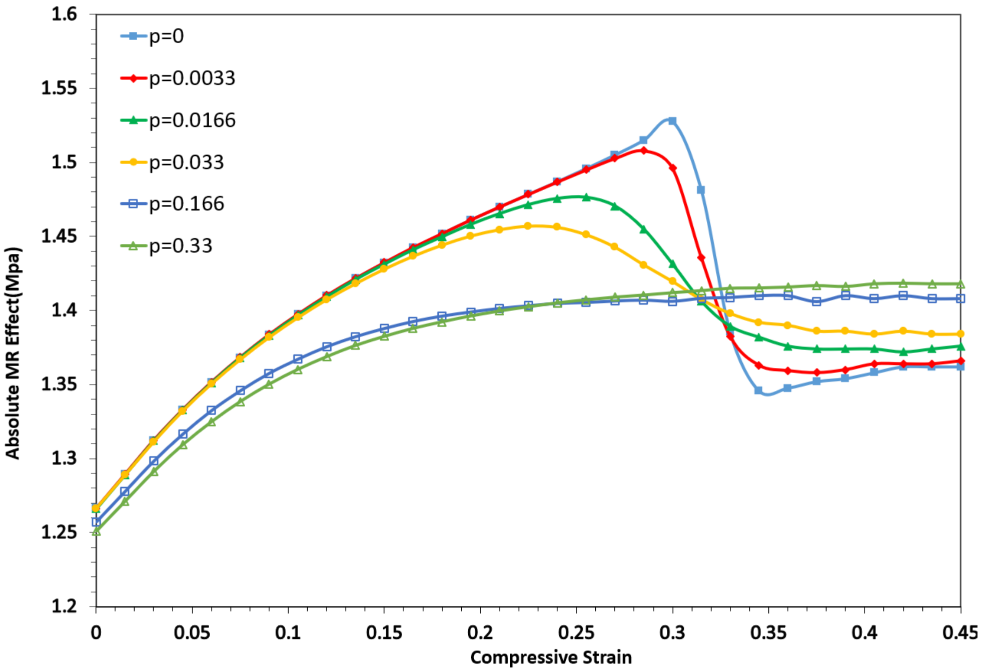

Figure 8.11 Effective shear modulus vs. compressive strain with and without the magnetic field for MRE with wavy chains.

.

Results show that chains with smaller p values, which are straighter, exhibit a higher initial MR effect due to tighter alignment and interaction between particles. As p increases, indicating more wave-like configurations, the MR effect initially rises rapidly at low compressive strains but begins to plateau at higher strains. For models with smaller p values that are prone to buckling, there is a sharp and sudden drop in the MR effect. This drop aligns with the peak stiffness observed in models without magnetic fields and continues until a critical strain is reached, after which the MR effect stabilizes. This pattern indicates a critical transition point in the structural integrity of the material, consistent across different p values.

To elucidate the phenomena observed, we propose that the onset of buckling is due to the stress concentration within the matrix between the particles of a chain. As the strain within this chain reaches a specific threshold, further increases in strain will trigger the shear buckling, resulting in a reduction in the modulus. This understanding of the mechanics is supported by our analysis of the magnetic interactions between particles, which can be divided into two primary components: the vertical and horizontal forces. Our research indicates that only the horizontal force significantly contributes to the MR effect when no compressive strain is applied. During shear deformation, this horizontal attraction opposes the direction of the shear, enhancing the MR effect. At smaller strains, compressive forces narrow the distances between particles, intensifying the both of the magnetic forces; however, at this stage, the vertical forces are less influential, and the increased horizontal force dominates the MR effect.

As compressive strain increases beyond a certain point, the continued compression leads to a reduction in shear stiffness. During this phase, the vertical magnetic force exacerbates the compression, further reducing shear stiffness, while the horizontal force continues to exert a positive MR effect. These two forces interact within the material, and as additional strain is applied, the sensitivity to vertical strain increases, leading to a predominant negative MR effect from the vertical forces, resulting in a decline in the absolute MR effect. However, upon reaching the buckling threshold, particle rearrangement alleviates the stress concentration, and further strain or vertical magnetic force no longer reduces shear stiffness, resulting in stabilized material behavior.

This mechanism also helps explain the influence of varying magnetic field strengths on the critical strain for instability. At lower magnetic fields, the stabilizing effect of the horizontal magnetic force predominates, increasing the critical strain and stabilizing the material. Conversely, at higher magnetic fields, the vertical force becomes dominant, compressing the matrix within the chain and enhancing stress concentration similarly to mechanical compression. This more substantial effect at higher fields leads to a decrease in the critical strain, illustrating the dual role of magnetic forces in influencing material stability and the MR effect.

8.4 Modeling of Interface Stability

In the section on interface stability, we delve into how interface friction influences instability issues within MREs. We utilize a fully debonded interface model with friction to understand its impact compared to fully bonded models. Figure 8.12 illustrates the model configuration at various stages: pre-buckling (a), at the onset of buckling (b), and post-buckling (c), corresponding to compressive strains of 0.25, 0.30, and 0.35, respectively. Additionally, the displacement ratio q of particle three relative to compressive strain is also depicted in Figure 8.13 using the third particle from the top with the largest vertical displacement.

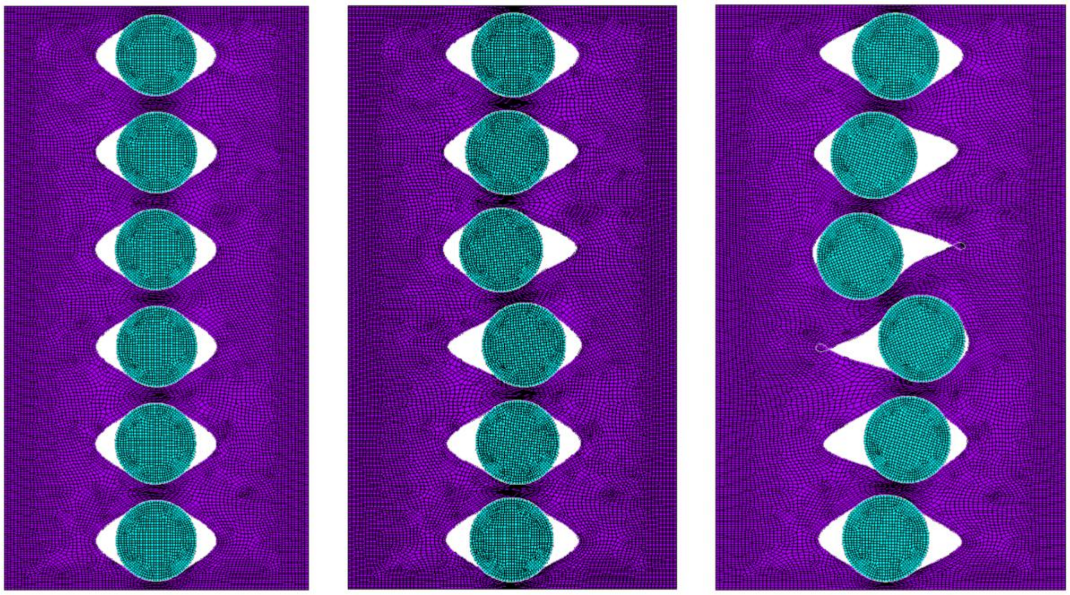

(a) (b) (c)

Figure 8.12 FEM model illustration of interface conditions at strain: (a) 0.25, (b) 0.3, (c) 0.35.

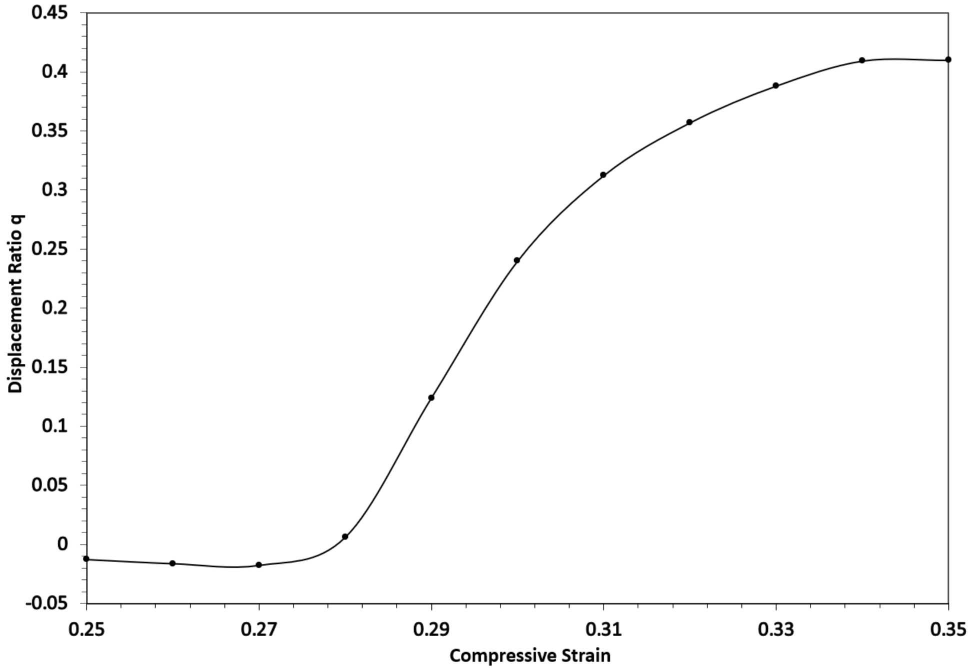

Figure 8.13 Critical strain detection with the weakly bonded model of straight chain.

Our observations indicate that models accounting for interface effects exhibit earlier debonding compared to fully bonded models. With the same radius factor of 0.333, the critical strain for buckling in the fully bonded model occurs around 0.335, while the debonded model shows a reduced critical strain of approximately 0.28. This earlier onset of instability in the debonded model is due to less constraint within the particle chains, leading to decreased structural stability. A noteworthy behavior observed post-buckling is the pattern of horizontal displacement, which initially increases linearly, then slows, and finally stabilizes near a strain of 0.34. This pattern differs from that in bonded cases and can be elucidated by the interface conditions visualized in Figure 8.12(b). As buckling commences, particles begin to rearrange; however, unlike in bonded scenarios, they first compress towards the sides of their containment, facilitated by the interface friction, which promotes a rapid, linear increase in displacement. Subsequently, as particles reach the boundary limits of their movement, the geometrical constraints halt further lateral displacement, slowing the displacement rate. This dynamic is particularly intriguing as it signifies a phase of high relative friction during debonding, indicative of significant energy dissipation. This behavior is not exclusive to MREs with straight chain configurations; it also manifests in MREs with wavy chains. Figure 8.14 illustrates the FEM models of an MRE subjected to varying compressive strains, ranging from 0.15 to 0.3. The corresponding critical strain curve is shown in Figure 8.15.

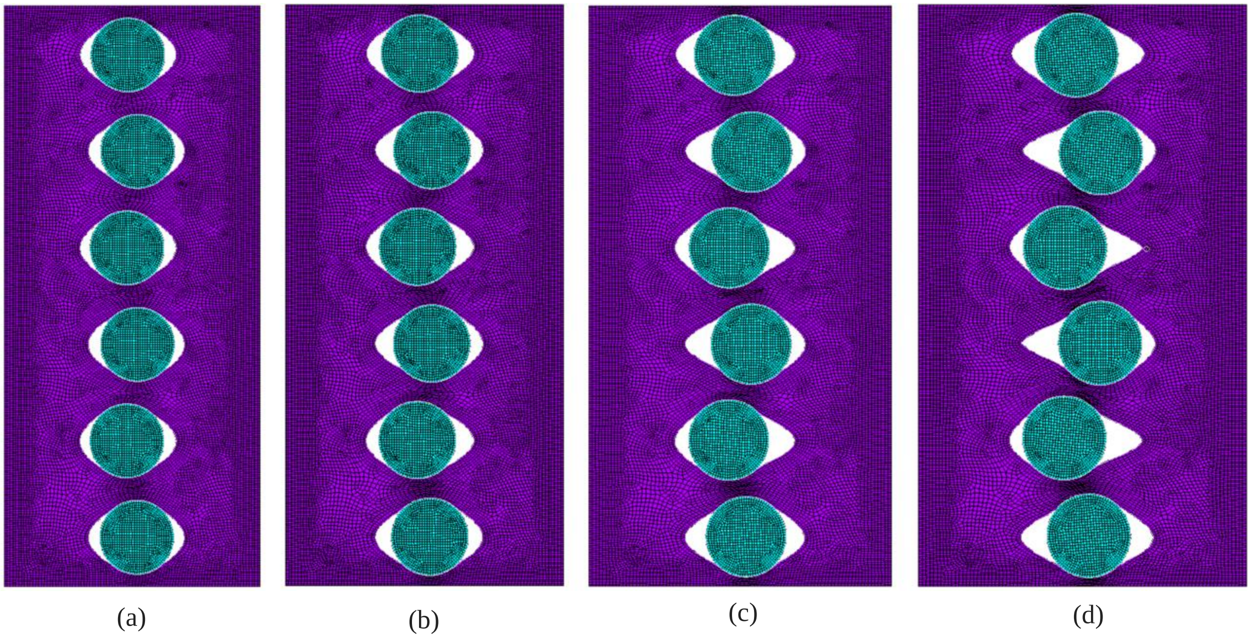
(a) (b) (c) (d)

Figure 8.14 FEM model illustration of interface conditions of wavy chains at strain: (a) 0.15, (b) 0.2, (c) 0.25, (d) 0.3.

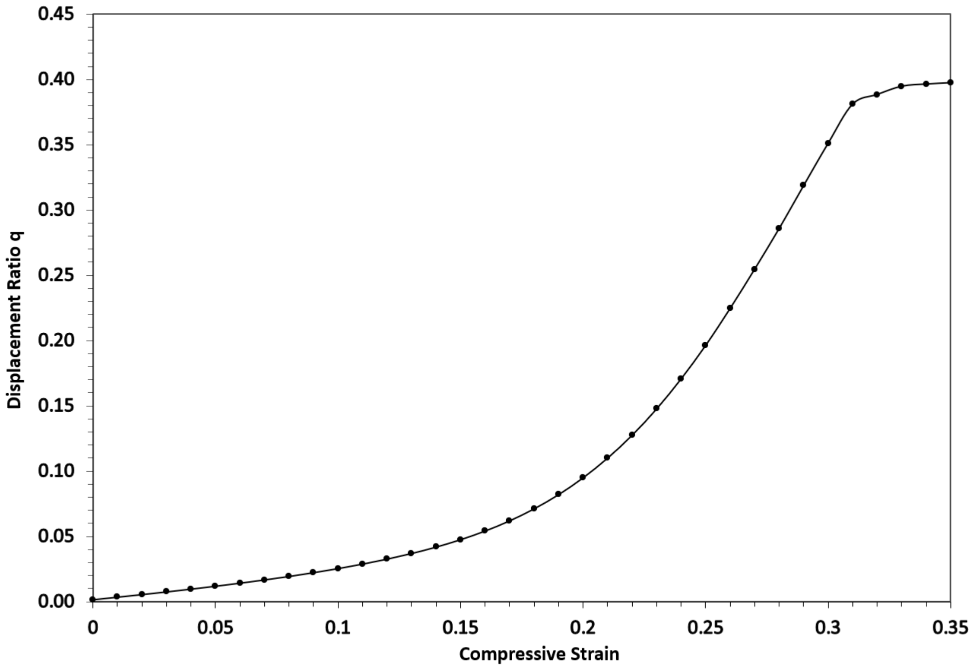

Figure 8.15 Critical strain detection with the weakly bonded model of wavy chain.

Compared with the straight chain model, particles in the wavy chain model do not experience the abrupt vertical displacement typically seen in buckling. Instead, displacement increases steadily with compressive strain. However, as observed in the interface figures, wavy chains exhibit similar interface friction behavior to straight chains, where particles are squeezed towards the edges as strain increases. This squeezing occurs suddenly and briefly in straight chains while it unfolds gradually and smoothly in wavy chains. Notably, although their behaviors differ at smaller strains, once the particles are squeezed to the edges, their distributions become similar, making further movement challenging, which makes them have similar microstructural distribution at higher compression. Additionally, various particle distribution patterns emerge under these conditions. While not the primary focus of this study, these patterns suggest underlying mechanisms that warrant further investigation.

8.5 Conclusions

In Chapter 8, we conducted a thorough analysis of the instabilities in magnetorheological MREs under compression. We explored macroscopic, microscopic, and interface instabilities, each influenced by complex interactions within the MRE structure. Our study integrated detailed modeling strategies, such as the use of a sextic polynomial for macroscopic instability, which highlighted how the magnetic field can alternatively stabilize or destabilize the MRE depending on its intensity. Microscopically, we observed how slight imperfections in particle positioning could precipitate instability, emphasizing the sensitivity of MREs to their microstructural configuration. The introduction of interface friction models further enriched our understanding, illustrating how debonding processes could influence mechanical behavior significantly. These models helped identify the critical strains at which instabilities occur, showcasing the intricate balance between magnetic and mechanical forces within MREs. The findings from this chapter lay a solid foundation for refining MRE models, enhancing their predictive capabilities, and tailoring them for specific applications where instability might affect performance.

Chapter 9 Conclusions and Future Works

9.1 Conclusions

This dissertation is committed to bridging the gap between microscopic-based modeling and phenomenological approaches, ensuring a precise alignment with experimental findings through detailed finite element simulations. The primary objective is to develop a robust, physics-based model that accurately simulates and elucidates the complex nonlinear stiffness and damping behaviors of materials under dynamic loading conditions. The key contributions of this dissertation are summarized as follows:

Our simulations reveal that the FEM model, when assuming all particles are bonded, fails to capture the dynamic damping behavior of MREs. It is essential to consider the effects of interface friction. By analyzing the affine local deformation using an RVE with a complete chain, we observed distinct interface behaviors of particles at various positions along the chain under the influence of a magnetic field, each contributing differently to the damping effects of MREs. Further investigation into these behaviors and measuring the response under each type of interface condition has allowed us to construct a FEM model that can simulate and clarify distinct experimental findings. We have successfully explained the varied damping behaviors of MREs with isotropic and orthotropic distributions, as well as with strong and weak interface bondings. This research paves the way for advancements in the simulation of interface friction and offers significant potential for future enhancements in the phenological models.

Building on prior research, we have expanded the instability analysis to consider the effects of shear stiffness, varying initial particle distributions, and the magnetorheological (MR) effect. Our simulations indicate that as compressive strains increase before the onset of instability caused by compression, the shear stiffness of MREs decreases at an earlier stage due to premature buckling under the combined effects of compression and unit shear. This reveals that MREs subjected to simultaneous compression and shear forces might buckle earlier than anticipated. Furthermore, we have detailed the influence of the magnetic field on instability by dividing it into horizontal and vertical components, each contributing uniquely to buckling phenomena. This concept also comprehensively explains the impact of the magnetic field on critical strain. Additionally, by integrating the instability simulations with the interface model, we discovered that instability develops earlier, accompanied by a unique friction behavior under compression, which could potentially explain the significant increase in damping observed in MREs during compression.

9.2 Future Works

The suggestions for future research are listed below:

Enhancing the stability and predictive capabilities of the instability models through the incorporation of advanced friction models, such as the LuGre friction model, appears promising. This improvement could significantly enhance the convergence of simulations involving cyclic compressive loading, where pronounced interfacial friction behaviors are observed. As a final remark, the two major achievements in this dissertation are summarized below:

Developing a more refined friction energy model could significantly enhance our ability to capture and quantify energy losses during loading. This model would enable precise calculations of energy dissipation, differentiating between losses attributed to friction and other factors. Such a model would provide a detailed quantitative analysis, offering insights into the relative contributions of various mechanisms to the overall energy loss in the system.

The inclusion of nonlinear ferromagnetic behavior, demagnetization, and magnetic saturation effects would expand the model's applicability and accuracy over a broader range of magnetic field strengths, thereby enhancing its practical relevance for engineering applications. Furthermore, the adaptation of our models to encompass larger magnetic fields and more complex loading scenarios could bridge the gap between theoretical predictions and experimental observations. There's also the potential to develop a detailed categorization of how physical parameter variations affect the model's behavior and how these modifications align or diverge from phenomenological predictions. Such an analysis could lead to a more nuanced understanding of the underlying mechanisms and foster the development of physically interpretable and practically applicable models.

A gap remains in experimentally verifying the proposed different interface debonding types under magnetic influences. Utilizing advanced imaging techniques, such as NanoCT, could provide invaluable insights into the microstructural changes at the interface before and after magnetic field application, thereby validating the simulation models.

Expanding the model to include macroscopic applications is another avenue for research. By maintaining the microscale model's predictive accuracy and simplifying it into homogenized material properties, it could be effectively integrated into larger structural analyses. This process could involve developing physically-based phenomenological models or applying machine learning techniques to distill complex micro-interactions into usable forms for engineering applications. These advancements would push the boundaries of how MR materials are modeled and applied, aligning simulation closer to real-world phenomena.

References

[1] Carlson, J. David, and Mark R. Jolly. "MR fluid, foam and elastomer devices." mecha tronics 10.4-5 (2000): 555-569.

[2] Rabinow, J. "The Magnetic Fluid Clutch AIEE Transactions, 67." (1948): 1308-1315.

[3] Bell, R. C., D. Zimmerman, and A. Vavreck. "Properties of Magnetorheological Fluid s." Retrieved January 29 (2006): 2011.

[4] Rigbi, Zvi, and Leif Jilken. "The response of an elastomer filled with soft ferrite to mechanical and magnetic influences." Journal of magnetism and magnetic materials 37.3 (1983): 267-276.

[5] Jolly, Mark R., et al. "The magnetoviscoelastic response of elastomer composites co nsisting of ferrous particles embedded in a polymer matrix." Journal of Intelligent Mat erial Systems and Structures 7.6 (1996): 613-622.

[6] Ahamed, Raju, Seung-Bok Choi, and Md Meftahul Ferdaus. "A state of art on magnetorheological materials and their potential applications." Journal of Intelligent Material Systems and Structures 29.10 (2018): 2051-2095.

[7] Hooshiar, Amir, Ali Alkhalaf, and Javad Dargahi. "Development and assessment of a stiffness display system for minimally invasive surgery based on smart magnetorheological elastomers." Materials Science and Engineering: C 108 (2020): 110409.

[8] Xu, Tianqi, et al. "Millimeter-scale flexible robots with programmable three-dimensional magnetization and motions." Science Robotics 4.29 (2019): eaav4494.

[9] Jung, Hyung-Jo, et al. "Dynamic characterization of magnetorheological elastomers in shear mode." IEEE transactions on magnetics 45.10 (2009): 3930-3933.

[10] Ginder, John M., et al. "Magnetorheological elastomers: properties and applications." Smart Structures and Materials 1999: Smart Materials Technologies. Vol. 3675. SPIE, 1999.

[11] Jolly, Mark R., J. David Carlson, and Beth C. Munoz. "A model of the behaviour of magnetorheological materials." Smart materials and structures 5.5 (1996): 607.

[12] Lokander, Mattias, and Bengt Stenberg. "Performance of isotropic magnetorheological rubber materials." Polymer Testing 22.3 (2003): 245-251.

[13] Shiga, Tohru, Akane Okada, and Toshio Kurauchi. "Magnetroviscoelastic behavior of composite gels." Journal of Applied Polymer Science 58.4 (1995): 787-792.

[14] Bellan, C., and G. Bossis. "Field dependence of viscoelastic properties of MR elastomers." International journal of modern physics B 16.17n18 (2002): 2447-2453.

[15] Kallio, Marke. The elastic and damping properties of magnetorheological elastomers. Espoo, Finland: VTT, 2005.

[16] Li, Yancheng, et al. "A state-of-the-art review on magnetorheological elastomer devices." Smart materials and structures 23.12 (2014): 123001.

[17] Vatandoost, Hossein, et al. "A novel phenomenological model for dynamic behavior of magnetorheological elastomers in tension–compression mode." Smart Materials and Structures 26.6 (2017): 065011.

[18] Du, Haiping, Weihua Li, and Nong Zhang. "Semi-active variable stiffness vibration control of vehicle seat suspension using an MR elastomer isolator." Smart materials and structures 20.10 (2011): 105003.

[19] Shi, Guanxin, et al. "Study of crosslink structure and dynamic mechanical properties of magnetorheological elastomer: Effect of vulcanization system." Journal of Intelligent Material Systems and Structures 30.8 (2019): 1189-1199.

[20] Lu, Huanglei, et al. "Effect of carbon black with large particle size on dynamic mechanical analysis of magnetorheological elastomers (MREs)." Materials Research Express 5.9 (2018): 095703.

[21] Jin, Qian, et al. "Influence of the particle size on the rheology of magnetorheological elastomer." Materials Science Forum. Vol. 809. Trans Tech Publications Ltd, 2015.

[22] Hegde, Sriharsha, Umanath R. Poojary, and K. V. Gangadharan. "Experimental investigation of effect of ingredient particle size on dynamic damping of RTV Silicone base Magnetorheological elastomers." Procedia Materials Science 5 (2014): 2301-2309.

[23] Guan, Xinchun, Xufeng Dong, and Jinping Ou. "Magnetostrictive effect of magnetorheological elastomer." Journal of Magnetism and magnetic materials 320.3-4 (2008): 158-163.

[24] Krueger, Hannes, Mohammad Vaezi, and Shoufeng Yang. "3d printing of magnetorheological elastomers (mres) smart materials." (2014).

[25] Bastola, A. K., V. T. Hoang, and L. Li. "A novel hybrid magnetorheological elastomer developed by 3D printing." Materials & Design 114 (2017): 391-397.

[26] Norouzi, Mahmood, et al. "A new approach for modeling of magnetorheological elastomers." Journal of Intelligent Material Systems and Structures 27.8 (2016): 1121-1135.

[27] Lu, Xiushou, et al. "Mechanical and structural investigation of isotropic and anisotropic thermoplastic magnetorheological elastomer composites based on poly (styrene-b-ethylene-co-butylene-b-styrene)(SEBS)." Rheologica acta 51.1 (2012): 37-50.

[28] Varga, Zsolt, Genovéva Filipcsei, and Miklós Zrínyi. "Magnetic field sensitive functional elastomers with tuneable elastic modulus." Polymer 47.1 (2006): 227-233.

[29] Johnson, Norman, Faramarz Gordaninejad, and Xiaojie Wang. "Dynamic behavior of thick magnetorheological elastomers." Journal of Intelligent Material Systems and Structures 29.2 (2018): 183-193.

[30] Harne, Ryan L., Zhangxian Deng, and Marcelo J. Dapino. "Adaptive magnetoelastic metamaterials: A new class of magnetorheological elastomers." Journal of Intelligent Material Systems and Structures 29.2 (2018): 265-278.

[31] Abramchuk, S. S., et al. "Effect of a homogeneous magnetic field on the mechanical behavior of soft magnetic elastomers under compression." Polymer Science Series A 48 (2006): 138-145.

[32] Gao, Wei, and Xingzhe Wang. "Steady shear characteristic and behavior of magneto-thermo-elasticity of isotropic MR elastomers." Smart Materials and Structures 25.2 (2016): 025026.

[33] Małecki, P., et al. "Influence of carbonyl iron particle coating with silica on the properties of magnetorheological elastomers." Smart Materials and Structures 25.10 (2016): 105030.

[34] Kallio, Marke. The elastic and damping properties of magnetorheological elastomers. Espoo, Finland: VTT, 2005.

[35] Du, Haiping, Weihua Li, and Nong Zhang. "Semi-active variable stiffness vibration control of vehicle seat suspension using an MR elastomer isolator." Smart materials and structures 20.10 (2011): 105003.

[36] Li, Weihua, Xianzhou Zhang, and Haiping Du. "Development and simulation evaluation of a magnetorheological elastomer isolator for seat vibration control." Journal of Intelligent Material Systems and Structures 23.9 (2012): 1041-1048.

[37] Stepanov, G. V., et al. "Effect of a homogeneous magnetic field on the viscoelastic behavior of magnetic elastomers." Polymer 48.2 (2007): 488-495.

[38] Li, W. H., and X. Z. Zhang. "A study of the magnetorheological effect of bimodal particle based magnetorheological elastomers." Smart Materials and Structures 19.3 (2010): 035002.

[39] Varga, Zsolt, Genovéva Filipcsei, and Miklós Zrínyi. "Magnetic field sensitive functional elastomers with tuneable elastic modulus." Polymer 47.1 (2006): 227-233.

[40] Khanouki, Mostafa Asadi, Ramin Sedaghati, and Masoud Hemmatian. "Experimental characterization and microscale modeling of isotropic and anisotropic magnetorheological elastomers." Composites Part B: Engineering 176 (2019): 107311.

[41] Tong, Yu, Xufeng Dong, and Min Qi. "Payne effect and damping properties of flower-like cobalt particles-based magnetorheological elastomers." Composites Communications 15 (2019): 120-128.

[42] Hapipi, Norhiwani, et al. "The field-dependent rheological properties of plate-like carbonyl iron particle-based magnetorheological elastomers." Results in Physics 12 (2019): 2146-2154.

[43] Koo, Jeong-Hoi, Alexander Dawson, and Hyung-Jo Jung. "Characterization of actuation properties of magnetorheological elastomers with embedded hard magnetic particles." Journal of Intelligent Material Systems and Structures 23.9 (2012): 1049-1054.

[44] Puente-Córdova, Jesús G., et al. "Fabrication and characterization of isotropic and anisotropic magnetorheological elastomers, based on silicone rubber and carbonyl iron microparticles." Polymers 10.12 (2018): 1343.

[45] Ahmad Khairi, Muntaz Hana, et al. "Enhancement of particle alignment using silicone oil plasticizer and its effects on the field-dependent properties of magnetorheological elastomers." International journal of molecular sciences 20.17 (2019): 4085.

[46] Shabdin, Muhammad Kashfi, et al. "Material characterizations of gr-based magnetorheological elastomer for possible sensor applications: Rheological and resistivity properties." Materials 12.3 (2019): 391.

[47] Yunus, Nurul Azhani, et al. "Thermal stability and rheological properties of epoxidized natural rubber-based magnetorheological elastomer." International Journal of Molecular Sciences 20.3 (2019): 746.

[48] Burgaz, Engin, and Mert Goksuzoglu. "Effects of magnetic particles and carbon black on structure and properties of magnetorheological elastomers." Polymer Testing 81 (2020): 106233.

[49] Soria-Hernández, Cintya G., et al. "Investigation of the effect of carbonyl iron micro-particles on the mechanical and rheological properties of isotropic and anisotropic MREs: Constitutive magneto-mechanical material model." Polymers 11.10 (2019): 1705.

[50] Rodríguez-Bermejo, Jose, et al. "Thermal study of a transport container." Journal of Food Engineering 80.2 (2007): 517-527.

[51] Li, W. H., Yang Zhou, and T. F. Tian. "Viscoelastic properties of MR elastomers under harmonic loading." Rheologica acta 49 (2010): 733-740.

[52] Agirre-Olabide, Iker, et al. "Characterization of the linear viscoelastic region of magnetorheological elastomers." Journal of Intelligent Material Systems and Structures 25.16 (2014): 2074-2081.

[53] Chen, Lin, and Steve Jerrams. "A rheological model of the dynamic behavior of magnetorheological elastomers." Journal of Applied Physics 110.1 (2011).

[54] Bouc, R. "Forced vibrations of mechanical systems with hysteresis." Proc. of the Fourth Conference on Nonlinear Oscillations, Prague, 1967. 1967.

[55] Wen, Yi-Kwei. "Method for random vibration of hysteretic systems." Journal of the engineering mechanics division 102.2 (1976): 249-263.

[56] Yang, Jian, et al. "Experimental study and modeling of a novel magnetorheological elastomer isolator." Smart Materials and Structures 22.11 (2013): 117001.

[57] Truesdell, C. "General and exact theory of waves in finite elastic strain." Arch. Rational Mech. Anal 8.263 (1961): 1976.

[58] Tiersten, HF1812240131. "Coupled magnetomechanical equations for magnetically saturated insulators." Journal of Mathematical Physics 5.9 (1964): 1298-1318.

[59] Maugin, Gérard A., and A. Cemal Eringen. "Deformable magnetically saturated media. I.

Field equations." Journal of Mathematical Physics 13.2 (1972): 143-155.

[60] Kankanala, S. V., and N20998281115 Triantafyllidis. "On finitely strained magnetorheological elastomers." Journal of the Mechanics and Physics of Solids 52.12 (2004): 2869-2908.

[61] Dorfmann, A., and R. W. Ogden. "Nonlinear electroelastic deformations." Journal of Elasticity 82 (2006): 99-127.

[62] Bustamante, R., and KR3326341 Rajagopal. "Implicit constitutive relations for nonlinear magnetoelastic bodies." Proceedings of the Royal Society A: Mathematical, Physical and Engineering Sciences 471.2175 (2015): 20140959.

[63] Spieler, Christian, Markus Kästner, and Volker Ulbricht. "Analytic and numeric solution of a magneto-mechanical inclusion problem." Archive of Applied Mechanics 85 (2015): 1483-1497.

[64] Bustamante, R25114781168. "Mathematical modelling of boundary conditions for magneto-sensitive elastomers: variational formulations." Journal of Engineering Mathematics 64 (2009): 285-301.

[65] Bustamante, Roger, Alois Dorfmann, and Ray W. Ogden. "Numerical solution of finite geometry boundary-value problems in nonlinear magnetoelasticity." International Journal of Solids and Structures 48.6 (2011): 874-883.

[66] Davis, LCs. "Model of magnetorheological elastomers." Journal of applied physics 85.6 (1999): 3348-3351.

[67] Danas, Kankanala, S. V. Kankanala, and Nicolas Triantafyllidis. "Experiments and modeling of iron-particle-filled magnetorheological elastomers." Journal of the Mechanics and Physics of Solids 60.1 (2012): 120-138.

[68] Coquelle, E., et al. "Micromechanical analysis of an elastomer filled with particles organized in chain-like structure." Journal of materials science 41 (2006): 5941-5953.

[69] Borbáth, T., et al. "XμCT analysis of magnetic field-induced phase transitions in magnetorheological elastomers." Smart materials and structures 21.10 (2012): 105018.

[70] Chen, Lin, X. L. Gong, and W. H. Li. "Microstructures and viscoelastic properties of anisotropic magnetorheological elastomers." Smart materials and structures 16.6 (2007): 2645.

[71] COQUELLE, Eric, and Georges BOSSIS. "Magnetostriction and piezoresistivity in elastomers filled with magnetic particles." Journal of Advanced Science 17.1+ 2 (2005): 132-138.

[72] Ivaneyko, Dmytro, et al. "Magneto-sensitive elastomers in a homogeneous magnetic field: a regular rectangular lattice model." Macromolecular Theory and Simulations 20.6 (2011): 411-

424.

[73] Han, Yi, Wei Hong, and LeAnn E. Faidley. "Field-stiffening effect of magnetorheological elastomers." International Journal of Solids and Structures 50.14-15 (2013): 2281-2288.

[74] Ivaneyko, D., et al. "Effects of particle distribution on mechanical properties of magneto-sensitive elastomers in a homogeneous magnetic field." arXiv preprint arXiv:1210.1401 (2012).

[75] Ivaneyko, D., et al. "Mechanical Properties of Magneto-Sensitive Elastomers in a Homogeneous Magnetic Field: Theory and Experiment." Macromolecular Symposia. Vol. 338. No. 1. 2014.

[76] Khanouki, Mostafa Asadi, and Ramin Sedaghati. "Modeling of Magneto-Mechanical Response of Magnetorhological Elastomers having Different Arrangement of Magnetic Particles."

[77] Khanouki, Mostafa Asadi, Ramin Sedaghati, and Masoud Hemmatian. "Experimental characterization and microscale modeling of isotropic and anisotropic magnetorheological elastomers." Composites Part B: Engineering 176 (2019): 107311.

[78] Galipeau, Evan, et al. "Magnetoactive elastomers with periodic and random microstructures." International journal of solids and structures 51.18 (2014): 3012-3024.

[79] Coquelle, E., and G. Bossis. "Mullins effect in elastomers filled with particles aligned by a magnetic field." International Journal of Solids and Structures 43.25-26 (2006): 7659-7672.

[80] Allahyarov, Elshad, Hartmut Löwen, and Lei Zhu. "A simulation study of the electrostriction effects in dielectric elastomer composites containing polarizable inclusions with different spatial distributions." Physical Chemistry Chemical Physics 17.48 (2015): 32479-32497.

[81] Chen, S. W., et al. "Micromechanical analysis on tensile modulus of structured magnetorheological elastomer." Smart Materials and Structures 25.3 (2016): 035001.

[82] Metsch, Philipp, et al. "A numerical study on magnetostrictive phenomena in magnetorheological elastomers." Computational Materials Science 124 (2016): 364-374.

[83] Khanouki, Mostafa Asadi, Ramin Sedaghati, and Masoud Hemmatian. "Adaptive dynamic moduli of magnetorheological elastomers: From experimental identification to microstructure-based modeling." Materials Science and Engineering: B 267 (2021): 115083.

[84] Kalina, Karl A., et al. "Multiscale modeling and simulation of magneto-active elastomers based on experimental data." Physical Sciences Reviews 8.1 (2023): 1-31.

[85] Chougale, Sanket, Dirk Romeis, and Marina Saphiannikova. "Transverse isotropy in magnetoactive elastomers." Journal of Magnetism and Magnetic Materials 523 (2021): 167597.

[86] Zabihyan, R., et al. "FE2 simulations of magnetorheological elastomers: influence of microscopic boundary conditions, microstructures and free space on the macroscopic responses of MREs." International Journal of Solids and Structures 193 (2020): 338-356.

[87] Mukherjee, Dipayan, Laurence Bodelot, and Kostas Danas. "Microstructurally-guided explicit continuum models for isotropic magnetorheological elastomers with iron particles." International Journal of Non-Linear Mechanics 120 (2020): 103380.

[88] Garcia-Gonzalez, Daniel, and Mokarram Hossain. "Microstructural modelling of hard-magnetic soft materials: Dipole–dipole interactions versus Zeeman effect." Extreme Mechanics Letters 48 (2021): 101382.

[89] Nguyen, Xuan Bao, Toshihiko Komatsuzaki, and Nong Zhang. "A nonlinear magnetorheological elastomer model based on fractional viscoelasticity, magnetic dipole interactions, and adaptive smooth Coulomb friction." Mechanical Systems and Signal Processing 141 (2020): 106438.

[90] Landau, L. D. & Lifshitz, E. M. (1984). Course of Theoretical Physics (2nd ed.). (Vol. 8). New York, NY: Pergamon.

[91] Mizzi, Luke, et al. "Implementation of periodic boundary conditions for loading of mechanical metamaterials and other complex geometric microstructures using finite element

analysis." Engineering with Computers 37 (2021): 1765-1779.

[92] Metsch, P., et al. "Two-and three-dimensional modeling approaches in magneto-mechanics: a quantitative comparison." Archive of Applied Mechanics 89 (2019): 47-62.

[93] Biller, A. M., O. V. Stolbov, and Yu L. Raikher. "Dipolar models of ferromagnet particles interaction in magnetorheological composites." J. Optoelectron. Adv. Mater 17.7 (2015): 1106-1113.

[94] Biller, A. M., O. V. Stolbov, and Yu L. Raikher. "Modeling of particle interactions in magnetorheological elastomers." Journal of Applied Physics 116.11 (2014).

[95] Barbero, Ever J. Finite element analysis of composite materials using Abaqus®. CRC press, 2023.

[96] Hashin, Zvi, and Shmuel Shtrikman. "A variational approach to the theory of the elastic behaviour of multiphase materials." Journal of the Mechanics and Physics of Solids 11.2 (1963): 127-140.

[97] Weng, G. J. "Some elastic properties of reinforced solids, with special reference to isotropic ones containing spherical inclusions." International Journal of Engineering Science 22.7 (1984): 845-856.

[98] Hill, Rodney. "A self-consistent mechanics of composite materials." Journal of the Mechanics and Physics of Solids 13.4 (1965): 213-222.

[99] Budiansky, Bernard. "On the elastic moduli of some heterogeneous materials." Journal of the Mechanics and Physics of Solids 13.4 (1965): 223-227.

[100] Norouzi, Mahmood, et al. "A new approach for modeling of magnetorheological elastomers." Journal of Intelligent Material Systems and Structures 27.8 (2016): 1121-1135.

[101] Dargahi, Ashkan, Ramin Sedaghati, and Subhash Rakheja. "On the properties of magnetorheological elastomers in shear mode: Design, fabrication and characterization." Composites Part B: Engineering 159 (2019): 269-283.

[102] G. Heinrich, M. Kluppel, Recent advances in the theory of filler networking in elastomers, Fill. Elastom. Drug Deliv. Syst. 160 (2002) 1e44.

[103] D. Ponnamma, S.H. Sung, J.S. Hong, K.H. Ahn, K.T. Varughese, S. Thomas, Influence of non-covalent functionalization of carbon nanotubes on the rheological behavior of natural rubber latex nanocomposites, Eur. Polym. J. 53 (2014) 147e159.

[104] P.G. Maier, D. Goritz, Molecular interpretation of the Payne effect, Kaut Gummi Kunstst. 49 (1) (1996) 18e21.

[105] Fan, Yanceng, et al. "Interfacial friction damping properties in magnetorheological elastomers." Smart materials and structures 20.3 (2011): 035007.

[106] Li, Jian-feng, and Xing-long Gong. "Dynamic damping property of magnetorheological elastomer." Journal of Central South University of Technology 15.Suppl 1 (2008): 261-265.

[107] Yu, Miao, et al. "Understanding the reinforcing behaviors of polyaniline-modified carbonyl iron particles in magnetorheological elastomer based on polyurethane/epoxy resin IPNs matrix." Composites Science and Technology 139 (2017): 36-46.

[108] Rudykh, Stephan, and Katia Bertoldi. "Stability of anisotropic magnetorheological elastomers in finite deformations: A micromechanical approach." Journal of the Mechanics and Physics of Solids 61.4 (2013): 949-967.

[109] Goshkoderia, Artemii, and Stephan Rudykh. "Stability of magnetoactive composites with periodic microstructures undergoing finite strains in the presence of a magnetic field." Composites Part B: Engineering 128 (2017): 19-29.